4 XFEL accelerator

4.1 Overview

4.1.1 Introduction

The heart of the accelerator complex is the L-band (1.3 GHz) electron linear accelerator (linac) with a nominal design energy of 20 GeV, operating at an accelerating gradient of 23.6 MV/m. It utilises the advanced superconducting radio fequency (RF) technology which has been successfully developed by the international Tera-Electronvolt Superconducting Linear Accelerator (TESLA) Collaboration, leading to the superconducting Linear Collider technical proposal in 2001 **[4-1]**, and which is routinely in operation at the TESLA Test Facility (TTF) Linac and FLASH at Deutsches Elektronen Synchrotron Laboratory (DESY). The advantages of the superconducting linac technology are: the acceleration of a large number of electron bunches per RF pulse (up to about 3,000); small beam-induced wake fields and the possibility of applying intra-bunch train feedback to provide a stable and high quality beam (Section 4.5); and a large operational flexibility regarding beam time structure and energy, including (as a possible future option) high duty cycle (up to continuous wave (CW)-mode) operation. The linac technology is described in detail in Section 4.2. In the following section, a brief overview of the general layout of the accelerator complex and its parameters and a consideration of operational flexibility and future options are given.

4.1.2 Overall layout and choice of parameters

The layout of the accelerator is schematically shown for convenience in Figure 4.1.1 and visualised in a 3D computer drawing in Figure 4.1.2. The electron beam is generated in a laser-driven photocathode RF gun and pre-accelerated in a single superconducting accelerator module (see Section 4.3). The injector is housed in an underground enclosure separate from the linac tunnel, so that it can be commissioned at an early stage, well before installation work in the linac tunnel is completed. Furthermore, there is space foreseen for a completely separate and radiation-shielded second injector, which can be constructed, commissioned and maintained independently from the operation of the first injector.

After transfer to the main accelerator tunnel, the beam is further accelerated by one linac unit (four accelerator modules with eight cavities each, driven by one RF station) to an energy of 0.5 GeV before entering the first bunch compression stage. A third harmonic (3.9 GHz) RF system is foreseen to optimise the longitudinal phase-space properties (Section 4.2.4). After acceleration to 2 GeV with three linac units, the beam enters the second (final) compression stage, after which the bunch peak current has increased to 5 kA, a factor of 100 higher than the initial peak current from the RF gun. Considerable attention to detail has been paid to foreseeing extensive standard and special beam diagnostic tools, to assess the beam phase-space properties after the compression process with high accuracy.

Final acceleration to a nominal maximum beam energy of 20 GeV takes place in the main part of the linac, consisting of 25 RF stations and 100 accelerator modules in total. Downstream from the Linac, a conventional beamline is located, for installation of the beam collimation and trajectory feedback systems, as well as providing and for distribution of the beam into the different undulator beamlines (see Section 4.5), including the connection to a future upgrade of the user facility with more beamlines. A combination of slow and fast switching devices allows generation of bunch trains of different time patterns for different experiments without having to generate and accelerate bunch trains with strongly varying transient beam loading. After having passed through the undulators, the “spent” beam is stopped in radiation-shielded solid absorbers (Section 4.7.4). An additional beam dump is installed in the beam distribution shaft XS1, just upstream from the undulator beamlines. It allows the commission or operation of the accelerator while installation or maintenance work is ongoing in the undulator tunnels.

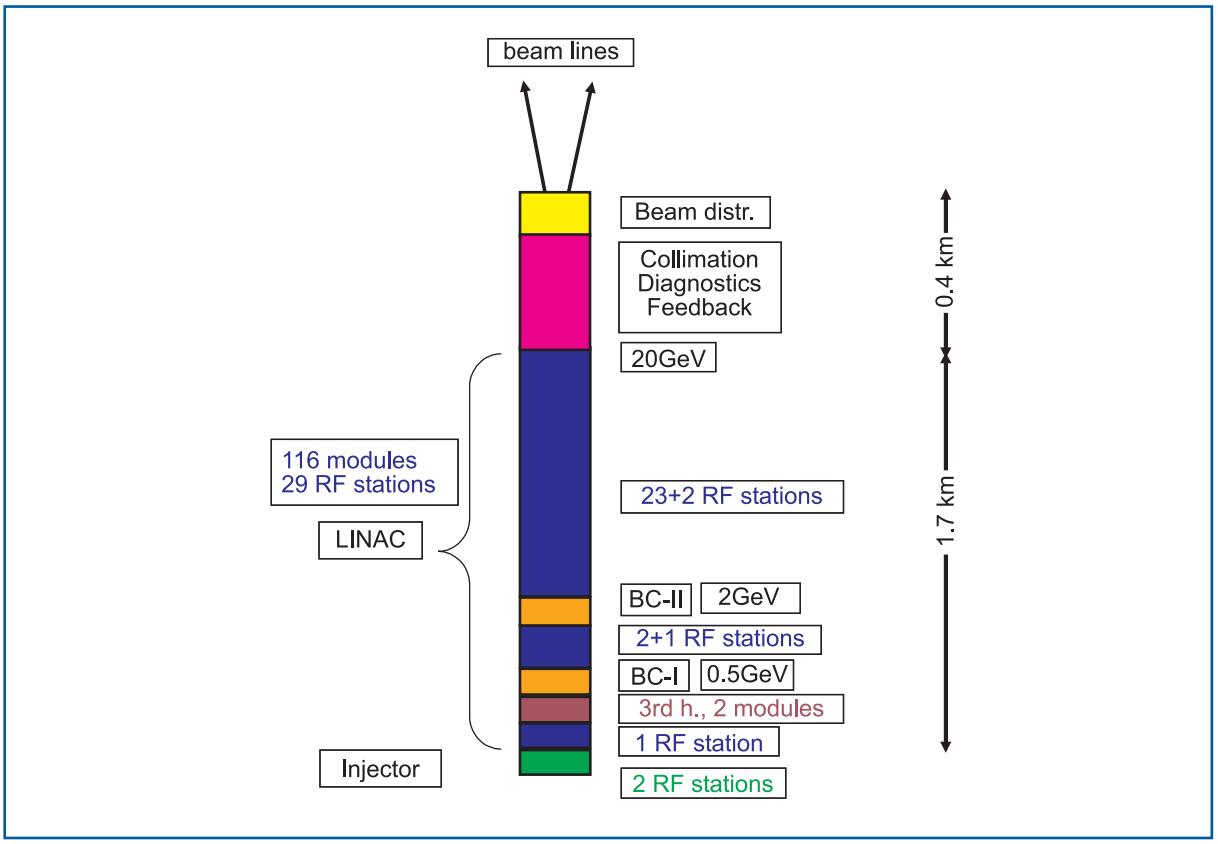

Figure 4.1.1 *Schematic layout of the accelerator.*

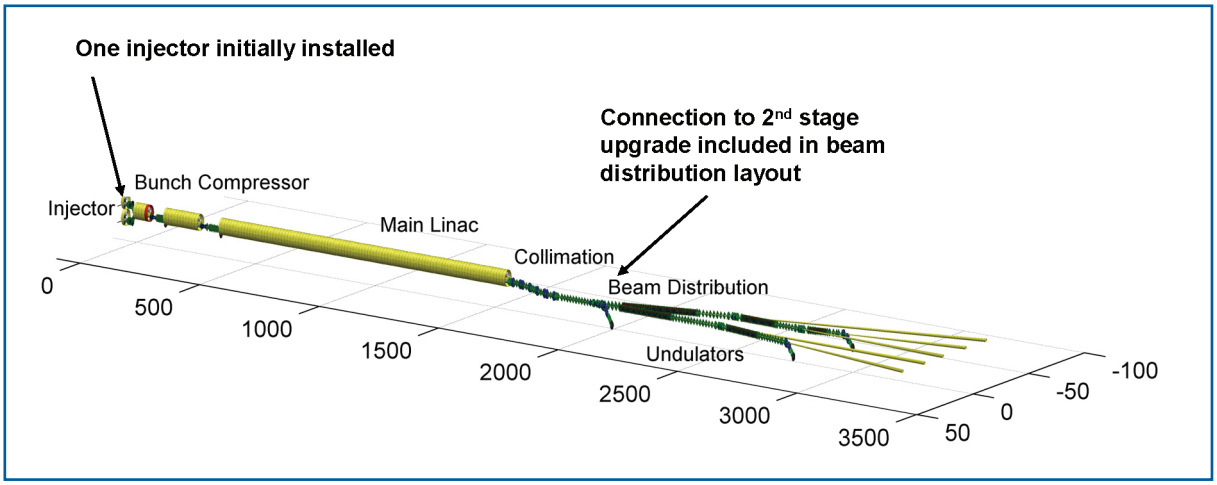

Figure 4.1.2 *3-D sketch of the accelerator complex.*

The layout of the linac includes precautions for energy management in case of RF component failure. The section between the two bunch compression stages consists of three RF units with four accelerator modules each, out of which only two have to be active to accelerate the beam to 2 GeV at the design gradient. Likewise, the main section of the linac (from 2 to 20 GeV) has an overhead of two RF stations. This guarantees that in case of an RF unit failure, there is sufficient energy reserve to maintain both the beam energy at the second bunch compressor stage as well as at the end of the linac. Tunnel access for repair of RF stations during scheduled operation time can, thus, be safely avoided. In practice, the reserve stations will not be left idle when not needed. Instead, all available stations will be operated with reduced gradient and in case a station fails, the gradient will be increased in the other sections to keep the beam energy constant.

The main parameters of the accelerator are summarised in Table 4.1.1. The beam energy required for 0.1 nm photon wavelength in the SASE 1 and SASE 2 beamlines is 17.5 GeV. The linac design energy of 20 GeV thus already includes the potential to reach a lower wavelength of about 0.08 nm. The required peak power per RF station is well below the limit of the 10 MW multibeam klystrons (Section 4.2.4). This lower mode is beneficial for highly reliable operation on one hand and potential upgrade of the beam energy or duty cycle on the other (see Section 4.1.3). Likewise, the cryogenic system is laid out with an overhead of 50% (Section 7.2.5) with similar operational benefits.

Energy for 0.1nm wavelength *(maximum design energy)*	17.5 GeV *(20 GeV)*
Number of installed accelerator modules	116
Number of cavities	928
Acc. gradient (104 active modules) at 20 GeV	23.6 MV/m
Number of installed RF stations	29
Klystron peak power (26 active stations)	5.2 MW
Loaded quality factor Q_{ext}	4.6×10^6
RF pulse length	1.4 ms
Beam pulse length	0.65ms
Repetition rate	10 Hz
Maximum average beam power	600 kW
Unloaded cavity quality factor Q_0	10^{10}
2K cryogenic load (including transfer line losses)	1.7 kW
Maximum number of bunches per pulse *(at 20 GeV)*	3,250 *(3,000)*[1]
Minimum bunch spacing	200 ns
Bunch charge	1 nC
Bunch peak current	5 kA
Emittance (slice) at undulator	1.4 mm*mrad
Energy spread (slice) at undulator	1 MeV

Table 4.1.1 *Main parameters of the accelerator.*

The specified bunch slice emittance takes into account a 50% dilution budget from the injector to the undulators, significantly higher than the calculated dilution from the bunch compression process. The specified slice energy spread takes into account the intentional beam heating to avoid micro-bunching in the compressor (Section 4.4).

4.1.3 Operational flexibility and future options

The single set of basic reference parameters in Table 4.1.1 does not cover the full range of operational flexibility of the linac. There is, within certain limits, a considerable flexibility in operational parameters, based on built-in performance reserves of its technical components.

4.1.3.1 Energy variation

Operation at lower beam energy, thus extending the photon wavelength range to softer x-rays, is an obvious possibility. Variation of the beam energy will always be done by changing the accelerating gradient in the main part of the linac, i.e. after the bunch compressor, leaving the delicate set-up of the lower energy part of the machine completely untouched. Within a range of ±1.5%, a beam energy variation can be applied even within a bunch train (by appropriate programming of the low level RF system). The beamlines after the linac are designed for this dynamic range.

[1] The limitation to 3,000 bunches at 20 GeV beam energy is related to a maximum load of 300 kW on each of the beam dumps in the initially installed two electron beamlines.

Based on the experience gained with the superconducting TESLA cavities (see Section 4.2.1), it can be realistically expected that the linac can be operated at an accelerating gradient somewhat above the specified design value of 23.6 MV/m at 20 GeV. An increase of the gradient to about 28 MV/m would permit a maximum beam energy of 24 GeV, thus significantly extending the photon wavelength range to harder x-rays, provided that an improved injector beam quality simultaneously becomes available to maintain saturation of the Self-Amplified Spontaneous Emission (SASE) Free-Electron Lasers (FEL) process. The RF system power reserve can cope with the required increase in peak power per station. The cryogenic system also has a certain built-in reserve but, at higher energies, the linac repetition rate will have to be somewhat reduced below the nominal value of 10 Hz (see below). All beamline components downstream from the linac are laid out for a maximum energy of 25 GeV, to avoid the conventional accelerator components becoming a limitation for the energy reach.

4.1.3.2 Repetition rate variation

In addition to the possibility of higher beam energies, the available reserve in the RF and cryogenic systems can also be used for increasing the linac repetition rate and thus the duty cycle of the pulsed linac. The limitations on repetition rate depend on the energy at which the linac is operated: at lower energy the RF system is the limitation, at higher energy the cryogenic system. In order to illustrate the likely accessible range of maximum repetition rate against energy, these two limitations are plotted in Figure 4.1.3, under the assumption that the RF systems are operated at 80% of their maximum average power capability and the cryogenic plant at 80% of its design 2 K cooling capacity (the assumption of going to 100% of the design values is viewed as unrealistic for a highly reliable and stable operation). It should be noted that in this case an improvement of the injector for higher duty cycle is also necessary.

Higher repetition rates than those shown in Figure 4.1.3. are also possible, if the length of the beam pulse (and thus, the maximum number of bunches per pulse) is reduced. This way, the problem of duty cycle limitation from the injector can also be mitigated. The essential limitation is the maximum pulse rate of the RF power stations, which cannot be arbitrarily increased even if the average power is kept constant. The upper limit for the repetition rate with short pulses is expected to be about 30 Hz at 17.5 GeV beam energy.

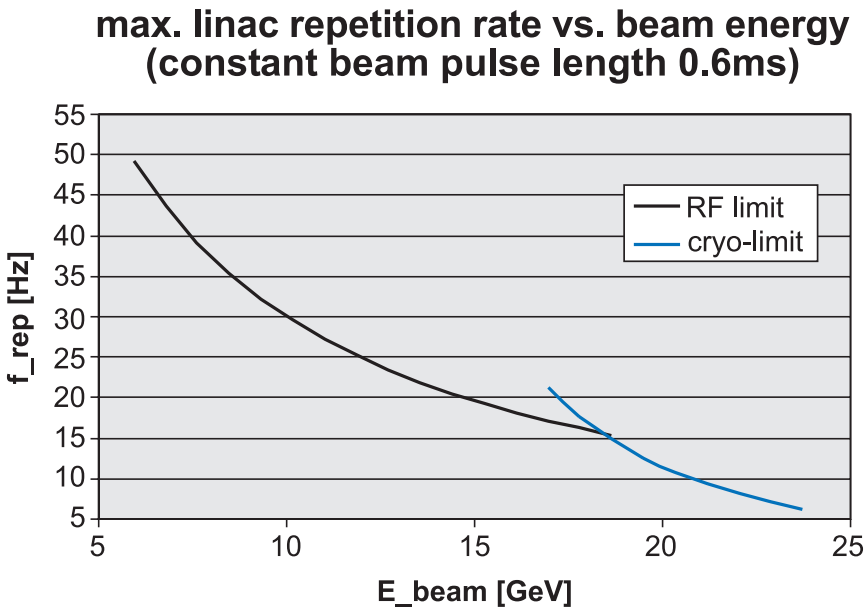

Figure 4.1.3 *Limitation of the linac repetition rate as a function of beam energy. A constant beam pulse length of 0.6 ms is assumed.*

4.1.3.3 Future option of CW operation

At sufficiently low beam energy, a 100% duty cycle, i.e. CW, mode of operation is conceivable, an option which is only possible with a superconducting linac. This option is viewed as not being part of the first stage of the X-Ray Free-Electron Laser (XFEL) Facility and can only be briefly discussed here. Continuous wave operation is not a possibility at full energy, because the cryogenic load would become excessive. If, however, experience with the SASE process at short wavelength and improvements of injector performance indicate that the 0.1 nm wavelength regime becomes accessible with electron beam energies around 6-8 GeV, the CW option could be very attractive since it allows optimisation of the beam time structure with experiments' requirements over a very large range. This is illustrated in Figure 4.1.4, where the pulsed machine is compared with a CW linac for the usable average bunch frequency as a function of the maximum bunch frequency which a certain experiment can tolerate (e.g. for detector or sample recovery time reasons). For example: an experiment needs a recovery time of 0.1 ms between photon pulses. With a CW linac, the experiment can operate at the full average bunch (=photon pulse) frequency of 10 kHz, whereas with a pulsed linac of ~1% duty cycle (and in principle maximum possible bunch frequency of 5 MHz), only ~100 Hz of average bunch frequency can actually be used.

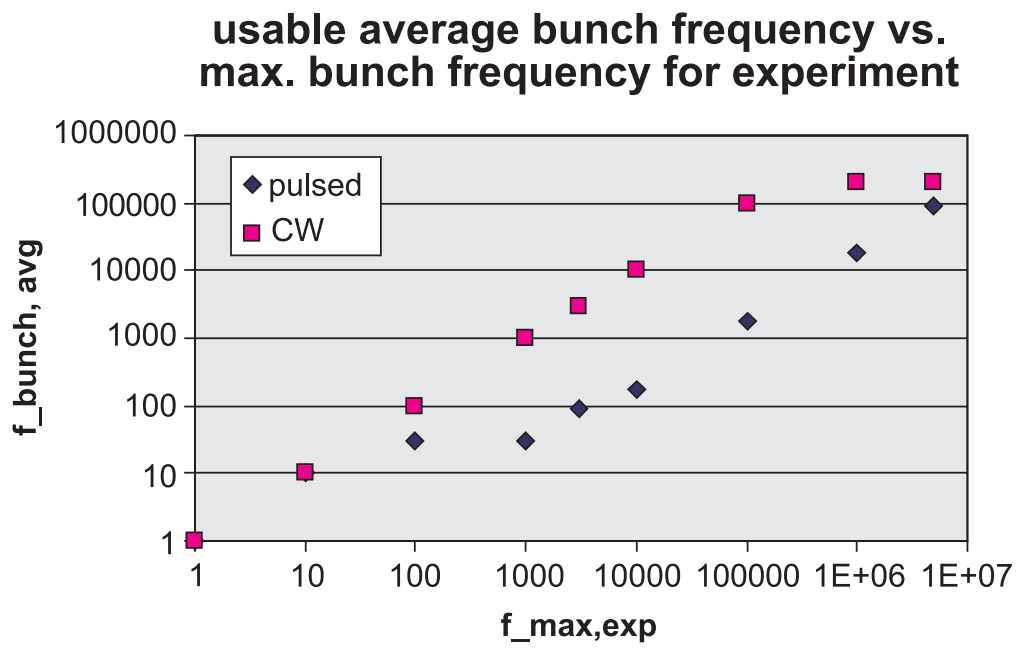

Figure 4.1.4 *Usable average bunch frequency against maximum tolerable bunch frequency for an experiment for a CW operation compared to the pulsed XFEL linac (see Section 4.1.3.3).*

A possible set of main parameters for operating the XFEL linac in CW mode is sketched in Table 4.1.2. The 2 K cooling capacity of the cryogenic plant would have to be approximately doubled for this option and a low power CW RF system would have to be added (space in the linac tunnel is available). With today's available technology, this would consist of one inductive output (IOT) device per accelerator module. As a result of the relatively low accelerating gradient, the external quality factor has to be increased by only a moderate factor compared to pulsed operation, cavity detuning due to microphonics is not a serious problem and much of the RF power could be fed to the beam instead of being needed mainly to stabilise the accelerating field.

Beam energy	7 GeV
Accelerating gradient	7.5 MV/m
Number of CW RF stations	116
RF power per accelerator module	≈20 kW
Beam current	0.18 mA
Loaded quality factor Q_{ext}	2×10^7
Bunch frequency	180 kHz
Unloaded quality factor Q_0	$2 \cdot 10^{10}$
2 K cryogenic load	≈3.5 kW

Table 4.1.2 *Sketch of possible parameters for a future option of operating the linac in CW mode.*

4.2 Linac

4.2.1 Cavities

4.2.1.1 Introduction

The XFEL accelerating cavity is a nine-cell standing wave structure of about 1 m length whose fundamental TM mode has a frequency of 1,300 MHz. It is identical to the so-called TESLA cavity **[4-1]**, made from solid Niobium, and is bath-cooled by superfluid Helium at 2 K. Each cavity is equipped with: a Helium tank; a tuning system driven by a stepping motor; a coaxial RF power coupler; a pickup probe; and two higher-order mode (HOM) couplers. The superconducting resonators are fabricated from bulk Nobium by electron-beam (EB) welding of deep-drawn half cells. The tubes for the beam pipes and the coupler ports are made by back extrusion and are joined to the cavity by EB welds.

		XFEL
Type of accelerating structure		standing wave
Accelerating mode		TM010, π-mode
Fundamental frequency	f_{RF} [MHz]	1300
Nominal gradient	E_{acc} [MV/m]	23.6
Quality factor	Q_0	$> 10^{10}$
Active length	L [m]	1.038
Cell-to-cell coupling	k_{cc} [%]	1.87
Iris diameter	[mm]	70
R/Q	[Ω]	1036
E_{peak}/E_{acc}		2.0
B_{peak}/E_{acc}	[mT/MV/m]	4.26
Tuning range	[kHz]	± 300
$\Delta f/\Delta L$	[kHz/mm]	315
Lorentz-force detuning constant	K_{Lor} [Hz/(MV/m)^2]	1
Q_{ext} of input coupler		4.6×10^6
Cavity bandwidth f/Q_{ext}	[Hz] FWHM	283
Fill time	[µs]	780
Number of HOM couplers		2

Table 4.2.1 *Parameters of the nine-cell cavity (note: $R = V^2/P$, where P is the dissipated power and V the peak voltage in the equivalent LCR circuit).*

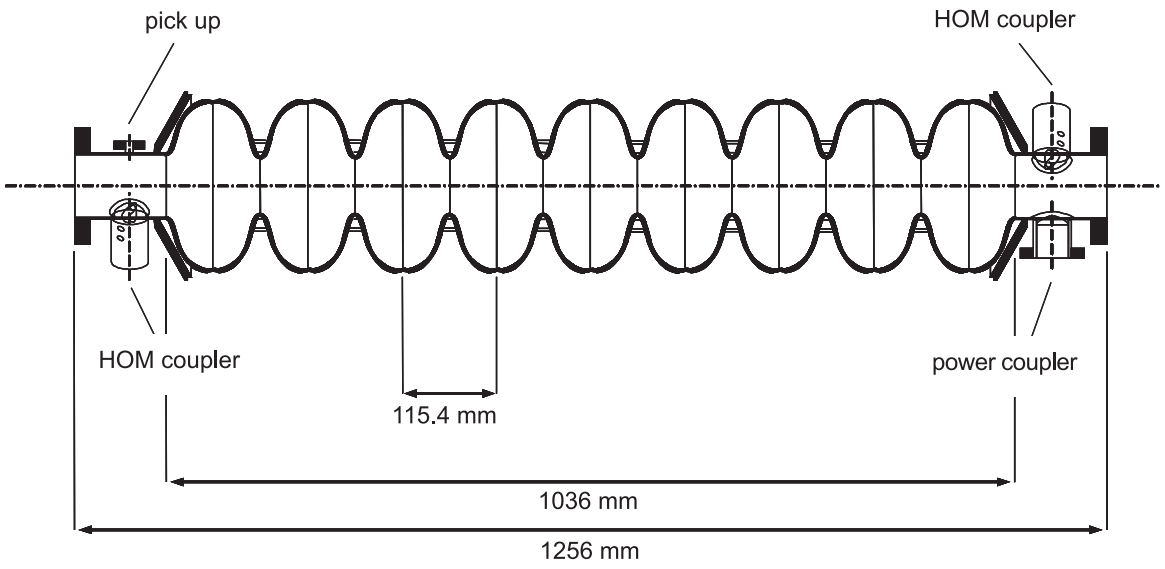

Figure 4.2.1: *Side view of the nine-cell cavity with the main power coupler port (right), the pick up probe (left), and two HOM couplers.*

4.2.1.2 Superconducting material and cavity fabrication

Niobium (Nb) with the highest critical temperature and critical magnetic field of all pure metals (T_c=9.2 K; superheating field of approximately 240 mT) is the favourite material for the fabrication of superconducting RF cavities. In addition, Niobium is chemically inert (at room temperature the surface is covered by a protecting pentoxide layer), it can be easily machined and deep drawn, and it is available as bulk and sheet material in any size. The majority of the RF cavities worldwide are formed from Niobium sheet material. There exist superconductors with a higher critical temperature and field, but in practice, cavities based on these materials have shown much inferior performance compared to Niobium cavities. The bulk Niobium is adopted as the material for XFEL cavities.

A high thermal conductivity in the cavity wall is needed (at least 10 W/m K at 2 K) to transfer the dissipated RF power to the liquid Helium coolant. For bulk Niobium cavities this requires Niobium of exceptional purity. The requirements of high purity Niobium are listed in Table 4.2.2.

The residual resistivity ratio (RRR=300 for XFEL cavities) is a common indicator of the purity level. The main interstitially dissolved impurities that act as scattering centres for unpaired electrons and reduce the RRR and therefore, the thermal conductivity, are Oxygen, Nitrogen, Hydrogen and Carbon. Oxygen is dominant due to the high affinity of Niobium to the Oxygen. The influence of Hydrogen on the RRR is not so significant, but the content of Hydrogen should be kept small (less than 3-5 µg/g) to prevent the hydride precipitation and degradation of the Q-value of the high RRR cavities under certain cool down conditions (Hydrogen Q disease).

Electrical and mechanical properties of Niobium		Content of the main impurities µg/g			
Residual Resistivity Ratio	> 300	Ta	≤ 500	H	≤ 2
Grain size	≈ 50 µm	W	≤ 50	O	≤ 10
Yield strength	> 50 N/mm^2	Mo	≤ 50	N	≤ 10
Tensile strength	> 140 N/mm^2	Ti	≤ 50	C	≤ 10
Elongation at fracture	> 30%	Fe	≤ 50		
Vickers hardness HV 10	≤ 60	Ni	≤ 50		

Table 4.2.2 *Technical specification for Niobium applied for the fabrication of 1.3 GHz superconducting cavities.*

Among the metallic impurities, Tantalum (Ta) has the highest concentration (500 µg/g). This element accompanies Niobium in most ores; modern separating methods are based on solvent extraction. The impurity level of 500 µg/g is normally harmless for cavities since Tantalum is a substitutional impurity and does not substantially affect the scattering mechanism. Next in abundance among substitutional impurities are metals such as Tungsten (W), Titanium (Ti), Molybdenum (Mo), Iron (Fe) and Nickel (Ni) usually at the level less than 30-50 µg/g.

Several remeltings in a high vacuum electron beam furnace allow purification of the Niobium ingot. Light elements evaporate during this process. Four to six melting steps are generally necessary to reach the RRR=300 level with few µg/g of interstitial impurities. The content achieved by melting should be maintained during fabrication and treatment.

The Niobium should be free of defects (foreign material inclusions or cracks and laminations) which will initiate a thermal breakdown. For example, Tantalum clusters are dangerous, as they could result in a normal-conducting spot **[4-2]**. An eddy current scanning device for defect diagnostics in Niobium sheets was successfully developed for TTF and will be applied for the XFEL **[4-3]**. A SQUID scanning system could be more sensitive and is currently in development. The acceptance test of the material includes the RRR measurement, microstructure analysis, analysis of interstitial and metallic impurities, hardness measurement, tensile test, examination of the surface roughness and defects diagnostic.

The fabrication procedure of XFEL cavities consists of the deep drawing and EB welding of the parts into a cavity assembly. This procedure is well established and has about 20 years of industrial fabrication experience. Half cells are produced from Niobium discs pressed into shape using a set of dies. The dies are usually fabricated from hard anodised aluminium alloy. For establishing the form of the deep drawing tools, the spring-back of the Niobium sheet material has to be taken into consideration. Deep drawing is sensitive to the mechanical properties of Niobium. In particular, small and uniform grain size (see Table 4.2.2) is essential, unless mono-crystalline sheets can be used (see the end of this section). The Niobium sheet must be annealed to achieve complete re-crystallisation, and to remove lattice defects, without growing large grains. Too large grains would result in a roughening effect during the forming process (“orange peeling”).

If the material is incompletely re-crystallised, it tears during deep drawing. Achieving good mechanical properties for high RRR Niobium requires the proper choice of annealing temperature and time. The final annealing of 2.8 mm thick Niobium sheets occurs normally at 750-800°C in a vacuum oven at a pressure of 10^{-5}-10^{-6} mbar for 1-2 h. Niobium also has a low degree of work hardening, which is advantageous for mechanical forming. In almost all cases when the proper mechanical properties of the sheet are achieved, cavity parts can be deep drawn to final shape without intermediate annealing. The accuracy of the half cell is controlled by 3D measurement and by sandwiching the half cell between two Niobium plates and measuring the resonance frequency.

The EB welding is done in several steps: The weld parameters are chosen to achieve full penetration. A slightly defocused beam in an elliptic pattern and using 50% beam power during the first weld pass and 100% beam power in the second pass, creates a smooth weld seam. Welding from the inside (RF-side) is recommended, wherever possible. Welds at the equator and iris of cells and at the HOM coupler parts are especially critical because they will be exposed to high magnetic or electric fields. Therefore, a thorough cleaning by ultrasonic degreasing, chemical etching, and ultra pure water rinsing and clean room drying is mandatory; absolutely clean conditions must be assured during welding. Touching the weld preparation area after the last cleaning must be strictly avoided. Since Niobium is a strong getter material for Oxygen, it is important to carry out the EB welds in a sufficiently good vacuum. Tests have shown that RRR300 Niobium has less than 10% RRR degradation by welding at a pressure lower than 5×10^{-5} mbar.

Two half cells are joined at the iris with an EB weld to form a dumbbell. This EB welding is usually done from the inside. The next step is the welding of the stiffening ring. The weld shrinkage may lead to a slight deformity of the cell which needs to be corrected. Afterwards, frequency measurements are made on the dumbbells to determine the amount of trimming at the equators.

The dumbbells are visually inspected. Defects and foreign material imprints from previous fabrication steps are removed by grinding. In state-of-the-art EB welding, the iris welds are very smooth, but it is still good practice to also perform the extra step of grinding the iris weld in order to ensure a smooth inner surface in this high electric field region and to avoid geometric field enhancement.

Beam tubes are either purchased as extruded seamless tubes or as rolled from sheet and EB welded. Flanges for the beam tubes are machined. Flanges are located in regions of low magnetic field and can be made from NbTi alloy (about 50%Ti).

After proper cleaning, eight dumbbells and two end group sections are assembled in a precise fixture to carry out the equator welds which are done from the outside. Experience has shown that all equator welds can be done in one production step (one evacuation of the EB chamber) without deterioration of the quality.

Use of an Engineering Data Management System (EDMS) for the complete documentation of the cavity fabrication process and the prompt exchange of all engineering information with the manufacturer will be required. This implies that all documents (inspection sheets,

specifications, drawings, etc.) which are created and maintained during the process of manufacturing the RF cavities, should be made available electronically in the EDMS. The complete information that must be reviewed by the manufacturer and approved by the client will be controlled by the system.

A potentially cost effective and more reliable cavity fabrication approach was recently proposed by colleagues of Jefferson Lab **[4-4, 4-5]**. High purity Niobium sliced directly from EB melted large grain ingot was used instead of Niobium sheets. Several single cell cavities deep drawn and EB welded demonstrated very promising performance. This approach might result in a possible cost saving option for fabrication of XFEL cavities. Several large grain Niobium single cells and 1.3 GHz nine-cell cavities will be produced, treated and RF tested.

4.2.1.3 Cavity preparation

Based on the standard preparation technique, (a buffered chemical polishing (BCP) followed by high pressure water rinsing), high acceleration gradients up to 30 MV/m were achieved at TTF **[4-6, 4-7]**. Encouraging results in cavity performance of 35-40 MV/m were gained in the cavity preparation with electropolishing in a collaboration of DESY and the KEK laboratories in Japan **[4-8]**. Thus, this newly established process has been chosen as the baseline.

For the XFEL, improved quality control measures for the fabrication of the resonators and the infrastructure for cavity preparation were introduced. The surface preparation relies on the removal of Niobium with electropolishing (EP) only. With this preparation, the post-purification with Titanium at 1,400°C can be avoided which leads to a cost reduction. Easier handling of the cavities due to their more favourable mechanical properties is also and advantage. The only remaining temperature treatment is an 800°C annealing.

The fundamental advantage of superconducting cavities is their extremely low surface resistance at 2 K, leading to RF losses which are five to six orders of magnitude lower than in Copper cavities. The drawback is that even tiny surface contaminations are potentially harmful as they decrease the quality factor and may even lead to a thermal breakdown/ quench of the superconductor due to local overheating. Perfect cleaning of the inner cavity surface is of utmost importance. Cavity treatment and assembly is, therefore, carried out in clean rooms conforming to semiconductor standards.

The cavity preparation for the XFEL industrial production is foreseen to be as follows:

- electrochemical removal of a thick Niobium layer (so-called damage layer) of about 150 µm from the inner cavity surface;
- a rinse with particle free/ultra-pure water at high pressure (~100 bar) to remove residues from the electrochemical treatment;
- outside etching of the cavities of about 20 µm;
- ultra-high vacuum annealing at 800°C;
- tuning of the cavity frequency and field profile;

- removal of a thin and final layer of about 30 µm prior to the low power acceptance test done in a vertical dewar;
- rinsing with particle free/ultra-pure water at high pressure (100 bar) to remove surface contaminants;
- assembly of auxiliaries (pick-up probe and HOM pick-up);
- baking at 120°C in an ultra-high vacuum;
- additional six times rinse with high pressure ultra-pure water (100 bar);
- low power acceptance test at 2 K temperature.

Application of the above techniques combined with extremely careful handling of the cavities in a clean-room environment led to acceleration gradients of more than 30 MV/m. The XFEL design gradient of 23.6 MV/m can be reproduced (and likely be exceeded) within one preparation sequence (see Section 4.2.2.4). The latter is an important aspect of the series production, where a cost increase by a reapplied treatment procedure has to be avoided.

Cavity treatment

A Niobium layer of in total 180 µm is removed in several steps from the inner cavity surface to obtain good RF performance in the superconducting state. At present, the standard method applied for material removal for XFEL test cavities at DESY is EP. An acid mixture of hydrogen fluoride (HF) (48%), and H_2SO_4 >96% mixed in a volume ratio of 1:9 is used. The acid is heated to 30-35°C and a constant voltage of 17 volts is applied between the electrode made from pure aluminum and the cavity body. Closed loop pumping of the acid through the cavity is used. After rinsing with ultra-pure water and drying in a class 100 clean-room, the cavities are annealed at 800°C in an Ultra-High Vacuum (UHV) oven to out-gas possibly dissolved Hydrogen and to relieve mechanical stress, introduced in the Niobium during deep drawing in the cavity fabrication.

After the heat treatment, the cavities are mechanically tuned to adjust the resonance frequency to the design value and to obtain equal field amplitudes in all nine cells. This is followed by a light EP of about 30 µm material removal, a rinse with water at high-pressure (100 bar), and drying in a class 10 clean-room. This surface treatment is followed by the assembly of HOM antennae, the RF pick-up probe, and a provisional input antenna for the low power acceptance test. Even if this is done under controlled clean-room conditions, the cavities are rinsed with high pressure water six times to remove particles that may be introduced during the assembly process. The final acceptance step is an RF test in a super fluid Helium bath cryostat, (the vertical dewar).

String assembly

A total of eight superconducting resonators completed by one superconducting quadrupole magnet package are combined to form a module string inside a clean-room. In order to do so, the cavities are disassembled from the test inserts and the field profile and frequency are adjusted before welding the resonators into their individual Helium container. Tank

welding takes place in a normal workshop area. A bead pull system that stays with the cavity until the end of this procedure is installed inside the clean-room to keep the resonator interior as clean as it was during the low power acceptance test. For the string assembly, the provisional input antenna gets replaced by the power coupler. Finally, the cavities are rinsed six times with ultra-pure high pressure water for removing particles that may be introduced during the assembly process.

The interconnection between cavities and the attachment to the quadrupole magnet package with its integrated beam position monitor are made in a class 10 clean-room by insertion of a bellows between the beam pipes of the individual components. During the assembly procedures the working area is monitored by air particle counters. An integral leak check finalises the string assembly before roll-out of the string for module assembly.

Diagnostic methods and quality control for cavity preparation

To ensure a reproducible cavity preparation, several diagnostic methods and quality control procedures are installed:

- Control of the ultra-pure water in use for the cavity rinses:

  The main ultra-pure water supply, as well as the point-of-use stations (tap connection), are controlled for particles by online measurements of the particulate contamination, the total oxidable carbon (TOC) content and the resistance of the water.

- The clean-room and process gases (Argon):

  The air and process gases Argon and Nitrogen underlie a general monitoring of particle contamination and air flow conditions (flow speed/flow direction). During the assembly procedures the working area is monitored by additional air particle counters. These data, taken at the point of work, are the basis of quality control of the assembly procedure.

- High pressure rinsing:

  To control the quality and efficiency of the high pressure rinses, the drain water, coming from the inside of the resonator, is conducted through a filter which is examined by a scanning light microscope to identify particulates.

4.2.1.4 Cavity performance

Radio frequency performance tests on the cavities are a crucial tool for quality control. The performance of the cavities is determined by measuring their “excitation curve”, i.e. the so-called quality factor Q as a function of the accelerating gradient. In first approximation, this quality factor Q is independent of the gradient. In a real cavity the non-perfect superconductor surface leads to a gradient dependence. The low power acceptance test done in a vertical bath cryostat at 2 K temperature includes the measurement of the “excitation curve” with its gradient limit, and the determination of the dark current onset caused by field emission.

Test setup for the acceptance test

The test infrastructure includes a bath cryostat and its auxiliaries needed to cool down the cavity to 2 K using liquid Helium. The RF measurement setup includes a low level RF feedback system based on a phase locked loop (PLL) to hold the RF generator's signal frequency equal to the resonance frequency of the cavity f_0. A solid state continuous wave (CW) 1 kW L-band RF amplifier is used to feed the cavity. Calibrated directional couplers and RF power meters are used to measure the forward, reflected and transmitted RF power. A digital scope, used together with logarithmical amplifiers, detects the signal's pulse shape (see Figures 4.2.2 and 4.2.3). Prior to the measurement, a low power calibration is done. This allows the calculation of the accelerating gradient E_{acc} from the transmitted (probe) power values. The cavity quality factor Q_0 is derived from the stored energy, the RF pulse decay time, and the measured RF power coupling coefficients.

During the test, multi-pacting[2] can occur at accelerating gradients of 17-22 MV/m. Conditioning is typically finished in less than half an hour. The usual gradient limitation is a thermal breakdown (called quench) caused by defects or inclusions heating up the cavity surface. X-rays can be produced by field emitted electrons due to a particulate contamination. These electrons are contributing to the dark current in the accelerator and increase the power dissipated inside the cavity. The consequence is a reduction in quality factor and, therefore, the emitted dark current can limit the cavity performance.

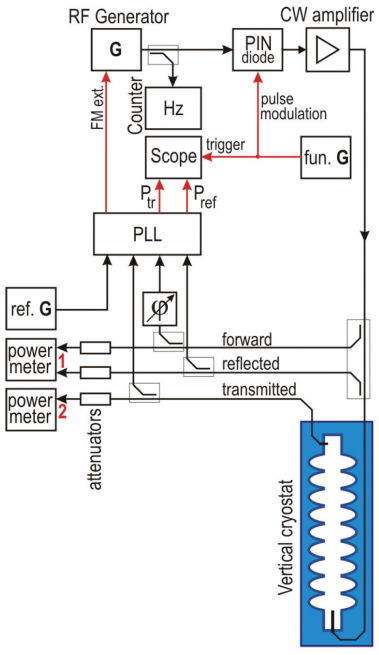

Figure 4.2.2 *Vertical cryostat cavity test diagram.*

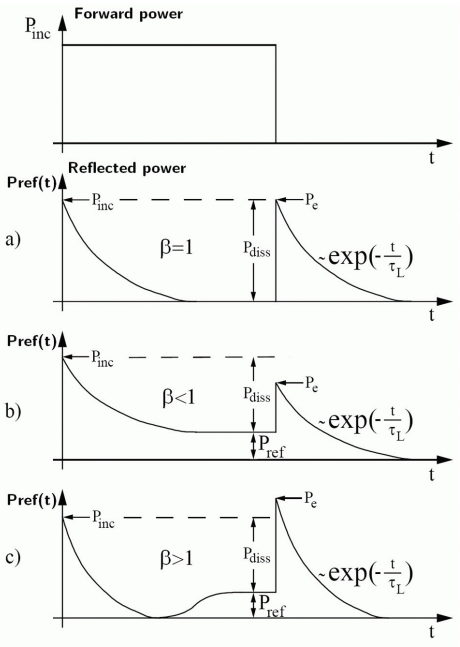

Figure 4.2.3 *Forward and reflected RF power pulses.*

[2] Multi-pacting = "Multiple impacting" – electrons emitted from the cavity surface are accelerated and hit the surface yielding secondary electrons. If the secondaries are generated in resonance with the RF frequency, an avalanche is generated. Processing reduces the secondary emission coefficient of the surface.

Results from acceptance test

As mentioned before, the envisaged XFEL surface preparation is based on EP and 800°C annealing. The classical cavity surface preparation uses a 1400°C post-purification and etching as described in **[4-6, 4-7]**. Electro-polishing offers prospects for significantly higher gradients (Figure 4.2.4) **[4-8, 4-9]**.

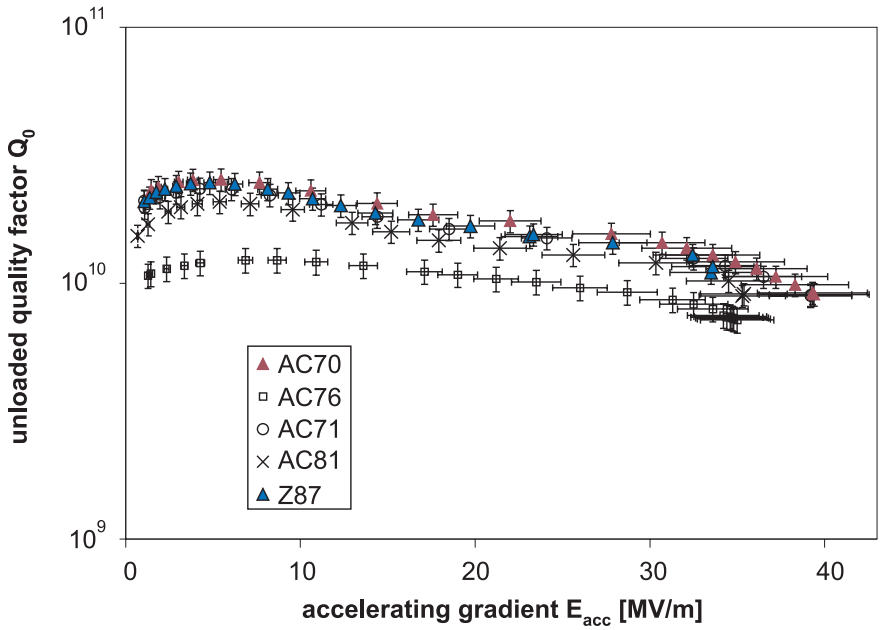

Figure 4.2.4 *"Excitation curves" of the best cavities treated with 800°C furnace treatment and EP. The XFEL baseline gradient of 23.4 MV/m is exceeded by a significant margin.*

Comparing the first performance tests on each cavity from both preparation techniques shows that the new XFEL procedure yields an average gradient of 28.4 +/- 3.6 MV/m at Q_0 of 10^{10}, whereas the classical procedure achieves 24.0 +/- 4.8 MV/m.

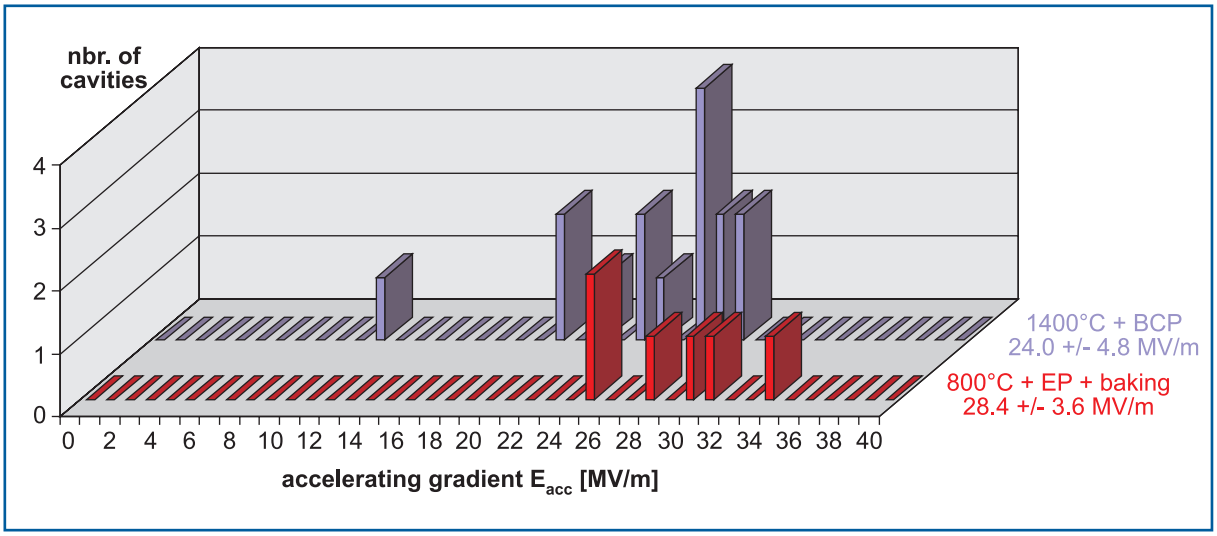

Figure 4.2.5 *Comparison of the accelerating gradients at $Q_0=10^{10}$ in the first performance test after the full preparation sequences using etching with post-purification at 1,400°C (blue) and EP with 800°C annealing (red).*

High power test set-up

A high power test of each individual cavity is done after assembly of the cavities into the accelerator module cryostats. In addition to that, a fraction of the cavities in production will be tested in an horizontal cryostat cavity test as a cavity qualification test done at 2 K in pulsed RF power mode (CHECHIA, **[4-10]**).

The goal of this test is to measure the performance of a resonator including all its auxiliaries such as main RF power coupler, HOM couplers, tuner and Helium tank. Done either in the completed module or in an horizontal test cryostat, the test conditions are identical with operation conditions in the linac, except for the electron beam.

The test infrastructure includes an L-band klystron to feed the cavity with pulsed RF power up to 1 MW. Calibrated directional couplers and RF power meters are used to measure the forward, reflected and transmitted RF power. A digital scope is used together with logarithmical amplifiers to obtain the signal's pulse shape. Prior to the measurement a low power calibration is done. This allows the calculation of the accelerating gradient E_{acc} from the transmitted (probe) power values. The cavity quality factor Q_0 is derived from the stored energy W and the cryogenic losses P_{loss}, measured as $Q_0 = 2\pi f_0 W / P_{loss}$.

The cavity operating mode as well as the HOM spectra and quality factors are measured to evaluate the HOM couplers' performance. The variable coupling factor of the main input coupler is checked for the whole antenna movement range and set to the aimed Q_{load} value of 4.6×10^6.

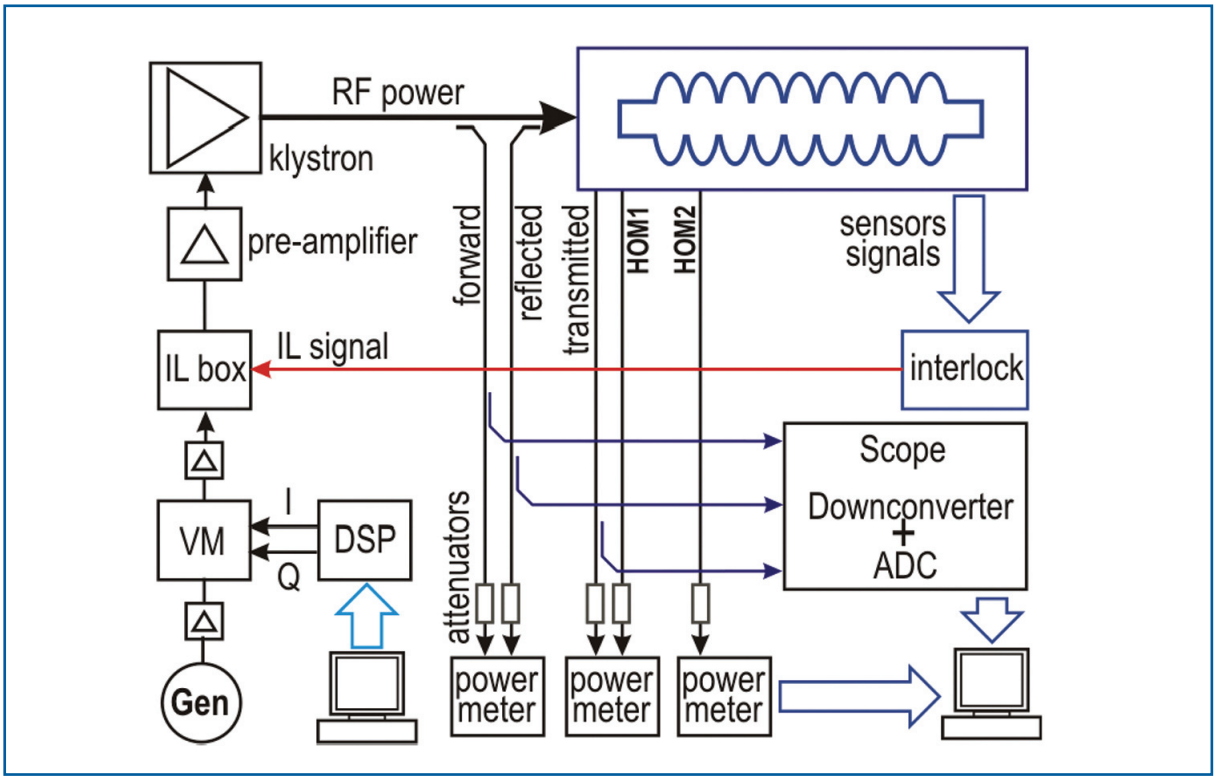

Figure 4.2.6 *Horizontal cryostat cavity test diagram.*

The test is done in three major steps:

1 The main RF power coupler is conditioned with the cavity being off resonance; this is done at room temperature.

2 Coupler and cavity are then conditioned with the cavity being on resonance at 2 K.

3 The Q_0 vs. E_{acc} measurement is done during 'flat-top' pulse operation; the cavity performance limit is investigated.

The power coupler off-resonance conditioning is carried out for pulse lengths of 20, 50, 100, 200, 400 µs with RF power up to 1 MW, and for pulse lengths of 800 and 1,400 µs up to 600 kW. On-resonance conditioning uses rectangular pulses up to the length of the cavity filling time (780 µs), and for longer pulses (up to 1.4 ms) with a reduced forward power in order to keep the cavity gradient constant during the pulse[3]. During the last stage the cavity quality factor is determined measuring the cryogenic losses at various accelerating gradient values up to the cavity limit. The x-rays associated with the dark current are measured in addition.

[3] Cavity conditioning might include high peak power processing (HPP) done with the pulse lengths of 100-1300 µs up to the cavity breakdown or the 1 MW power limit. The HPP procedure can help to remove the existing cavity electron emitters by applying the short high RF power pulses. **[4-11]**

High power test results

The accelerating fields achieved in the vertical and the horizontal tests are well correlated **[4-8, 4-6]**. In a few cases a reduced performance was seen, usually caused by field emission. Several cavities improved their performance in the horizontal test because of operation with short (millisecond) pulses instead of the CW operation in the vertical cryostat. The results show that the good performance of the cavities is maintained by taking care to avoid dust contamination during the mounting of the Helium vessel and power coupler. The ultimate performance test of the cavities is done after assembly of the cavity string and their installation into the accelerator module cryostat vessel. The experience obtained at TTF with the accelerator modules is summarised in Figure 4.2.7.

As can be seen, the latest generation accelerator modules (M4 and M5) have operational gradients above the baseline gradient for the XFEL. The expected performance from the acceptance test could be transferred to the fully assembled modules for these modules. For some of the TTF accelerating modules this is not the case. The performance degradation in those modules is partially linked to the different scheme of cavity positioning used as well as to missing quality control procedures in the earlier string and module assemblies.

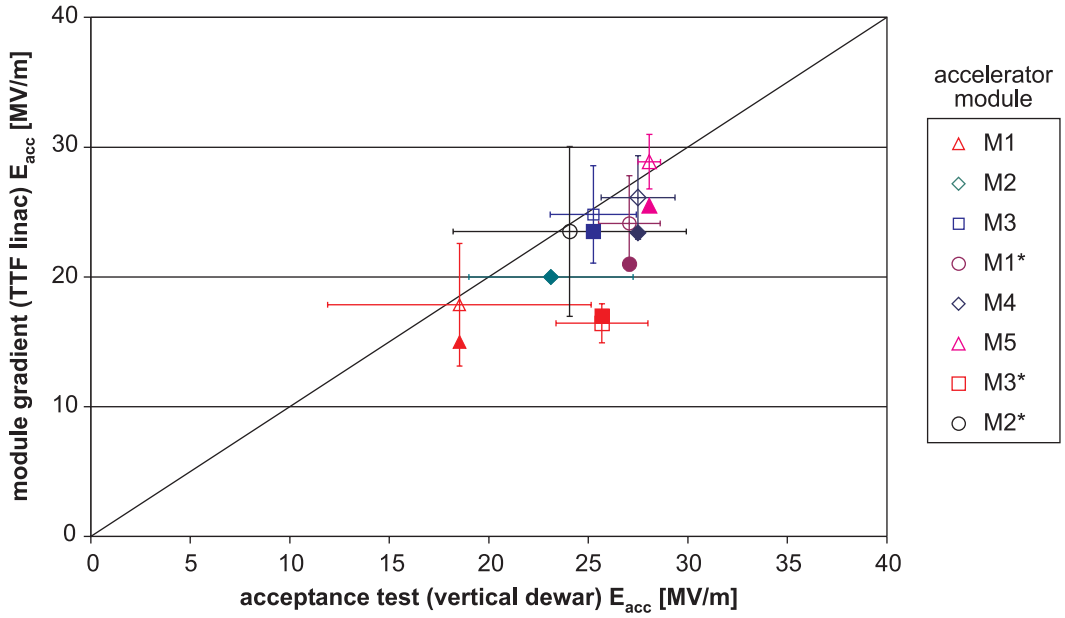

Figure 4.2.7 *Performance of the TTF accelerator modules. The plot shows the average maximum gradient in the accelerator modules against the average gradient achieved in the acceptance tests at $Q=10^{10}$ (open symbols). In addition, the operational gradient of the modules is plotted against the acceptance test gradient (closed symbols) which is based on equal RF power feeding.*

4.2.2 Auxiliaries

4.2.2.1 Main power coupler

The XFEL linac coaxial RF power input coupler has been developed **[4-12, 4-13]** consisting of a cold section which is mounted on the cavity in the clean-room and closed by a ceramic window, and a warm section which contains the transition from the coaxial line to the waveguide. This section is evacuated and sealed against the air-filled wave guide (WR650) by a second ceramic window (see Figure 4.2.8). The elaborate two-window solution was chosen for additional protection of the cavity against contamination during mounting in the accelerator module, and against a window fracture during linac operation.

Bellows in the inner and outer conductors of the coaxial line of the coupler allow a few mm of motion between the cold mass and the vacuum vessel when the cavities are cooled from room temperature to 2 K. A low thermal conductivity is achieved by using stainless steel pipes and bellows with a 10-30 µm Copper plating at the radio frequency conducting surface. Lower values than the design heat loads of 6 W at 70 K, 0.5 W at 4.5 K and 0.06 W at 2 K have been achieved in practice.

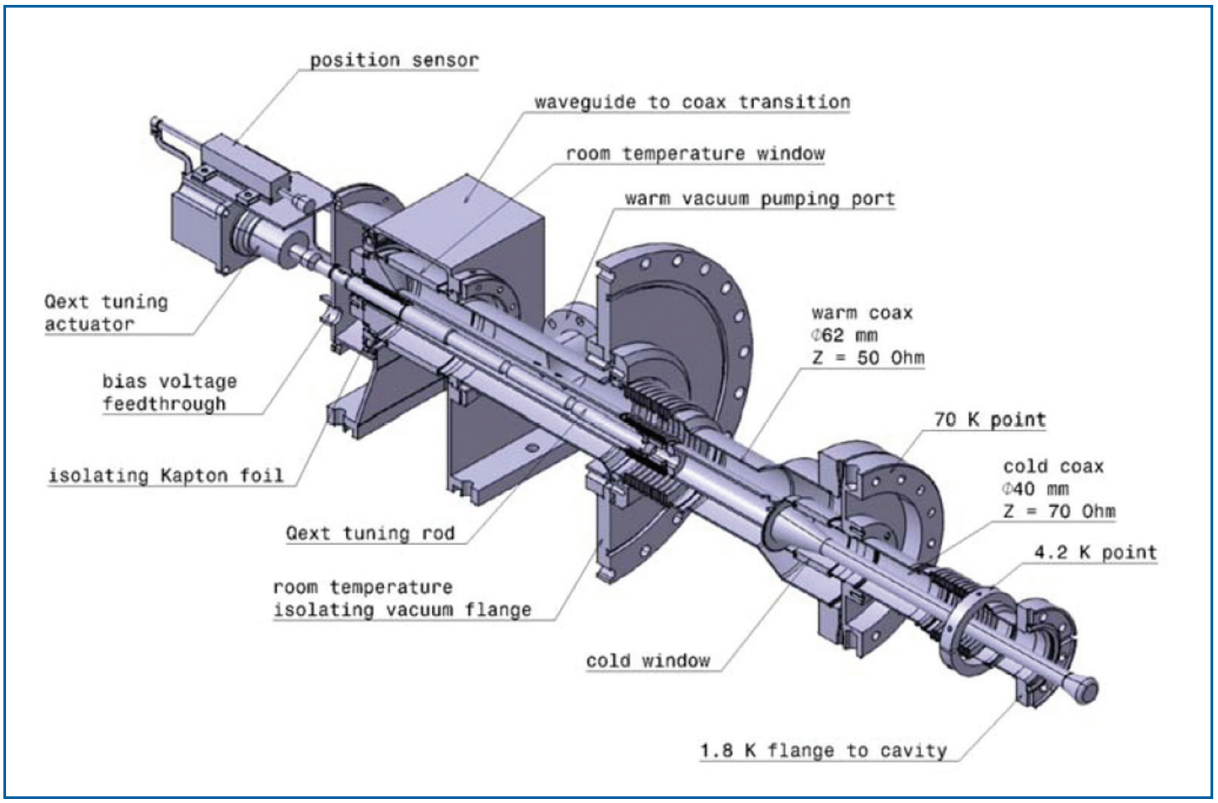

Figure 4.2.8 *The coaxial power input coupler for the XFEL linac cavities. The coaxial part is thermally connected to the 4.5 K and 70 K radiation shields of the cryostat. The input antenna is movable to vary Q_{ext} in the range 10^6 – 10^7.*

The coupler features two cylindrical Al_2O_3 windows which are insensitive to multi-pacting resonances according to the simulations, and are coated with Titanium nitride to reduce the secondary electron emission coefficient **[4-14, 4-15, 4-16]**. The coaxial line is also insensitive to multi-pacting resonances. A further suppression is achieved by applying a DC bias voltage (up to 5 kV) to the inner conductor.

At 20 GeV beam energy, an instantaneous power of 120 kW has to be transmitted to provide a gradient of 23.6 MV/m for a 600 µs long beam pulse of 5 mA. The maximum RF pulse length is 1.38 ms, the filling time of the cavity amounts to 720 µs. The repetition rate is 10 Hz (1.37% duty cycle) and the average power amounts to 1.6 kW. The external quality factor of the coupler is $Q_{ext} = 4.6 \times 10^6$ at 23.6 MV/m. By moving the inner conductor of the coaxial line, Q_{ext} can be varied in the range 10^6-10^7 to cope with different beam loading conditions and to facilitate an in-situ high power processing of the cavities at RF power levels up to 1 MW. This feature has proven to be extremely useful on several occasions to eliminate field emitters that entered the cavities at the last assembly stage. The continuous wave (CW, 100% duty cycle) operation, as an XFEL upgrade option, with an accelerating gradient of 7 MV/m and a beam current of 0.18 mA would need 2.5 kW of CW power for the coupler, including regulation overhead; it will take advantage of using tunable Q_{ext}.

All couplers must be conditioned in order to perform according to specifications. During experimental tests at TTF, the couplers were able to transmit up to 1.5 MW of peak pulsed RF power at 2 Hz repetition rate in travelling wave mode on the coupler test stand, and 600 kW at 5 Hz repetition rate in standing wave mode with cavities operated at 35 MV/m in a horizontal test cryostat (2,400 hours of operation, 2.5 kW of average RF power) **[4-8]**.

4.2.2.2 Damping of higher-order modes (HOM)

The spectrum of the electron bunch reaches very high frequencies up to 5 THz due to the short length $\sigma_z = 25$ µm of the accelerated bunches. The integrated longitudinal loss factor of the accelerator module housing eight nine-cell cavities is 135 V/pC and the total power deposited by the nominal beam (30,000 bunches/s) in an accelerator module is 5.4 W if no resonant excitation takes place **[4-17]**. Its distribution for various frequency ranges is shown in Figure 4.2.9. Two types of devices, HOM couplers and beam pipe absorbers, are proposed for extracting this power from the 2 K environment. Modes below the cut-off frequency of the interconnecting beam tubes (non-propagating part of the spectrum) will be suppressed by the HOM couplers **[4-18]** of which two will be attached to the end beam tubes of each cavity. The HOM couplers, based on the coaxial line technique (Figure 4.2.10) will also suppress non-propagating modes in case of their resonant excitations.

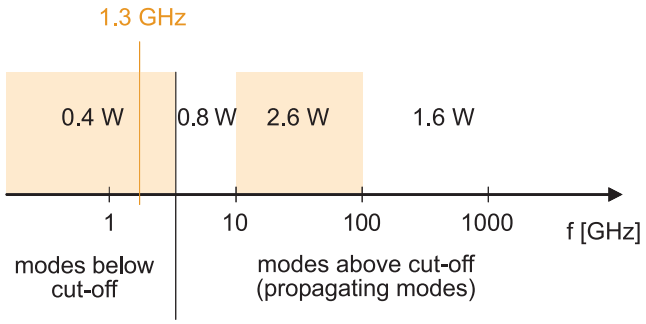

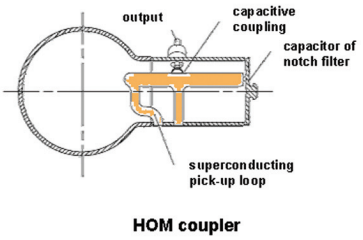

Figure 4.2.9 *HOM power distribution against frequency for the nominal pulse operation.*

Figure 4.2.10 *HOM coupler.*

A large proportion (~80%) of the propagating power will be dissipated in the beam pipe absorbers (Figure 4.2.11) to mitigate additional cryogenic load at 2 K. These devices installed between accelerator modules will absorb the power in the lossy ceramic rings and transfer generated heat to the 70 K environment.

In the beam pipe absorber and HOM coupler designs we take into account a possible upgrade of the XFEL Facility to higher average brilliance by operating it with more bunches in CW or near-CW modes **[4-19]**. For this, the absorber power capability has been specified to be 100 W which will allow for acceleration of up to one million nominal bunches per second. Even for this high power, good heat conductivity of the chosen ceramic keeps the temperature gradient across the ceramic ring below 140 K. Several performed tests confirmed that this gradient does not change the mechanical and RF properties of the absorber. The HOM couplers will be equipped with high heat conductivity feedthroughs (as compared to those used at present for the TTF cavities) allowing their Niobium output probes to be kept in the superconducting state, so avoiding additional cryogenic load at 2 K.

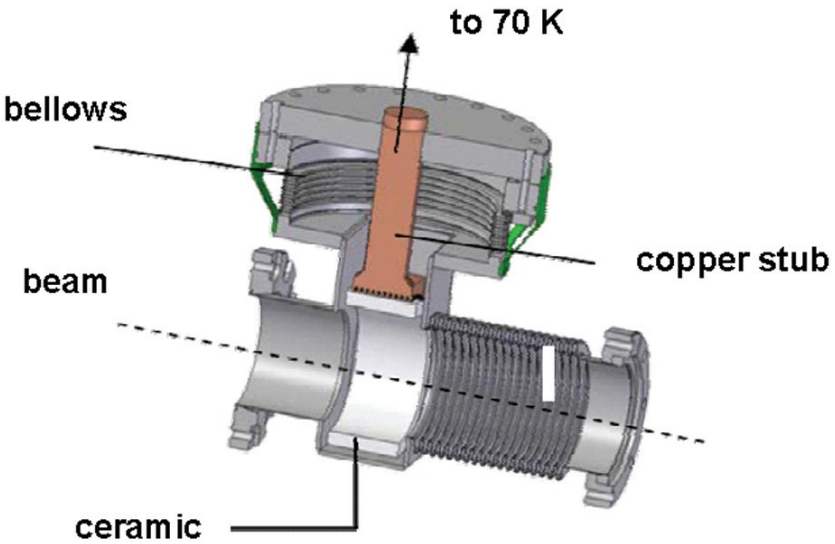

Figure 4.2.11 *Layout of the beam pipe absorber.*

4.2.2.3 Helium vessel and tuning system

The cavity is welded into a cylindrical vessel which contains the superfluid Helium needed for cooling and serves as part of the tuning mechanism. The vessel is made from Titanium whose thermal contraction is almost identical to that of Niobium. A Titanium bellows allows the length to be adjusted by the mechanical tuner.

Slow tuner

Tuning the cavity to its nominal operating frequency is a challenging task since the cavity length must be adjusted with sub-micron accuracy. The tuning system used at TTF consists of a stepping motor with a gear box and a double lever arm. The moving parts operate at 2 K in a vacuum. The frequency tuning range is about 400 kHz with a resolution of 1 Hz. The tuners in the TTF linac have been working since 1997 with high reliability. The tuner for the XFEL is based on a tuner design used for 1.5 GHz cavities built by CEA Saclay **[4-20, 4-21]**, and being in operation at the ELETTRA and PSI synchrotron light sources. The new design will be stiffer than the TTF tuner, using a double lever with a screw-nut system. In contrast to the TTF design, the cavity is stretched by the tuner. This has the advantage that the piezo elements are compressed under all circumstances (see Figure 4.2.12).

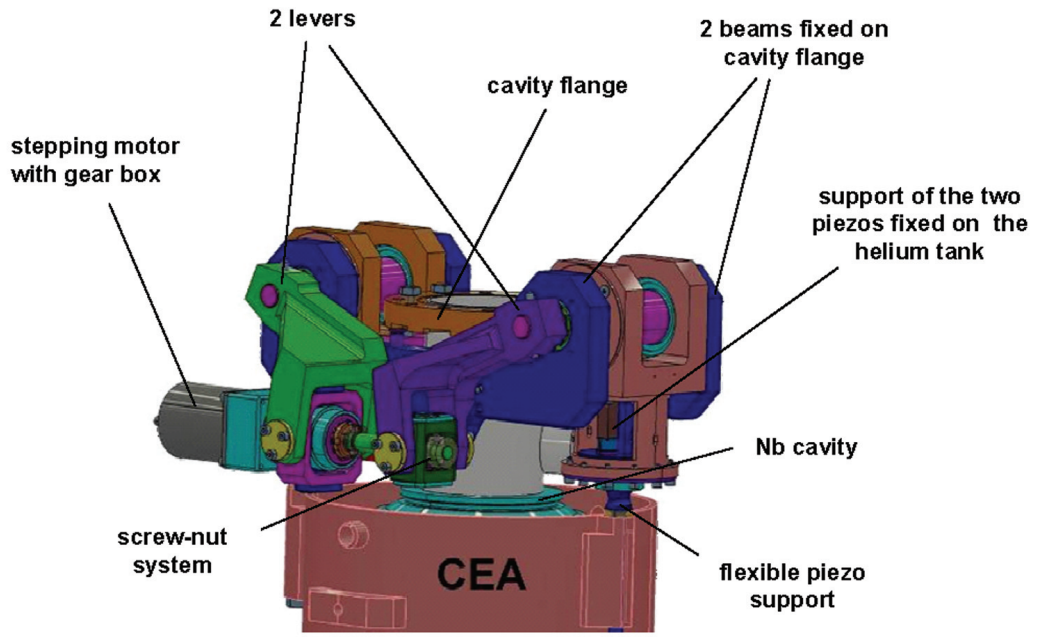

Figure 4.2.12 *Overview of the tuner design for the XFEL.*

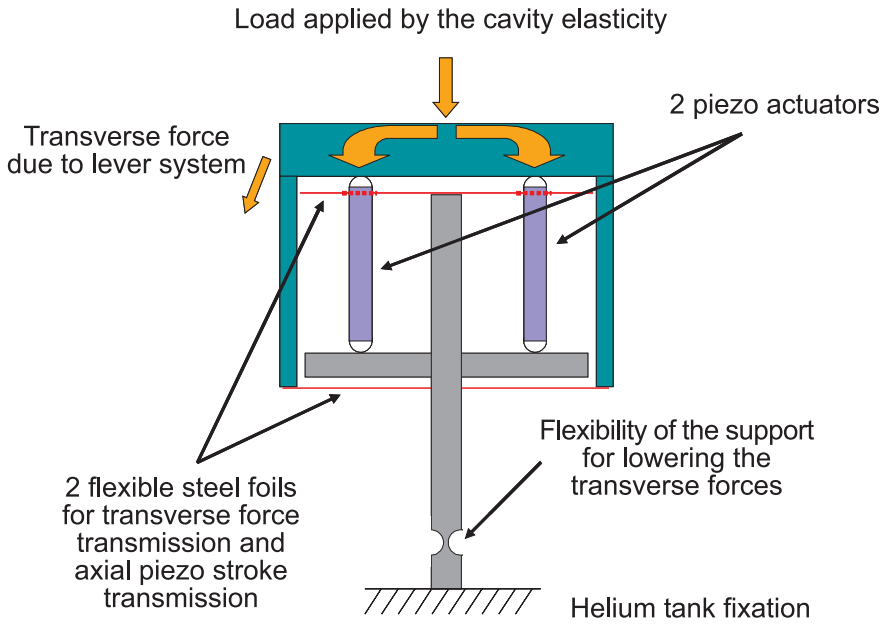

Figure 4.2.13 *The principle of operation of the fast piezoelectric elements* **[4-21]**.

Frequency stability of the cavities within an RF pulse (fast tuner)

The pulsed operation leads to a time-dependent frequency change of the nine-cell cavities. The stiffening rings joining neighbouring cells are adequate to keep this so-called "Lorentz-force detuning" within tolerable limits up to the nominal XFEL gradient of 23.6 MV/m.

To allow for higher gradients and to further improve frequency stabilisation, the cavity deformation must be compensated for. This approach has been successfully demonstrated using a piezoelectric tuner **[4-8, 4-21]** (see Figure 4.2.14). The result indicates that the present stiffening rings augmented by a piezoelectric tuning system will permit efficient cavity operation for all operation modes of the XFEL. In addition, for lower gradients the frequency of the cavities can be stabilised to a few Hz leading to a better phase stability during the RF pulse **[4-22, 4-23]**.

The principle of the new XFEL tuner is based on the fact that the preload is directly applied on the piezo actuators by the cavity elasticity. No additional force is applied by the support of the piezo elements. With this concept, the preloading of the piezos can be predicted in a more precise way, which is an important improvement compared to the TTF tuner. A prototype system is currently being tested at CEA and DESY.

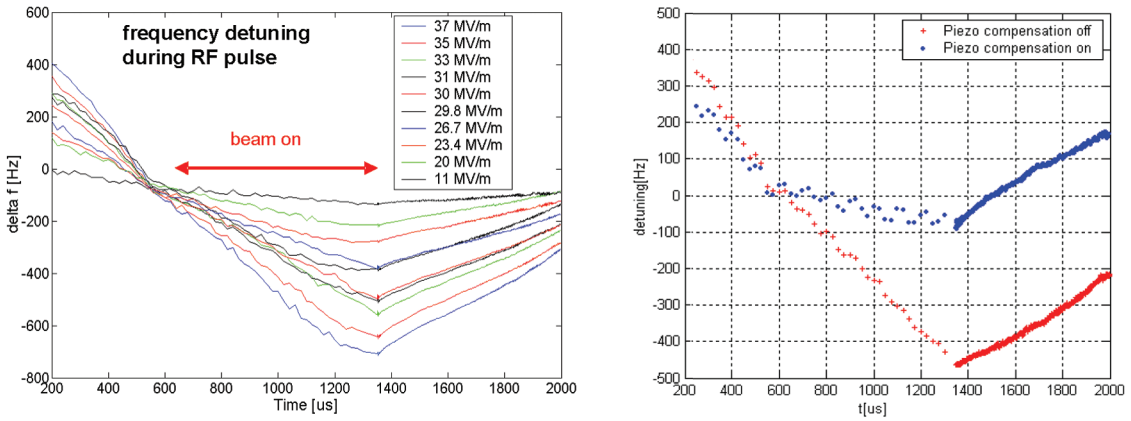

Figure 4.2.14 *Lorentz-force detuning in pulsed mode operation at gradients from 11 to 37 MV/m (left). High-power pulsed test at 35 MV/m of an EP nine-cell cavity. The measured detuning during cavity filling and "flat top" at 35 MV/m with and without piezo-electric compensation.*

4.2.2.4 Accelerator module (cryomodule)

The design of the accelerator module described here is based on the third cryomodule generation for the TTF. Two of these so-called type-3 modules have been successfully tested and operated in the TTF linac since March 2003. The length of the type-3 module is 12.2 m, the total weight 7.8 t, (2.8 t for the cold mass and 5 t for the vacuum vessel). Its major components are:

- a Carbon steel vacuum vessel with a standard diameter of 38";
- a 300 mm Helium Gas-Return-Pipe (GRP) acting as a support structure, together with three adjustable posts on top of the vacuum vessel. The middle post is the fixed-point but, the outer posts can slide in a longitudinal direction, because during-cool down the ends of the 12 m long GRP move by up to 18 mm towards the centre of the module;
- a 2 K forward line transferring single phase Helium, a 2 K two phase line connected to the cavity Helium vessels, a 5-8 K forward and return line, a 40/80 K forward and return line, and a warm-up/cool-down line with capillaries to the bottom of each cavity vessel;
- Aluminum thermal shields with stiff upper parts for 4 K and 40/80 K with 10 layers of super-insulation (MLI) for 4 K and 30 layers for 40/80 K, attached to the support structure;
- eight completed cavities and one beam position monitor (BPM)/magnet unit, attached to the GRP;
- the cavities and BPM/magnet unit can be aligned individually. To keep the cold coupler head of each cavity fixed within 2 mm, each cavity is anchored to a long Invar rod attached to the longitudinal centre of the GRP at the middle post. In addition, the cavity and magnet Helium vessels and GRP are wrapped with 10 layers MLI to reduce the heat transfer in the event of vacuum failure;
- manually operated valves to terminate the beam tube at both ends;
- a HOM-Absorber is part of the beam pipe and installed next to the BPM/magnet unit;
- four C-shaped stainless steel elements clamp a Titanium pad welded to the Helium tank. Rolling needles drastically reduce the longitudinal friction. The cavities are independent from the elongation and contraction of the HeGRP.
- lateral and vertical position the are defined by reference screws. The longitudinal position can be fixed by the use of an Invar rod.

Well defined procedures to prepare the individual components, guide the assembly and installation, and test the linac cryogenic operation of an accelerator module, are available. Already 10 accelerator modules have been built and successfully commissioned for the TTF linac during the last ten years.

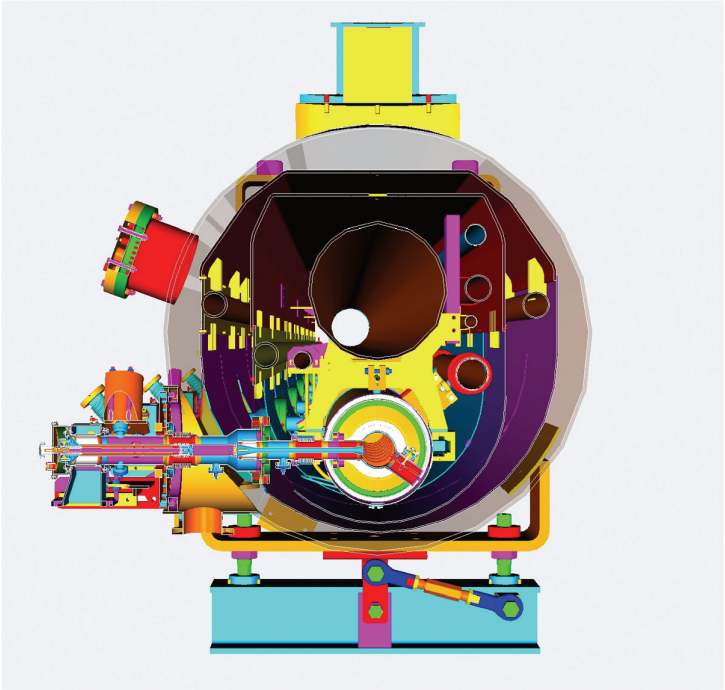

Figure 4.2.15 *Cross-section of a type-3 cryomodule.*

The type-3 cryomodule meets nearly all the requirements of the XFEL modules, with the following exceptions:

- the cold magnet will be operated at 2 K (now up to 4 K at TTF) with conduction cooled current leads; the cold magnet and BPM will be one unit; at the XFEL, the 4 K circuit raises up to ~8 K temperature;
- a HOM-Absorber will be placed in module interconnection with 40/80 K cooling; the maximum cooling capacity is laid out for a future CW-operation of the XFEL linac;
- a modified cavity frequency tuner with fast (piezo) tuning will be used;
- the cavity-to-cavity spacing will be corrected to be exactly one RF wavelength. Shortening the cryomodule length by 230 mm allows for an inter-module cavity-to-cavity spacing of a multiple of the RF wavelength.

These necessary modifications are on the way and will be introduced and tested in two further accelerator modules (M8 and M9) of the so-called cryomodule type-3+ in November/December 2006. Industrial studies for the assembly of modules in later series production have been launched.

Module performance	Module 4	Module 5	XFEL specification
RF gradient			**reached**
Design	>24 MV/m	>25 MV/m	23.6 MV/m
Measured	average >26 MV/m	average >29 MV/m	
Dynamic cryo losses 2 K			**reached**
25MV/m 5Hz 500/800µs			
Design	3.0 W (Qo=1E10)	3.0 W (Qo=1E10)	3.0 W (Qo=1E10)
Measured	2.3 W Qo=1.3E10	2.0 W Qo=1.7E10	
Static cryo losses			**reached**
2K/4K/40-80K			
Design	4.2/21.0/12 W	4.2/21.0/112 W	4.2/21.0/112 W
Estimated	2.8/13.9/77 W	2.8/13.9/77 W	
Measured	<3.5/13.5/74 W	<3.5/13.5/74 W	
Number of leaks	0	0	**reached**
He → insulation	0	0	
He → beam pipe	0	0	
Insulation → coupler	0	0	
Insulation → beam pipe	0	0	
Coupler → beam pipe	0	0	
Alignment x/y inside			**reached**
Cavities design x/y	+0.5/-0.5 mm (peak)	+0.5/-0.5 mm (peak)	+-0.5mm (rms)
measured x	+0.32/-0.19 mm	+0.35/-0.32 mm	
measured y	+0.10/-0.35 mm	+0.2/-0.1 mm	
Magnet/BPM design	+0.3/-0.3 mm (peak)	+0.3/-0.3 mm (peak)	+-0.3 mm (rms)
measured x	+0.10/-0.05 mm	+0.15/-0.05 mm	
measured y	+0.35/-0.05 mm	+0.20/-0.05 mm	
Alignment z inside			**reached**
Coupler antenna design z within 2 mm	within 2 mm		within 2 mm
Measured z x-ray	within < 2 mm	within <2 mm	

Table 4.2.3 *Comparison of cryomodule type-3 parameters (after two thermal cycles) with the XFEL specifications.*

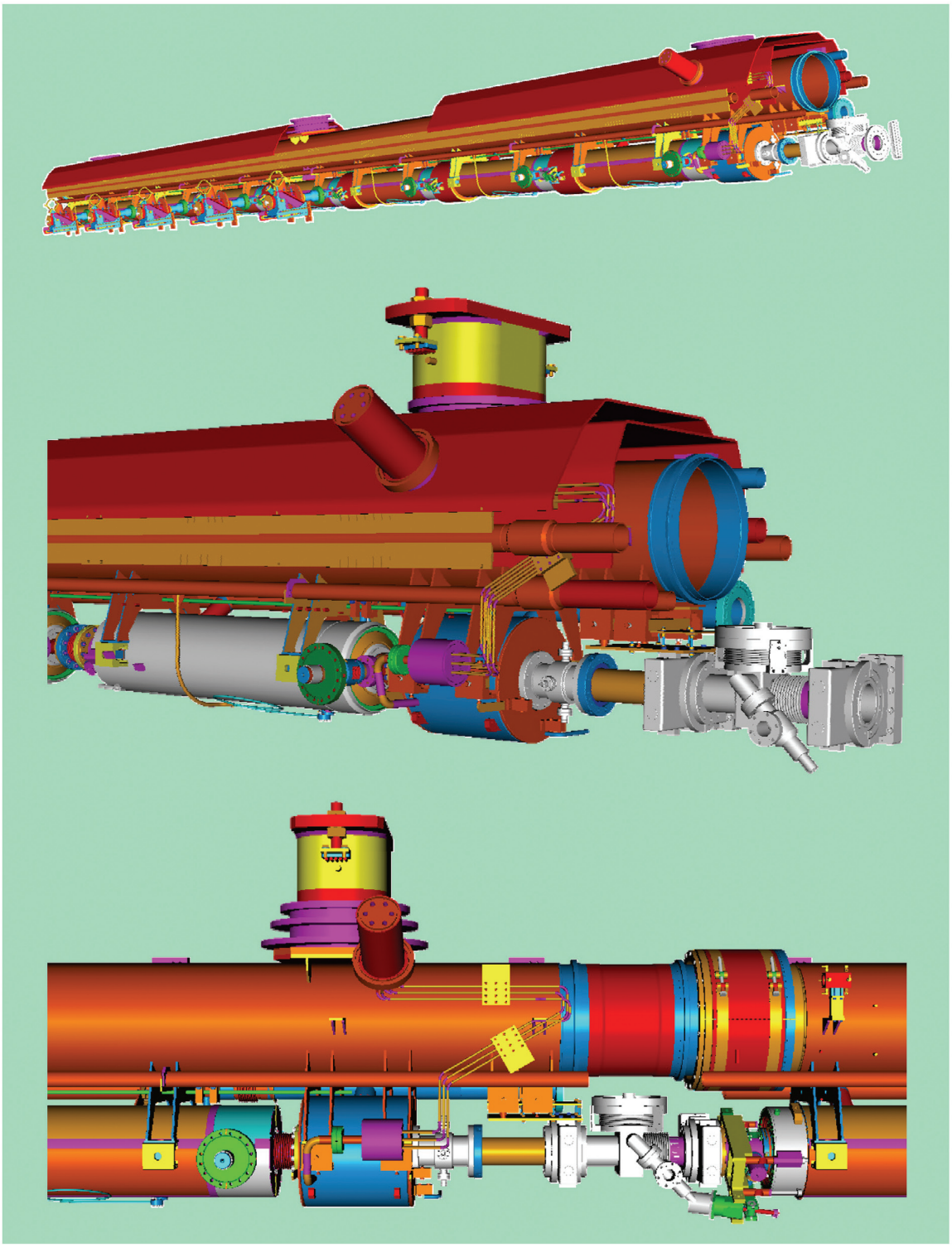

Figure 4.2.16 *CAD cut-away view of the type-3+ cryomodule.*
Top: Cold mass with cavities, BPM/magnet, HOM-Absorber beam pipe valve.
Middle: End group of a module.
Bottom: Module-to-module connection.

4.2.2.5 *XFEL magnet package and cold beam position monitor*

At the downstream end of the cavity string of each XFEL accelerator module, a magnet package and an attached BPM is placed (see Figure 4.2.17). The magnet package contains three independent superconducting magnets: a super-ferric quadrupole magnet, a vertical and a horizontal dipole magnet. A detailed parameter list is given in Table 4.2.4 and Table 4.2.5.

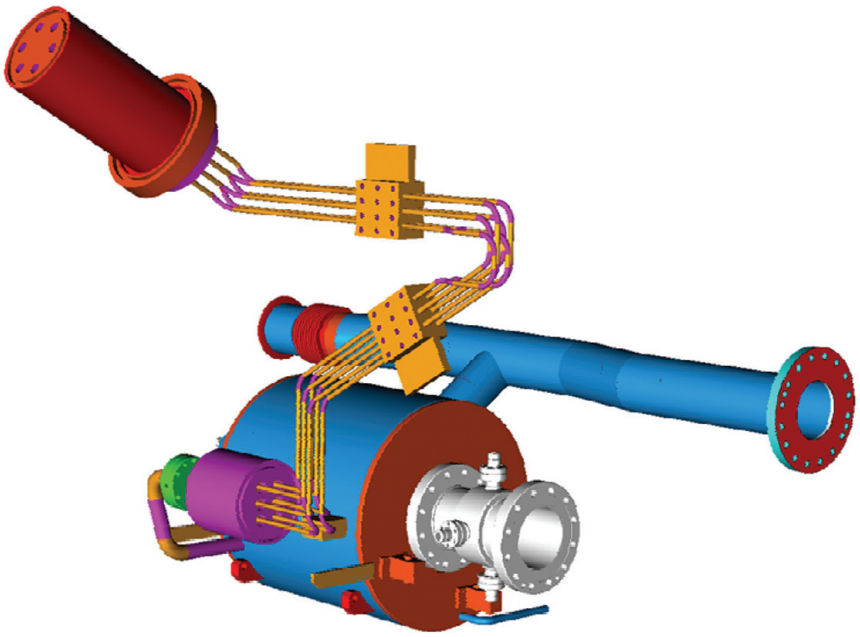

Figure 4.2.17 *Schematic view of the magnet package, the BPM and the current leads.*

A super-ferric magnet design has been selected for the quadrupole because a magnet with a low gradient can be best realised with a conventional Iron-based design using a superconducting coil allowing the integration into the 2 K liquid Helium volume in the XFEL accelerator module. The correction magnets are single layer cos-Θ type coils which are directly mounted on the beam pipe. The beam pipe itself is the inner wall of the Helium vessel. In order to avoid flanged connections, the vessel is made of Titanium. This allows welding connections to the cavity tank (also made of Titanium). Iron mirror plates at both magnet ends inside the Helium vessel are included to minimise the stray field outside the magnet and prevent magnetic field penetration into the cavity area. The magnet and cryostat design are done in collaboration with CIEMAT **[4-24]**.

Two different types of BPMs are under discussion: the SACLAY design is described in **[4-25]**, the DESY design is shown in Figure 4.2.17. The connection between the BPM and the magnet package is the same type as the connections between the cavity tanks. The axial space is limited to 170 mm.

Magnet support and alignment with the BPM

The magnet package is hanging at the 300 mm tube using a bearing system to allow axial movement of about 30 mm during cool-down. The axial position, relative to the central post, is kept constant by connecting the magnet package to the Invar rod. The bearing play is minimised by a spring-loaded support.

For machine operation it is important to know the relative position of the quadrupole with respect to the BPM. The required tolerance for the axis differences is 0.3 mm and it is 3 mrad for the roll angle difference. In order to fulfil these requirements, two dowel pins are used. The position for the boreholes of the dowel pins at the quadrupole flange will be calculated from warm magnetic measurements (Δx, Δy and α) and will then be transferred to the quadrupole flange. By this procedure an arbitrary selection of magnet packages and BPMs is possible. To follow this procedure one has to ensure that the deviation of the mechanical and magnetic axes and roll angle of the magnet package is within ±0.4 mm and 6.5 mrad respectively, given by the difference of the bore hole diameter of the BPM flange and the bolt diameter.

		Quadrupole magnet
Winding type		Super-ferric
Iron yoke inner diameter	[mm]	94.4
Iron yoke outer diameter	[mm]	270
Nominal current	[A]	50
Nominal gradient	[T/m]	35
Magnetic length	[mm]	166.5
Number of turns		646 (34x19)
Wire diameter (bare/insulated)	[mm]	0.4/0.438
Copper to superconductor ratio		1.35
RRR		>70
Filament diameter	[micron]	35
Twist pitch	[mm]	50
Iron yoke length	[mm]	140
Coil length	[mm]	200.6
Stored magnetic energy at 50 A	[J]	1439
Self inductance	[H]	1.15
Integrated gradient at 50 A	[T]	5.828
Integrated b6 at 50 A	10^{-4} × b2 at 30 mm	1.34
Integrated b10 at 50 A	10^{-4} × b2 at 30 mm	-1.10
Coil peak field	T	2.47
Integrated gradient at 5 A	T	0.6284
Integrated b6 at 5 A	10^{-4} × b2 at 30 mm	0.36
Integrated b10 at 5 A	10^{-4} × b2 at 30 mm	-0.04
Saturation at 50 A (integrated)	%	<5

Table 4.2.4 *Parameters of the cold superconducting quadrupole magnet.*

Dipole magnet		Inner	Outer
Winding type		cos-Θ	cos-Θ
Inner diameter	[mm]	83.6	88.5
Outer diameter	[mm]	85.66	90.56
Nominal current	[A]	50	50
Nominal field	[T]	0.04	0.04
Magnetic length	[mm]	197.5	197.5
Number of turns		33	34
Wire diameter	[mm]	0.7/1.03	0.7/1.03
Copper to superconductor		1.8	1.8
RRR		100	100
Filament diameter	[micron]	20	20
Twist pitch	[mm]	25	25
Iron yoke length	[mm]	140	140
Coil length	[mm]	230	230
Self inductance	[mH]	0.62	0.73
Integrated field at 50 A	[Tm]	0.0079	0.0079
Integrated b3 at 50 A	10-4 × b1 at 30 mm	4.14	-12.66
Integrated b5 at 50 A	10^{-4} × b1 at 30 mm	119	14
Int.field, dip.&quad@50 A	[Tm]	0.0069	0.0068
Saturation at 50 A	[%]	13	14

Table 4.2.5 *Parameters of the cold superconducting dipole magnet.*

Current leads

Three pairs of current leads for a maximal current of 50 A are necessary. A design of Copper-coated bronze rods, insulated by Kapton® and embedded in stainless steel tubes is selected. Two thermal heat sinks, one at 4-8 K and one 40-80 K reduce the heat load to the 2 K level (see green parts in Figure 4.2.17). The design is based on a CERN design **[4-26]** used at LHC. The superconducting wires enter the wiring box, which is flanged to the Helium vessel of the magnet package. From here stainless steel is used. The soldered connections of the superconducting wires to the cold ends of the leads are made in the wiring box and the box is closed by welding. In a complicated path the leads are brought out through the two thermal shields, allowing a 30 mm relative movement between the cold and the warm end. The leads are connected by Copper braids to the heat sinks. They end at a flange on the accelerator module where they are connected to ceramic feedthroughs, to which the power supplies are then connected.

4.2.3 Vacuum system

The layout of the linac vacuum system of the XFEL is similar to the vacuum system of the TTF linac described in **[4-27]** and **[4-28]**.

4.2.3.1 Vacuum requirements

The requirements for the vacuum system are mainly determined by the goal of reaching high accelerating gradients in the superconducting cavities. Dust particles can act as field emitters and thus, limit the performance of the superconducting cavities. As the 2 K cold cavities are an integral part of the beam pipe they act as huge cryopumps. Therefore, the risk of contaminating the superconducting cavities with particles and condensating gas from other vacuum components during assembly and operation needs to be avoided at all costs. As a consequence, the preparation of all vacuum components includes, in addition to standard UHV procedures, cleaning in a clean-room of at least class 100 to remove particles and the installation of components into the machine under local clean-rooms.

The interaction between beam and residual gas is, however, uncritical and synchrotron radiation is negligible.

4.2.3.2 Cold vacuum system

The superconducting cavities, fabricated from pure Niobium, are surrounded by a Titanium tank filled with superfluid Helium. Eight cavities, a superconducting quadrupole and a beam position monitor are grouped into 12 m long strings, which are assembled in a class 10 clean-room shown in Figure 4.2.16. The cavities are connected via Copper coated bellows without RF-shields. The sealing system has been specially developed and consist of rigid Niobium-Titanium flanges (Nb/Ti55) EB welded to the Niobium cavities and massive aluminium rings as gaskets **[4-29]**. After assembly, the complete string is evacuated, closed off by all-metal manual valves at both ends and inserted into the module tank.

As shown in Figure 4.2.18 the beam pipe interconnection between the accelerator modules consists of a 300 mm long section that incorporates a HOM-Absorber, a bellows and a vacuum pumping port. Every 12 modules, in the area of the module string connection boxes, there will be a connection for continuous pumping of the beam vacuum by sputter ion pumps and all-metal automatic beam valves.

The RF power input coupler attached to each cavity has two ceramic windows, one at a temperature of 70 K and one at room temperature. This design enables complete closure of the cavity in the clean-room by mounting the coupler up to the first window, thus preventing any contamination during further assembly of the module. Additionally, gas and dust are prevented from entering the cavities in case a crack in one of the ceramic windows should occur during operation. The warm coupler parts have a common vacuum for eight couplers of each module which is pumped by a sputter ion pump and a Titanium sublimation pump.

The accelerator module vessels serve as an isolation vacuum once the cavities are cooled down to 2 K. The layout is similar to the HERA design **[4-30]**. The string connection boxes are equipped with a vacuum barrier, which separates the insulating vacuum of the module strings, thus separating vacuum sections of 144 m length.

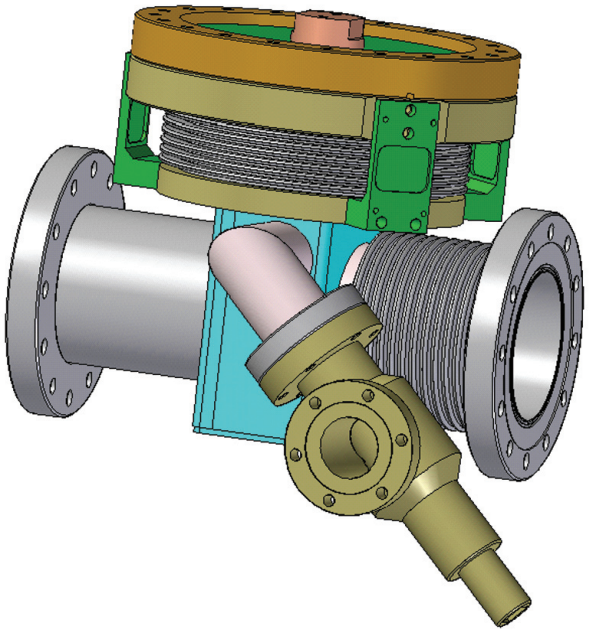

Figure 4.2.18 *Module interconnection including the HOM-absorber.*

4.2.4 High power RF system

4.2.4.1 Introduction

The XFEL RF system consists of 31 RF stations, 29 for the main linac and two for the injector, and another two if the second injector is added. Each station can provide RF power up to 10 MW peak and 150 kW average at a frequency of 1.3 GHz and distributes the power to a number of cavities in the XFEL main linac, injector and RF gun.

Each RF station comprises a klystron, an HV modulator, which transforms the AC line power to pulsed high voltage power, high voltage pulse cables, a pulse transformer, a waveguide distribution system, a low-level RF system, which controls shape, amplitude and phase of the RF, several auxiliary power supplies for the klystron and the pulse transformer, preamplifier and an interlock and control system, which protects the station and the linac.

Most of the components of the RF stations will be installed in the accelerator tunnel with a separation of 50 m. The exceptions are the modulators which will be installed above ground in a dedicated modulator hall near to one of the linac access shafts. High voltage pulse cables and additional cables for the interlock system connect the components of each station in and outside the tunnel.

The operation parameters, nominal at a linac energy of 20 GeV are listed in Table 4.2.6. Not all optimal values can be achieved at the same time.

At 20 GeV, the linac for the XFEL operates at a gradient of 23.6 MV/m with a repetition rate of 10 Hz. Since the particle beam current is 5 mA, up to 122 kW are required per cavity. The maximum beam pulse duration is 600 µs and the cavity filling time 780 µs.

Thirty-two cavities (four times eight cavities per cryogenic module) will be connected to one klystron by the RF waveguide distribution system. At nominal operation parameters, 3.9 MW are required. Taking into account 6% losses in the waveguide distribution system and a regulation reserve of 15% for phase and amplitude control, the klystron must provide up to 5.2 MW.

		Nominal	Maximum
Number of sc cavities in main linac		928	
Peak power per cavity	[kW]	122	230
Gradient	[MV/m]	23.6	28.5
Power per 32 cavities	[MW]	3.9	8.3
Power per RF station	[MW]	5.2	10
Number of installed linac RF station		29	
Number of active linac RF stations		26	
Number of installed injector RF station		2	
RF pulse duration	[ms]	1.38	1.5
Repetition rate	[Hz]	10	10 (50)
Average klystron beam power	[kW]	153	250
Average RF power during operation	[kW]	71	150

Table 4.2.6 *RF system requirements.*

In order to match the operation requirements of the different users of the XFEL it is aimed to operate the accelerator and thus the RF system at a higher repetition rate up to 50 Hz by reducing either the RF pulse width or the RF output power at the same time. The limiting factor will be the maximum average klystron beam power.

4.2.4.2 RF Power Source

The RF power source for the XFEL is a 10 MW multi-beam klystron (MBK). By using several smaller electron beams in one klystron envelope instead of a single beam, space charge forces are reduced, thus, leading to higher efficiency and lower klystron cathode voltage in comparison with a single beam klystron of the same output power **[4-31, 4-32]**. The klystron requirements are given in Table 4.2.7.

		Nominal	Min./Max
Frequency	[GHz]	1.3	1.3
RF Pulse Duration	[ms]	1.38	/1.5
Repetition Rate	[Hz]	10	/≈50 (low P_{peak})
Cathode Voltage	[kV]	95	120
Beam Current	[A]	103	140
HV Pulse Duration	[ms]	1.57	0.2/1.7
Microperveance		3.5	3.3/3.7
RF Peak Power	[MW]	5.2	10

Table 4.2.7 *Klystron parameters.*

Three manufacturers have developed MBKs which meet or almost meet these requirements. Figure 4.2.19 shows the multibeam klystrons TH1801 produced by THALES Electron Devices, VKL 8301 by CPI, and E3736 by Toshiba Electron Devices.

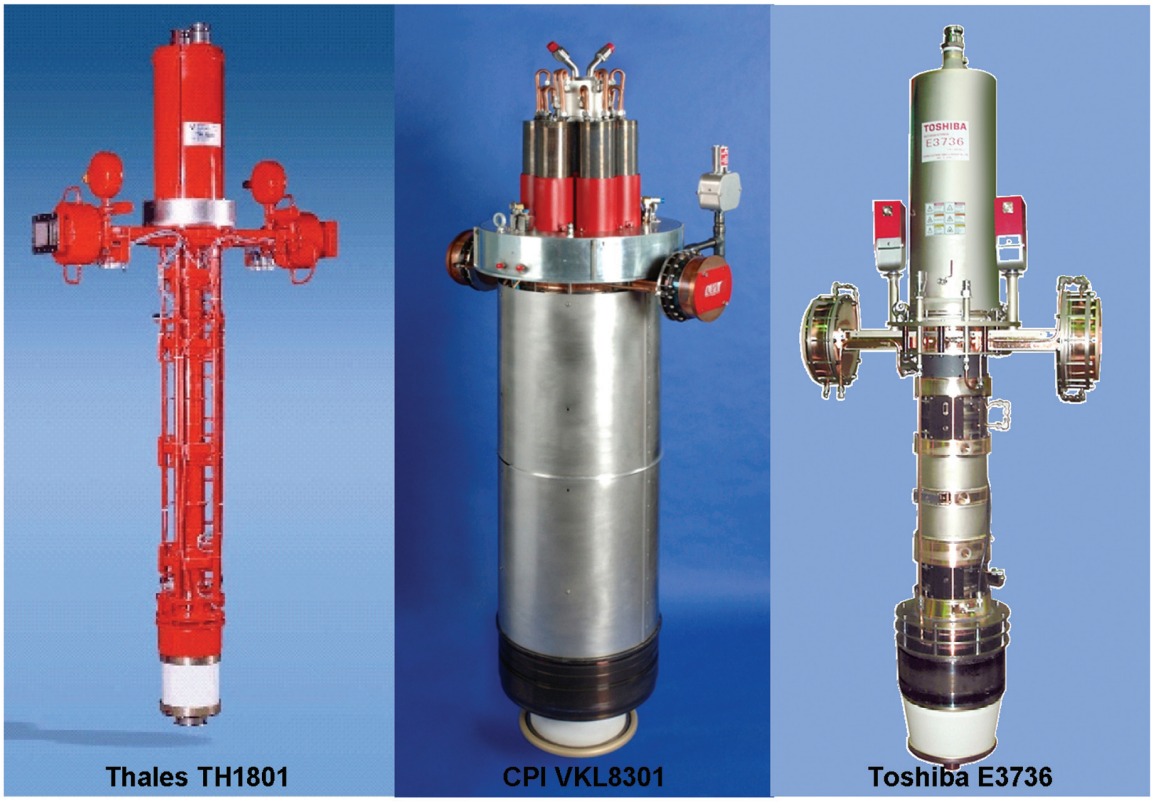

Figure 4.2.19 *Thales TH1801, CPI VKL8301, and Toshiba E3736 MBK.*

Two output waveguides are always required to handle the RF power of 2 times 5 MW in the output windows. The total height of each klystron is about 2.5 m. In order to allow horizontal installation in the XFEL tunnel, the klystron must be delivered and installed together with the solenoids on a girder.

Multi beam klystrons have been tested and operated at the TTF at DESY. They achieved an output power of 10 MW with an efficiency of 65%. More detailed information about the individual klystrons can be found in **[4-33 – 4-38]**.

4.2.4.3 HV pulse power source (modulator, pulse cable and transformer)

The HV pulse power source consists of a HV pulse modulator, a 1:12 pulse transformer and HV pulse cables up to 1.5 km length connecting modulator and pulse transformer.

It generates HV pulses of 115 kV of almost rectangular pulse shape required at the klystron cathode. The nominal pulse duration is 1.58 ms and the rise and fall time 200 µs. Already during the leading edge of the high voltage pulse, when the voltage has reached 80% of the flat top level, the klystron can start to generate RF power. Although this part of the RF pulse does not meet the requirements regarding phase and amplitude stability for particle beam acceleration in the accelerator, it can be used to fill the superconducting cavities with RF. The phase change of 320° between 80% and 100% of the klystron voltage can be compensated for by the low level RF control. The flat top ripple should not exceed ±0.5% in order to limit phase and amplitude variations of the klystron RF output during beam acceleration. The pulse-to-pulse stability must be better than ±0.5%. In case of klystron gun sparking, the energy deposited in the spark must be limited to a maximum of 20 J. The requirements are summarised in the Table 4.2.8.

		Nominal	Max.
Modulator pulse voltage/pulse transformer primary	[kV]	8	11
Modulator pulse current voltage/pulse transformer	[kA]	1.24	1.8
Pulse transformer secondary voltage/klystron gun	[kV]	95	132
Pulse transformer secondary current/klystron gun	[A]	103	150
High voltage pulse duration (70% to 70%)	[ms]	1.58	1.7
High voltage rise and fall time (0 to 99%)	[ms]	0.2	0.2
High voltage flat top (99% to 99%)	[ms]	1.38	1.5
Pulse flatness during flat top	[%]	±0.3	±0.5
Pulse-to-pulse voltage fluctuation	[%]	±0.3	±0.5
Energy deposit in klystron in case of gun spark	[J]	<20	20
Pulse repetition rate	[Hz]	10	50
Pulse transformer ratio		1 :12	

Table 4.2.8 *HV pulse power source parameters.*

The basic idea of the bouncer modulator is to use a capacitor discharge and compensate for the voltage droop by the linear part of the oscillation of a bouncer circuit. This technical solution is well established and offers high reliability compared to alternative layouts **[4-39]**.

The circuit diagram of the bouncer modulator is sketched in Figure 4.2.20. A HV power supply keeps the 1.4 mF main capacitor C1 charged to the 10 kV level. By closing the switch S1, the capacitor C1 starts to discharge via the pulse transformer into the klystron. The 1:12 transformer converts the 10 kV voltage of the capacitor to the klystron level of

120 kV. After 1.57 ms, switch S1 opens and terminates the pulse. Since the capacitor voltage drops during the pulse, no flat top would be achieved unless a huge capacitor bank storing a large amount of energy could be used. For a droop of 1% a capacitor bank of 29 mF would be required. In order to overcome the disadvantage of a huge capacitor bank the bouncer circuit was added. A circuit consisting of a choke, a capacitor and another switch is connected to the low end of the primary winding of the pulse transformer. By triggering this switch shortly before the main pulse begins, the circuit starts to oscillate. The linear part of the 5 ms long oscillation is then used to compensate for the droop of the main capacitor C1. By this the 19% droop of the 1.4 mF capacitor can be reduced to 1%. A very detailed description of the modulator is given in **[4-40 - 4-44]**.

Within the modulator a special high voltage power supply for charging the main capacitor is required. It has to charge the capacitor to an accurate voltage in order to obtain the same voltage at the klystron from pulse to pulse, and it has to suppress the repetition frequency (up to 50 Hz) load of the mains in order to avoid disturbances of the mains.

The input connection of each power supply is a three-phase grid and the output voltage is 13.5 kV. In order to ensure a high reliability the power supplies will be built in modules of switch mode buck converters or alternatively of series resonant converters.

The power supply regulation is a digital self-learning regulation of the input power, made possible by the high regulation dynamic of the converter supply. In addition, the voltage at the capacitor bank at the firing time of the pulse will be regulated to within 0.1% accuracy. Further information about the power supplies can be found in **[4-45]**.

Several modulators of the bouncer type have been built and are in use at the TTF. The first modulators were built and assembled by Fermilab, USA, and then shipped to DESY. The others were assembled at DESY from units manufactured by industrial companies.

The first modulators made by Fermilab use GTOs and IGBTs as main switches in the pulse generating unit, whereas the newer version of the pulse generating unit built by industry use IGCTs instead. The size of a modulator is 5 m (length) x 2 m (width) x 2.2 m (height).

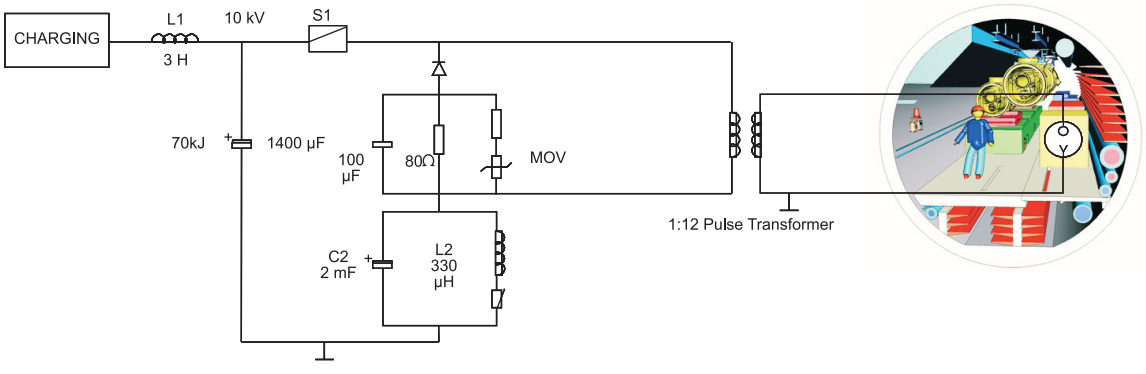

Figure 4.2.20 *Circuit diagram of the modulator (schematic).*

A 1:12 pulse transformer transforms the 9.6 kV pulses of the pulse generating unit to 115 kV required by the klystron. The transformers leakage inductance determines the rise time of the HV pulse. The first transformers had a leakage inductance of more than 300 µH whereas the newer ones have less than 200 µH. This meets the specification of rise time of less than 200 µs. The size of the transformer is 3.2 m (length) x 1.2 m (width) x 1.4 m (height), its weight is 6.5 t.

The pulse forming units of the modulators will be installed in the modulator halls at the surface, whereas the pulse transformers will be installed inside the tunnel. Thus, pulse cables with a length of up to 1.7 km must be used for the connection. In order to limit the ohmic power loss to 2%, on average, a current lead of 300 mm^2 is required. The wave impedance of the cable must match the impedance of the klystron transformed to the transformers primary side to avoid distortion of the pulse shape. In addition, the skin effect must be minimised. Therefore, four cables in parallel, each of 75 mm^2 cross section, 25Ω impedance, and an outer diameter of 30 mm, will be used. The cables are the triaxial type to minimise electromagnetic interference. The inner lead is at high potential (12 kV), the middle cylindrical lead at the potential of the bouncer circuit (±2 kV) and the outer cylindrical lead at ground potential. As insulation material VPE will be used. Additional line matching to the pulse transformer will be done via a RC network. Simulation results and further information on the cable can be found in **[4-46]**.

In case of klystron gun sparking, the modulator's main switch must be opened quickly and must be reliable to limit the energy deposited in the klystron spark to less than 20 J. The energy stored in the transformer leakage inductance and in the power transmission cable will be dissipated in two passive networks, one at the cable end near to the main switch consisting of a reverse diode and a resistor and a second one made up by an 80 Ω resistor across the transformer primary and by a 100 µF capacitor which limits the peak inverse voltage at the primary to 800 V when the main switch is opened.

4.2.4.4 Interlock and control system, preamplifier and auxiliary power supplies

Although the gain of the klystron is 48 dB and the required drive power is less than 200 W at nominal operation conditions, more power is required if the klystron is operated at lower voltage, e.g. if it is operated at a higher repetition rate than nominal but at the same average power. Taking this into account, a preamplifier with a 1 dB compression point at 650 W is needed. Even at this power level, solid state amplifiers can be used. They will be installed near to the klystrons inside the accelerator tunnel in racks housing the auxiliary power supplies and the interlock system.

Several additional auxiliary power supplies are required for the operation of the klystron and the modulator, e.g. for the klystron focusing solenoid, the klystron filament, the klystron vacuum pump and the pulse transformer core bias. Standard off-the-shelf auxiliary power supplies will be installed together in a rack near to the klystron and the pulse transformer.

The interlock system protects the accelerator and the RF stations in case of malfunction and supports the localisation of faults. Besides the modulator interlock and control system which is an integral part of the modulator, an additional interlock and control system for the RF system's components in the tunnel is required.

It will be based on programmable logic devices which have the advantage that the interlock logic can be modified easily if required. Today, electronic boards based on these devices are fast enough to react within µs. Therefore, no additional hard-wired systems for fast interlock are necessary. Besides system protection and providing start-up and shut-down procedures for the RF stations, the control and interlock system will offer diagnostics functions for the RF systems. It will allow measurement and diagnosis of actual parameters as well as adjustment of set points within certain limits for each RF station and its subsystems; and flexible reaction to different fault conditions. Communication with the accelerator's main control can be accomplished by standardised protocols.

Since each RF station consists of two parts, one in the tunnel and one in the access hall, there will be two interlock units connected to each other by glass fibre cables. Interlock conditions are summarised into categories, each starting a certain action in the other unit, thus, only a limited number of fibres is required. More detailed information on the interlock can be found in **[4-47 - 4-49]**.

The racks housing the preamplifier, auxiliary power supplies and interlock will be shielded by lead, thus protecting the electronic components in these devices from radiation.

Taking into account a maximum input power to the klystron of 250 kW and assuming a combined maximum efficiency of the system of modulator, pulse cable and pulse transformer of 75%, the AC input power is 333 kW. The other tunnel RF components require 17 kW of AC line power. So the total is 350 kW of maximum AC line power per active RF station.

4.2.4.5 RF waveguide distribution system

A linear distribution system is used to branch off equal amounts of power to the individual cavities. Thirty-two cavities (four accelerator modules) are connected to the two output waveguides of a 10 MW multibeam klystron. Directional couplers are foreseen to couple out the required amount of power. During cavity filling, a large amount of RF power is reflected back from the cavity. This also applies after the end of the beam pulse as well as in cases when the linac is operated with low beam current. In order to protect the klystrons against reflected power, a circulator is placed in front of each cavity. Motorised stub tuners are installed between the cavity and the circulator to adjust the cavities' phase and Q_{load}. A WR650 waveguide has been chosen for the RF power distributing system. Additional information on the waveguide distribution system can be found in **[4-50, 4-51]**.

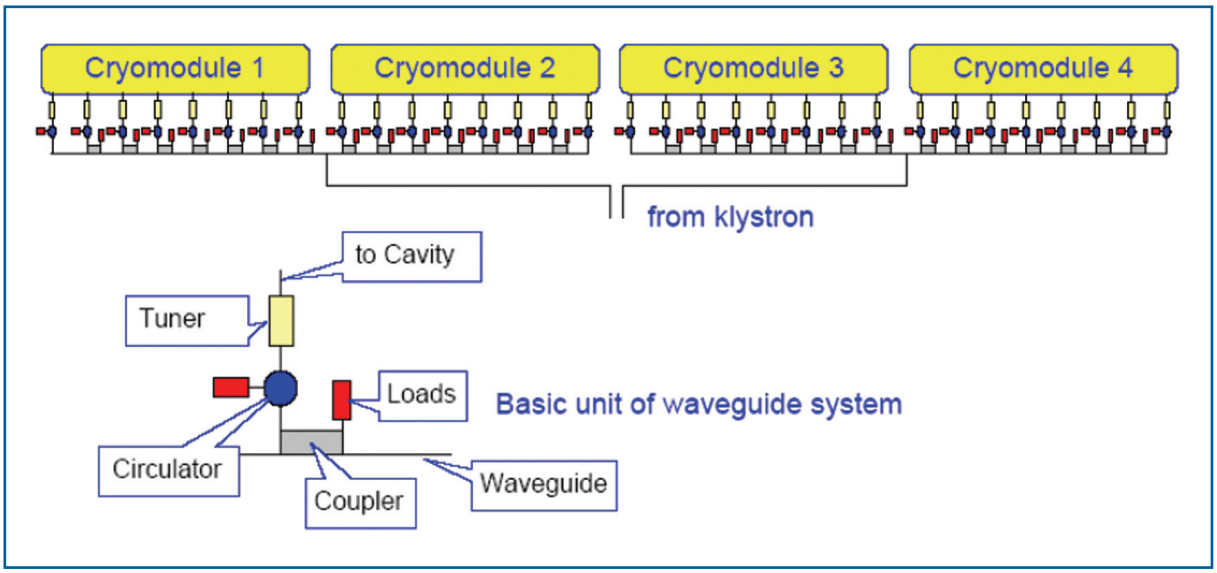

Figure 4.2.21 *RF waveguide distribution of one RF station.*

4.2.5 Low level radio frequency control

The requirements for RF control systems for the European XFEL are not only defined in terms of the stability of RF amplitude and phase but also with respect to the operability, availability and maintainability of the RF system. The field control of the vector-sum of many cavities driven by one klystron in pulsed mode at high gradients is a challenging task since Lorentz-force detuning, mechanical vibrations (microphonics), and beam-induced field errors must be suppressed by several orders of magnitude. This is accomplished by a combination of local and global feedback and feed-forward control.

Sensors monitor the individual cavity probe signals, together with forward and reflected wave as well as the beam properties. The electron beam energy, beam current and phase, with respect to the external RF master oscillator, are additional input parameters for the low level radio frequency (LLRF) control. Actuators control the incident wave of the klystron and the individual cavities' resonance frequency.

A high degree of automation eases the operability of the large LLRF system. High availability requires robust algorithms, redundancy, and extremely reliable hardware. Sophisticated on-line diagnostics for the LLRF subsystems support maintenance and minimise downtime.

LLRF systems are required for the RF gun, the injector RF systems including the third harmonic cavity, and the accelerator modules in the main linac. The largest RF system installation will be in the linac, with 928 cavities in 116 accelerator modules (where 32 cavities are driven by one 10 MW klystron). The technology for controlling the vector-sum of many cavities driven by one klystron has been demonstrated successfully at the TTF and is presently in operation at Free-electron LASer in Hamburg (FLASH) at DESY. It is a fully digital system providing the capability for feedback and feed-forward, exception handling and extensive build-in diagnostics. However, the full potential of such systems in terms of operability in large scale systems and the reliability required for the XFEL remains to be demonstrated.

4.2.5.1 Requirements for RF control

The requirements for the RF control system are usually defined in terms of phase and amplitude stability of the accelerating field during the 600 µs long flat-top portion of the RF pulse. In addition, operational demands impose further needs on the design of the RF control system.

Amplitude and phase stability

The requirements of the RF control system are derived from the desired beam parameters such as bunch-to-bunch and pulse-to-pulse energy spread, the bunch compression in the injector, and the arrival-time of the beam at the undulators. The beam parameters can be translated into the requirements for phase and amplitude of the accelerating field of individual cavities or the vector-sum of several cavities driven by one klystron. The RF systems in the injector of the XFEL require tight field control in the order of 0.01% for the amplitude and 0.01° for the phase. Additional requirements are imposed on the accuracy of the calibration of the vector- sum which must be in the order of 1% for amplitude and 0.5° for phase in presence of ±10° microphonics (see also Section 4.2.5.2).

Operational requirements

Besides field stabilisation, the RF control system must provide diagnostics for the calibration of gradient and beam phase, measurement of the loop phase, cavity detuning and control of the cavity frequency tuners. Exception handling capability will be implemented to avoid unnecessary beam loss and to allow for maximum operable gradient.

4.2.5.2 Sources of field perturbations

The LLRF system will suppress field perturbations induced by fluctuations in the resonance frequency of the cavities and fluctuations of the beam current. Changes in resonance frequency result from variations in the cavity shape induced either by mechanical vibrations (microphonics) or by the gradient dependent Lorentz-force caused by the electromagnetic accelerating field inside the cavity.

Lorentz-force

The static detuning of a resonator due to Lorentz-force is proportional to the square of the accelerating field. In the case of pulsed RF fields, a time varying cavity detuning – even during the flat-top portion of the RF pulse – can be observed. Mechanical resonances will be excited, whereas the lower the mechanical quality factor and the higher the mechanical resonance frequency (only longitudinal modes should be excited), the less likely is the enhancement of the peak cavity detuning by the Lorentz-force. Stiffening rings at the iris are used to reduce the Lorentz-force detuning constant to below 1 Hz/(MV/m)^2 and increase the mechanical resonance frequencies.

Microphonics

Mechanical vibrations caused by the accelerator environment (e.g. vacuum pumps at the cryogenics facility) are always present and may be transferred to accelerating structures through cryogenic transfer line, and beam pipe. The frequency spectrum and amplitude of excitation depend strongly on the coupling to the cavities. Measurements at the TTF show typical excitation amplitudes in the order of 5-10 Hz (rms) and frequencies ranging from 0.1 Hz up to a few hundred Hz.

Beam loading

The loaded Q is usually chosen for matched conditions, i.e. all of the RF generator power (with the exception of a small amount dissipated in the sc-cavities) is transferred to the beam. In the case of on-crest operation (the electron bunches see the maximum amplitude) the magnitude of the beam-induced voltage is half of the generator-induced voltage. While slow bunch charge fluctuations within the bandwidth of the LLRF system can be controlled, fast fluctuations in the order of a few percent of the bunch charge need not be corrected since the introduced amplitude and phase errors do not exceed the field stability requirements.

4.2.5.3 RF control concept and control system architecture

The basic idea of any RF control system is based on feedback control in which the cavity field vector is measured and compared to the desired set-point. The resulting error vector (the difference between measured field and set-point) is filtered and amplified before modulating the klystron drive and thereby, the incident wave to the cavities. Nevertheless, during pulsed operation, the perturbations from the above mentioned Lorentz-force detuning and beam loading are of a repetitive nature. Thus, the feedback can be supplemented by a feed-forward which compensates the average repetitive error. In addition, the cavity field set-point can be implemented as a table to accommodate the time-varying gradient and phase during cavity filling.

The architecture of a typical RF control system is shown in Figure 4.2.22. A power amplifier provides the RF power necessary for establishing the accelerating fields in the cavities. The cavity field is measured and compared to a set-point. The resulting error signal is amplified and filtered and drives a controller for the incident wave to the cavity. A frequency and phase stable master oscillator and RF distribution system provide the necessary RF reference signals for the cavity field measurements.

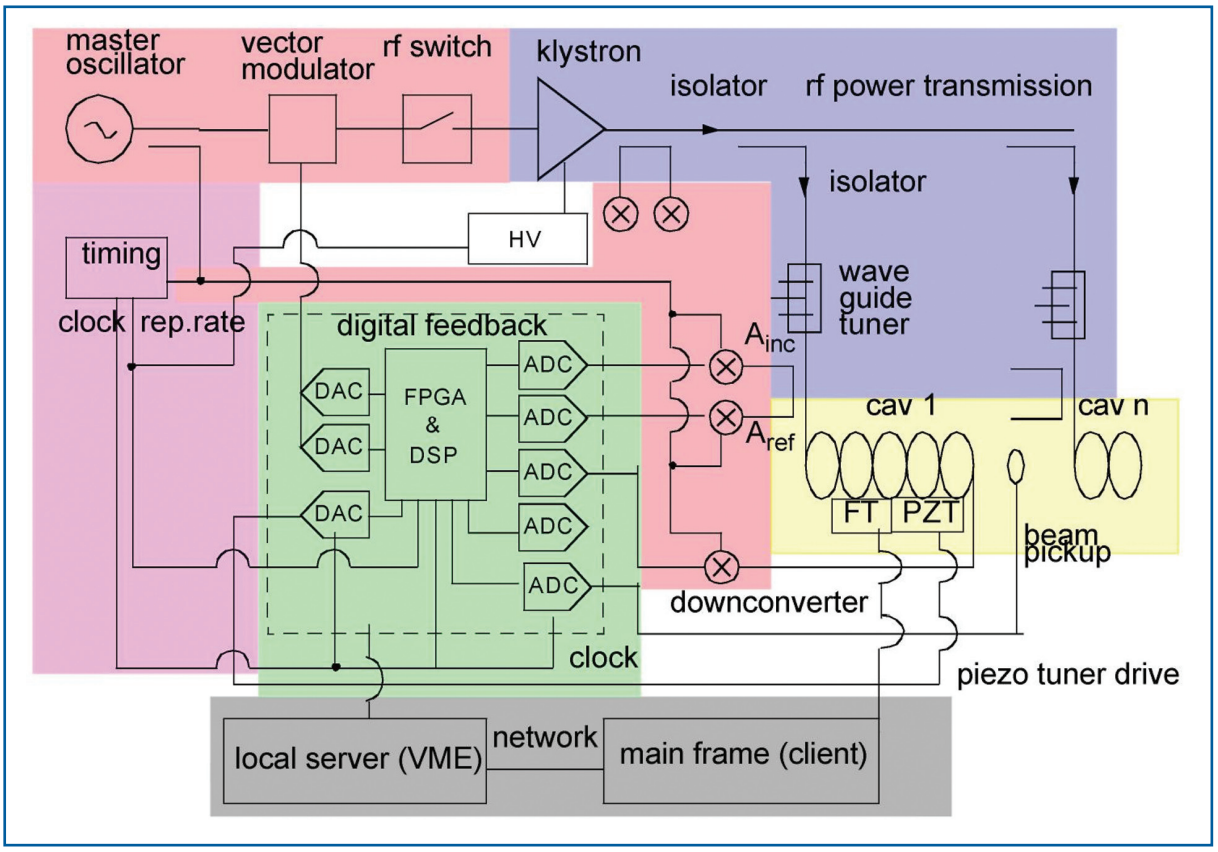

Figure 4.2.22 *Typical configuration of an RF control system using digital feedback control.*

The overall design of the RF control system provides:

- control of the cavity resonance frequency. Here the critical issue is the precise measurement of the cavity detuning which can be derived from the relationship of incident and reflected wave or in the pulsed operation mode from the slope of the phase during decay of the cavity field following the RF pulse;
- linearisation of the klystron – since operation close to klystron saturation will result in strong dependence of loop gain with klystron output power;
- remote control of waveguide tuners or phase shifters. In the case of vector-sum control, the phase of the incident wave (and loaded Q) of each cavity must be set independently to compensate for phase errors in the waveguide distribution system;
- exception handling. In case of interlock trips or abnormal operating conditions (wrong loop phase or completely detuned cavity) the control system must ensure safe procedures to protect hardware and avoid unnecessary beam loss.

4.2.5.4 Digital RF control

The use of a digital RF feedback and feed-forward system supports automated operation with minimal operator intervention. A number of algorithms can be used to guarantee best field stability (i.e. lowest possible rms amplitude and phase errors), to allow for fast trip recovery, and to support exception handling. Beam-based feed-forward will further enhance

the field stability. Also important is the automated control of the resonance frequency of the cavities with slow motor-controlled tuners and fast piezo actuator or magneto-strictive element **[4-52]** based tuners for Lorentz-force compensation in pulsed RF systems.

The key elements to be used are modern analogue to digital converters (ADCs), digital to analog converters (DACs), as well as for signal processing, powerful Field Programmable Gate-Array (FPGAs) and digital signal processing (DSPs). Low latencies can be realised – from ADC's clock to DAC output ranging from a few 100 ns to several µs depending on the chosen processor and the complexity of the algorithms. Gigabit Links are used for the high data rates between the large number of analogue I/O channels and the digital processor as well as for communication between various signal processing units **[4-53]**. Typical parameters for the ADCs and DACs are a sample rate of 65-125 MHz at 14-bit resolution (example AD6644). For the signal processing one has the choice of FPGAs with several million gates, including many fast multipliers cores and even with a Power PCs on the same chip such as the Virtex2Pro from Xilinx or the Stratix GX from Altera. More complex algorithms are implemented on slower floating point DSPs, such as the C6701 from Texas Instruments or the SHARC DSP from Analog Devices.

Present status of the LLRF development

At the vacuum ultraviolet (VUV)-FEL a DSP-based LLRF system has been commissioned and is now operational. This system does not meet all the requirements of the XFEL for achievable field stability, reliability and operability. The amplitude and phase stability achieved at the VUV-FEL are 0.03% (rms), and 0.03° (rms), respectively, which is sufficient for the main linac of the XFEL but not for the RF system in the injector where an improvement of a factor of 2 to 3 is needed. Areas for improvement are the down-converters for field detection **[4-54, 4-55]** (better linearity and lower noise levels), the number of analogue I/O channels, the latency in the controls loop, and the real-time computing power. The system must also be immune to Single Event Upsets (SEU), i.e. a spontaneous bit flip caused by, for example, radiation. Since a major effort will go into the software development it is important to have a prototype of the hardware to support this. This has been achieved with prototype of an FPGA-based digital controller **[4-56]** which has been evaluated recently during operation of the RF gun. With this platform it will be possible to implement and test new algorithms at FLASH (the VUV-FEL). The new hardware allows for higher sampling rates, thus supporting higher IF frequencies resulting in lower noise levels and lower latency. This hardware is already used at the facilities of the TESLA Technology Collaboration partners which will allow the sharing and exchange of LLRF controls software.

4.2.5.5 LLRF studies during the XFEL preparation phase

Low level RF system performance (simulations)

LLRF simulation programmes will be developed to study the expected performance of the RF control system. Feedback and feed-forward algorithms, the response to a cavity quench, or beam current variations, and non-linear gain behaviour of the klystron will be simulated in a Matlab/Simulink environment. In a rather generic way, basic blocks are defined such as cavity, controller and power source. The simulation programme will be

used to compare predicted performance with the actually measured performance and to define the control algorithm to be used in the digital feedback system **[4-57]**. Performance studies include operation at different gradients, and operation close to klystron saturation. If possible the cavity simulation will be implemented on a DSP or FPGA-based system to allow real-time simulation. This will provide a basis for testing the feedback system.

RF system reliability and tunnel installation

The overall XFEL injector and linac reliability and availability are a serious issue. As far as systems are placed inside the linac tunnel, they must be designed in a robust fashion since they are not accessible during operation. The potential for radiation damage is an added risk. Evaluation of trips or failures, what response results, what action is taken and how long it takes, all result in impact on availability. All these failure modes need to be thought through and possible mitigation considered. Smartly designed redundancy such as a simple feed-forward backing up the complex feedback scheme will be essential to guarantee the required availability. Built-in diagnostics for hardware and software will support preventive maintenance and increase reliability **[4-58]**.

Exception handling for the RF system

There will be a number of exceptions to normal operation that should be handled as rapidly and transparently as possible in order to maximise the FEL operation time. These exceptions include: cavity trips or quenches, beam current variation, klystron trips, RF out of range, etc. Some of these exceptions can be handled at the RF control level, like in the DSP, while others may need coordination from one station to another, or operation interruption through the Machine Protection System. Lists of exceptions will be developed, strategies for dealing with them worked out, and implication hardware and software specified and designed.

Waveguide tuner control

In the XFEL, up to 32 cavities (one RF station) will be driven by one klystron. Relative phase and amplitude adjustment between cavities will be provided, in part, by 3-stub tuners at each cavity just before the input power coupler. Tuners will be periodically adjusted by stepping motors based on information gathered by the LLRF system. Conceptual and detailed procedures and control algorithms will be worked out and implemented in hardware and software, with interfaces to LLRF.

LLRF Finite State Machine server and applications

The goal for the FEL control system is the fully automated operation of the large number of sub-systems. One of the most complex sub-systems is the RF control system. The automation will be implemented in the framework of a Finite State Machine (FSM) which is a well established industrial standard. The FSM concept has been integrated into the control system DOOCS used at the TTF/VUV-FEL to simplify the automation of the accelerator operation. For the XFEL the first step will be the definition of the super-states, sub-states, flows, entry-, during-, and exit-procedures, entry-conditions, timer and event triggered procedures, etc. The next step is the description of the applications to be used by the FSM. Then the full functionality will be implemented as an FSM server in DOOCS,

and the required application programmes will be developed. The basic functions of automation include, for example:

- RF system start-up;
- the setting of the RF system parameters needed for beam operation;
- beam loading compensation;
- cavity detuning;
- adjustment of loaded Q and incident wave;
- exception handling;
- performance optimisation.

LLRF servers

The LLRF that drives each klystron will be controlled by a FPGA and DSP-based real-time feedback system. The digital signal processing electronics in turn must get their parameters from the LLRF server **[4-59]**. The server software handles: generation of set point and feed-forward tables from basic settings, rotation matrices for I and Q of each cavity, loop phase constant, start-up configuration files, feedback parameters, and exception handler control parameters. Server software and interface to the DSPs and control system need detailed specification and code generation. Other servers relate to local reference oscillators (LO)-generation, RF system calibration, waveguide tuner control, cavity resonance frequency control, the ADC server for measurement of probe, forward and reflected power, and hardware and software diagnostics.

Local oscillator signal generation

Each RF station will have LO for both basic RF 1.3 GHz frequency generation and for driving the system that supplies down-conversion of the RF monitor signals and sampling gates that produce the I and Q components of the monitored signals. Prototypes have been built but more accurate systems are possible. Investigation and development of better systems for phase-noise and phase drifts are needed.

Radiation effects on electronics installed in the XFEL linac tunnel

Due to dark currents (from possible field emission in the accelerator cavities) there will be a background radiation (gammas and neutrons) in the XFEL linac tunnel. It is expected that dark current of several microamperes can reach an energy of about 100 MeV before being dumped in the beamline. Similar radiation background can be measured at the positron converter at the Linac II/DESY. This offers the possibility of studying single event effects and total ionising dose effects in electronics similar to the one installed in the XFEL linac tunnel **[4-60, 4-61]**. The main objective is to perform a test which allows learning what type of problems might occur in the XFEL linac tunnel and what shielding and hardware and software design measures can be taken to guarantee reliable performance of the electronics.

Piezo tuner control

As mentioned already, adaptive feed-forward to control Lorentz-force detuning can be used. Detailed studies at the TTF/FLASH will evaluate the potential for control of the Lorentz-force detuning as well as the control of microphonics.

Klystron linearisation

Increasing the electron beam energy to more than 20 GeV requires a maximum efficiency of the XFEL linac. The 10 MW klystrons must be operated close to saturation. Due to the non-linearity of the klystron this will lead to a strong dependency of the feedback gain on the klystron output power. A possible solution is the linearisation of the klystron with digital methods such as look-up tables or polynomials. It is desirable to develop an on-line mapping method to correct for klystron ageing. The mapping must be time variable due to the time-varying high voltage during the pulse. The linearisation should work over a large range of high voltage settings.

Gradient and phase calibration based on beam-induced transients

In order to optimise the LLRF system the transient of a single bunch (1 nC) should be measured **[4-62, 4-63]** with a precision of a few percent. This means that the beam phase can be determined within a few degrees, and the gradient calibration within a few percent. Accuracy can be increased by averaging over many bunches. Lock-in techniques will be studied for further signal noise improvement.

4.3 Injector

4.3.1 General layout

The injector consists of an RF gun, a standard accelerating module and a diagnostic section. The whole setup is located in the injector tunnel, which is separated from the main linac tunnel by the access shaft XSE. The shielding and personal protection system of the injector tunnel and the integration of a beam dump at the end of the injector, allow the operation of the injector independently of the main linac. The injector building comprises two injector tunnels of which, only one will be equipped with an injector in the beginning. The second tunnel can be used to install a second, redundant injector, or may be used to install a different injector type if, for example, special machine parameters are requested for other operation modes at a later time. Shielding as well as cryogenic supply allow for installation and maintenance work in one injector tunnel while the other injector and the main linac are in operation.

The injector building contains (besides the two injector tunnels) rooms for the installation of the photocathode drive laser, electronic equipment, klystrons, etc. Components are as far as possible installed outside the injector tunnel and are hence, accessible during operation.

From the beam dynamics point of view, the XFEL injector follows in its design the VUV-FEL injector design **[4-64]**. The electron bunch is emitted by a Cs_2Te cathode illuminated by a UV laser pulse in a high accelerating field (60 MV/m on the cathode, corresponding

to 30 MV/m average gradient in the gun cavity) and accelerated up to 6.6 MeV in the normal conducting 1.3 GHz RF gun cavity. The gun cavity is about 0.25 m long (one and a half cells) and is powered by a standard 10 MW klystron. A solenoid, centred 0.4 m downstream of the cathode, focuses the beam into the first accelerator module which is located after a 3 m long drift. Even without a bucking coil the solenoid field on the cathode is negligible. The accelerator module increases the energy to about 120 MeV. The accelerating section is followed by a diagnostics section, consisting of a four-screen transverse emittance measurement section and a dispersive section before the beam dump for energy and energy spread measurements. More details of the injector design can be found in **[4-65]** and **[4-66]**.

Table 4.3.1 summarises the main parameters of the XFEL injector:

Charge	1	nC
Laser pulse length (total)	20	ps
Laser pulse rise/fall time	2	ps
Laser spot radius	1.1	mm
Peak electric field on the cathode	60	MV/m
Solenoid centre position (with respect to cathode)	0.41	m
Solenoid peak field	0.19	T
Accelerator module:		
Gradient cavities 1 - 4	7.5	MV/m
Gradient cavities 5 - 8	25	MV/m

Table 4.3.1 *Main XFEL injector parameters.*

Figure 4.3.1 shows the expected evolution of the transverse emittance along the injector with the parameters of Table 4.3.1. The initial kinetic energy of the electrons at the cathode is assumed to be 0.55 eV in this simulation. The final projected emittance is 0.88 mrad mm.

Measurements at the Photo-Injector Test Stand in Zeuthen (PITZ) gun test facility **[4-67, 4-68]** indicate that the kinetic energy of the photoemitted electrons is larger than previously assumed leading to a larger initial emittance. This can be largely compensated for by reducing the initial spot size and re-optimising the focusing parameters into the accelerating module. Figure 4.3.2 shows the final projected emittance of the electron beam after re-optimisation for different initial kinetic energies. The final emittance stays below the design value of 1 mrad mm for kinetic energies below 1 eV.

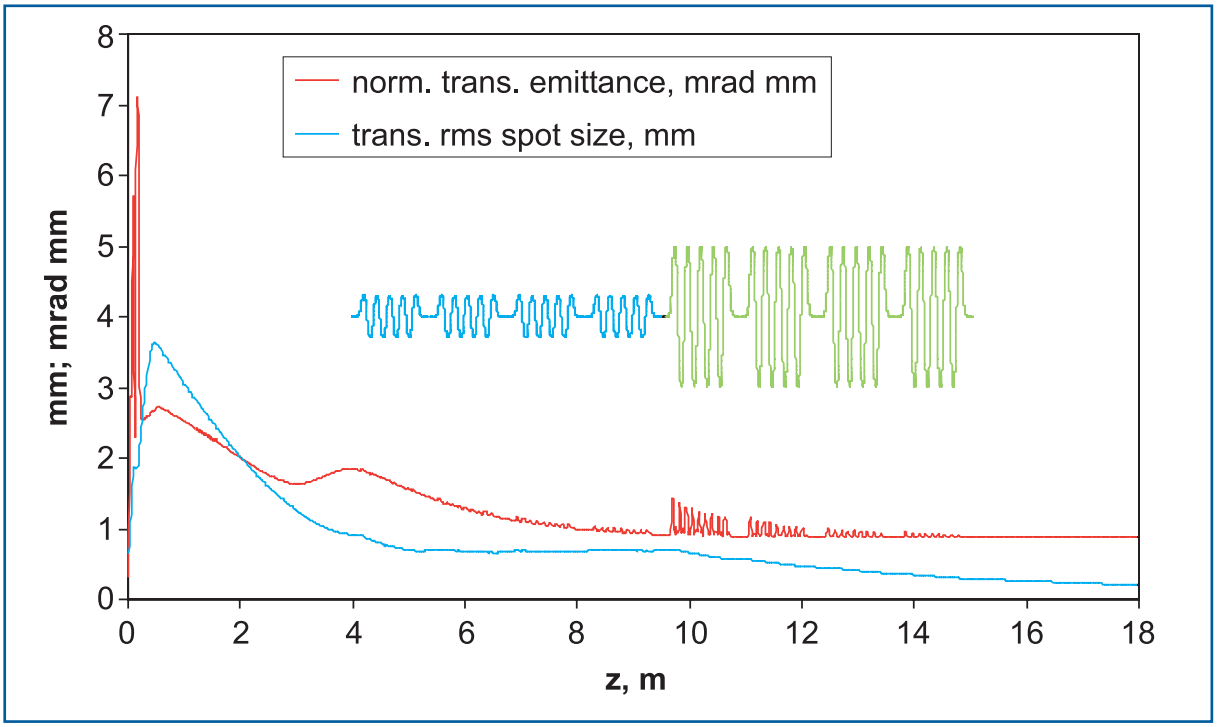

Figure 4.3.1 *Evolution of the spot size and the normalised transverse emittance in the XFEL injector. The position and strength of the accelerating field of the superconducting module is also indicated.*

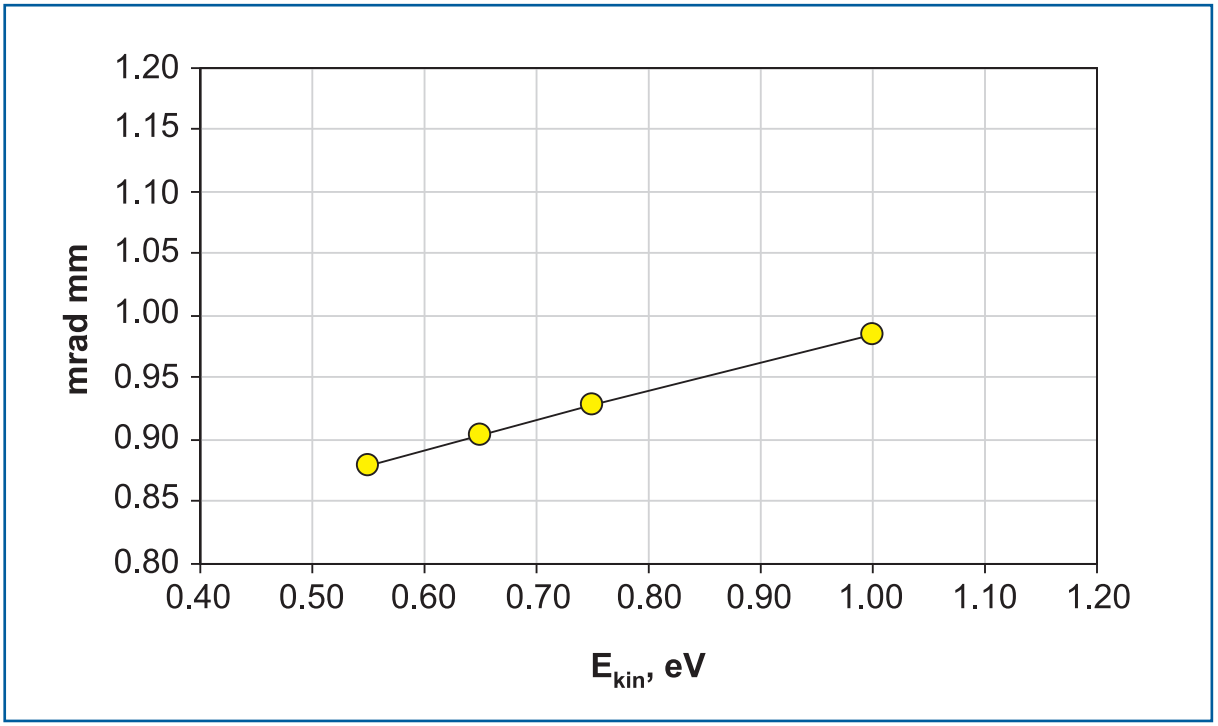

Figure 4.3.2 *Final normalised transverse emittance as function of the initial kinetic energy of the photo emitted electrons. A significant increase of the emittance can be avoided by reducing the initial spot size and re-optimising the matching conditions into the accelerator module.*

4.3.2 Experimental status and future developments

Transverse core emittance measurements at the photo injector test stand PITZ and at the VUV-FEL yield values of 1.4 mrad mm and below **[4-69 - 4-71]**. The measurements at PITZ are performed directly behind the RF gun cavity at an energy of about 4.5 MeV. The photocathode laser beam is shaped transversely (uniform, circular distribution on the cathode) and longitudinally (trapezoidal, 20 ps length, 4 ps rise/fall time). At the VUV-FEL (FLASH) the optimal longitudinal laser pulse form is not available yet, but the acceleration in the first module improves the emittance compensation mechanism, so that similar emittance values are achieved. Measurements at the VUV-FEL are performed at ~125 MeV beam energy and the photocathode laser beam has a longitudinally Gaussian shape of 4.5 ps rms width. The measurement results of the beam emittance and other beam parameters obtained at PITZ and the VUV-FEL correspond with simulation results and the beam dynamics in the gun and the injector are well understood.

While the measured core emittance values already reach the design slice emittance values for the XFEL at the entrance of the undulator, the design value for the injector has a tighter specification to operate with a sufficient safety margin. To realise the required improvement of the performance, the gradient in the gun cavity has to be increased from the present 42-45 MV/m to 60 MV/m. Additionally, the rise/fall time of the trapezoidal laser pulse should be decreased to 2 ps or below. The development efforts at the test stand PITZ will, hence, focus on these topics in the upcoming years. Other developments concentrate on further improvements in the high duty cycle operation, general stability issues, reduction of dark current and further investigations of the thermal emittance of photocathodes.

4.3.3 Photocathode laser

The photocathode laser is based on the laser developed for TTF **[4-72]** and its upgrade for the VUV-FEL **[4-73]**. The laser has been in operation since 1998 providing beam for the TTF linac. Further development of the laser system is continued at PITZ, where new ideas, especially the generation of flat-top laser pulses are studied **[4-74]**. In the present configuration, the laser is based on a diode pumped pulse train oscillator (PTO). The oscillator is synchronised with the master RF. The pulse train generated by the PTO is longer and has a shorter intra-pulse distance than the required electron bunch train structure (27 MHz at the VUV-FEL). A Pockels cell-based pulse picker picks out the required pulse train which is then amplified by a chain of diode-pumped amplifiers. The pulse picker not only gives flexibility in choosing the pulse train structure, it also serves as a fast switch-off mechanism for the MPS. Since the preferred photocathode material Cs_2Te requires radiation in the UV, the infrared light of the laser is quadrupled in frequency by non-linear crystals to 262 nm. The good quantum efficiency of the photocathode (in the order of a few percent) translates into a required laser pulse energy of a few µJ per pulse for a charge of 1 nC. The formation of synchronised picosecond pulses in the PTO is accomplished by an active mode-locking scheme. The key part is an electro-optic phase modulator driven by the 1.3 GHz frequency of the accelerator. It provides a phase stability of the laser pulse in respect to the master RF of less than 0.1° or 200 fs (rms). This has been confirmed by measurements of the electron beam arrival-time after acceleration at the VUV-FEL

[4-75]. The shot-to-shot stability in energy of the laser pulses and thus, the electron bunch charge, is 2% (rms) for single pulses and 1% (rms) averaged over a pulse train **[4-64]**. The generation of flat-top laser pulses both in the transverse and longitudinal plane is being successfully tested at PITZ **[4-74]**. Operation of such a system is foreseen at the VUV (FLASH-FEL) in the near future.

4.4 The bunch compressor system and start-to-end simulations

4.4.1 Introduction and layout

The layout of the bunch compression system **[4-76]** is sketched in Figure 4.4.1. The initially 2 mm (rms) long bunch is compressed in two magnetic chicanes by factors of 20 and five, respectively, to achieve a peak current of 5 kA. The optics of the beamline between the chicanes is optimised to reduce projected emittance growth **[4-77]**. Details about the chicanes proper can be found in **[4-78]**.

The energy chirp injected by running off-crest in the RF upstream of the first chicane is about 10 MeV, roughly compensating the energy contribution by the longitudinal wake fields of all main linac RF structures.

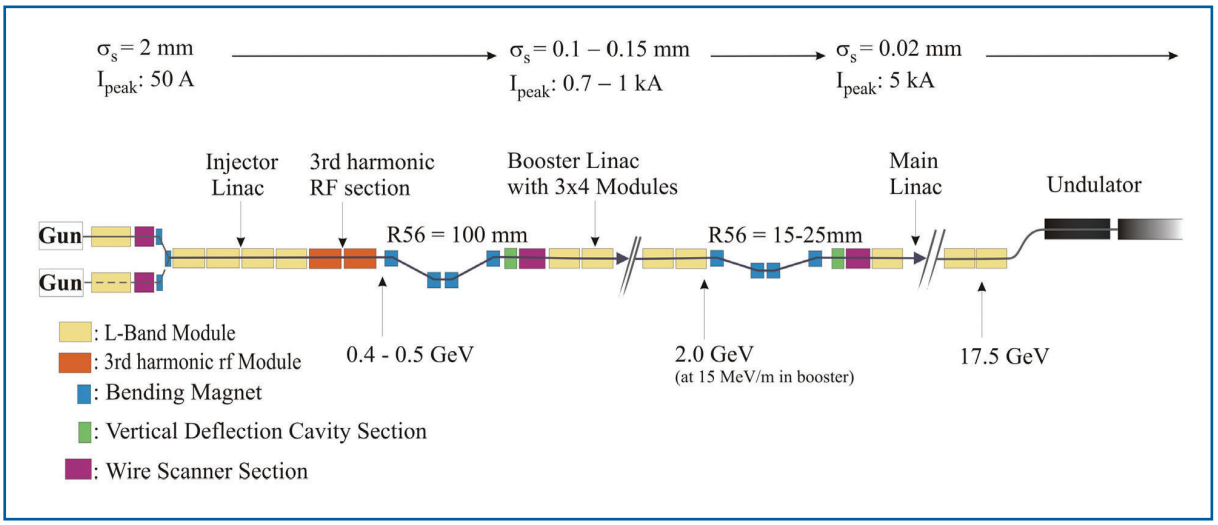

Figure 4.4.1 *Sketch of the XFEL bunch compression system.*

A third harmonic RF system is used to optimise the final longitudinal charge distribution **[4-79, 4-80]**. The minimum amplitude is about 90 MeV, corresponding to 16 third-harmonic cavities being operated in one module at 17 MV/m. With a second module, operation at RF working points with much less sensitivity to RF phase jitter becomes possible **[4-81]**.

Downstream of both chicanes, slice emittance and other parameters which vary along the longitudinal position in the bunch can be measured with vertically deflecting RF systems and wire scanner sections allow control of projected emittance and optics. Basic parameters for the bunch compression system are summarised in Table 4.4.1.

Beam energy at first chicane	0.4 … 0.5	GeV
Beam energy at second chicane	2	GeV
Longitudinal dispersion (R56) of first chicane	~ -100	mm
R56 of second chicane	-15 … -25	mm
R56 of collimation section	0.84	mm
Nominal compression factor of first chicane	20	
Nominal compression factor of second chicane	5	

Table 4.4.1 *Parameters for the bunch compression system.*

In the next chapter, results of simulation calculations including coherent synchrotron radiation (CSR) effects, space charge forces and the impact of wake fields are presented. They show the potential of the XFEL for further improvement or, respectively, its safety margin for operation at design values. Operation beyond the design parameters is discussed in two directions: achieving the uppermost number of photons in a single pulse on one hand and reaching the necessary peak current for lasing with a pulse as short as possible with possibly improved transverse emittance on the other.

4.4.2 Space charge and coherent synchrotron radiation effects

4.4.2.1 Transverse space charge effects

In low-emittance, high-current electron beams, space charge forces can cause growth of slice emittance and mismatch of slice Twiss parameters, with respect to the design (zero current) optics. Slice emittance growth directly degrades the performance of the SASE-FEL. The generated mismatch complicates accelerator operations because of projected emittance increase and the dependence of transverse dynamics on beam current. Extensive numerical studies were done using the TrackFMN code **[4-82]** and cross-checked with other codes (ASTRA **[4-83]**, CSRtrack **[4-84]**).

With the second compression stage at 2 GeV beam energy and optimised optics in the beamline sections downstream of the compressor chicane, the slice emittance growth (at design parameters) due to transverse space charge is less than 1%. The optical mismatch downstream of the first chicane corresponds to a beating of the β-function of about 5% if the bunch charge would change by 10%, and less than 1% downstream of the second chicane.

4.4.2.2 Coherent synchrotron radiation effects

The impact of CSR fields on beam emittance in the compressor chicanes was calculated with the code CSRtrack. The left side of Figure 4.4.2 shows the normalised horizontal emittance at the end of the compression system, if the peak current is raised by increasing the bending magnet strength in the second compressor chicane. In the right plot, the bunch charge is lowered and the longitudinal dispersion (R56) of the second chicane increased to keep the 5 kA peak current at the bunch compressor exit. Operating the XFEL like this has two (potential) rewards: The FEL pulse gets shorter and, with even smaller transverse emittance, lasing at shorter wavelengths might be achievable.

For the simulation, a 1 nC beam distribution at the injector exit is scaled in charge. Down to 0.25 nC the slice emittance growth stays within 5%, sufficiently low to profit from smaller emittance at lower bunch charge. The bunch length is reduced to 5 µm.

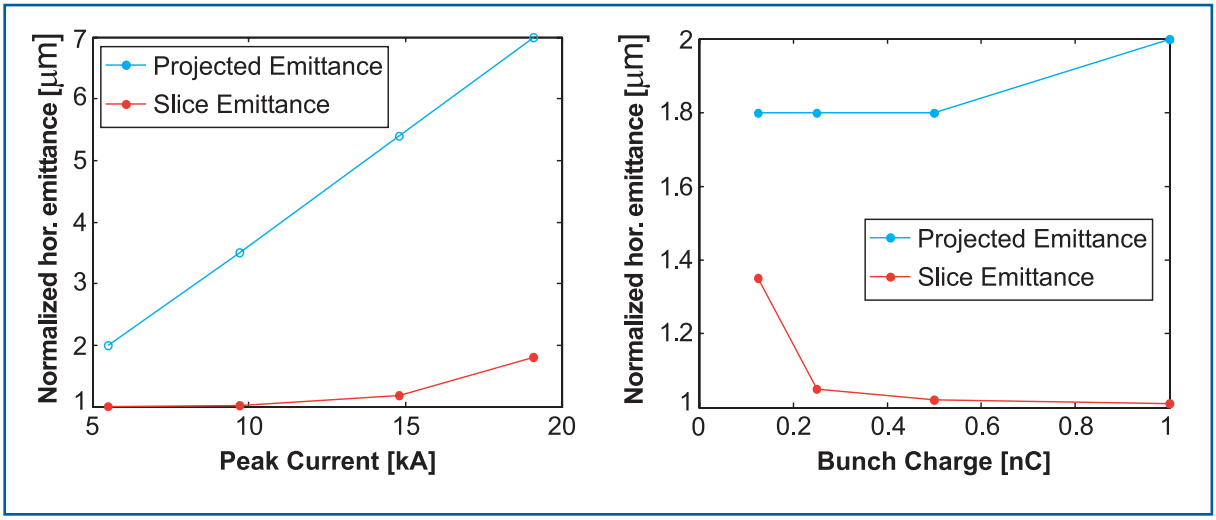

Figure 4.4.2 *Normalised horizontal emittance against different peak currents due to different settings of the second bunch compression chicane (left) and against bunch charge for fixed peak current of 5 kA (right).*

4.4.3 RF set-up and tolerances

A third harmonic RF system is used to compensate higher order effects of the dispersion and the RF voltage. A procedure to optimise the final longitudinal charge distributions is discussed in **[4-79]**. The amplitudes and phases of the fundamental and the higher harmonic RF system offer four degrees of freedom to adjust the beam energy, the chirp and the second and third derivative of the particle momentum distribution **[4-81]**. The beam energy and the chirp are fixed by the final peak current requirement. Simulations show that only a narrow range of the second derivative settings produces a reasonably symmetric beam profile without spikes.

The third derivative can be adjusted over a wide range without influencing the core of the distribution; it scales mostly with the amplitude of the third harmonic system and can be chosen to optimise RF parameter sensitivities.

Numerical results for a scan of the third derivative are presented in Figure 4.4.3. The amplitude of the fundamental harmonic RF system against the third harmonic RF amplitude is shown as well as sensitivities for the phases and amplitudes of the two RF systems. In the graphs showing sensitivities, the amount of phase or amplitude offset which causes a change of the final peak current by 10% is plotted.

The red curves are calculated for a beam energy of the first chicane of 500 MeV and a compression factor of 20 (and 5 in the second chicane), for the blue curves, the beam energy is 400 MeV and the compression factor 14 (and 7 in the second chicane), to keep space charge forces at the same level.

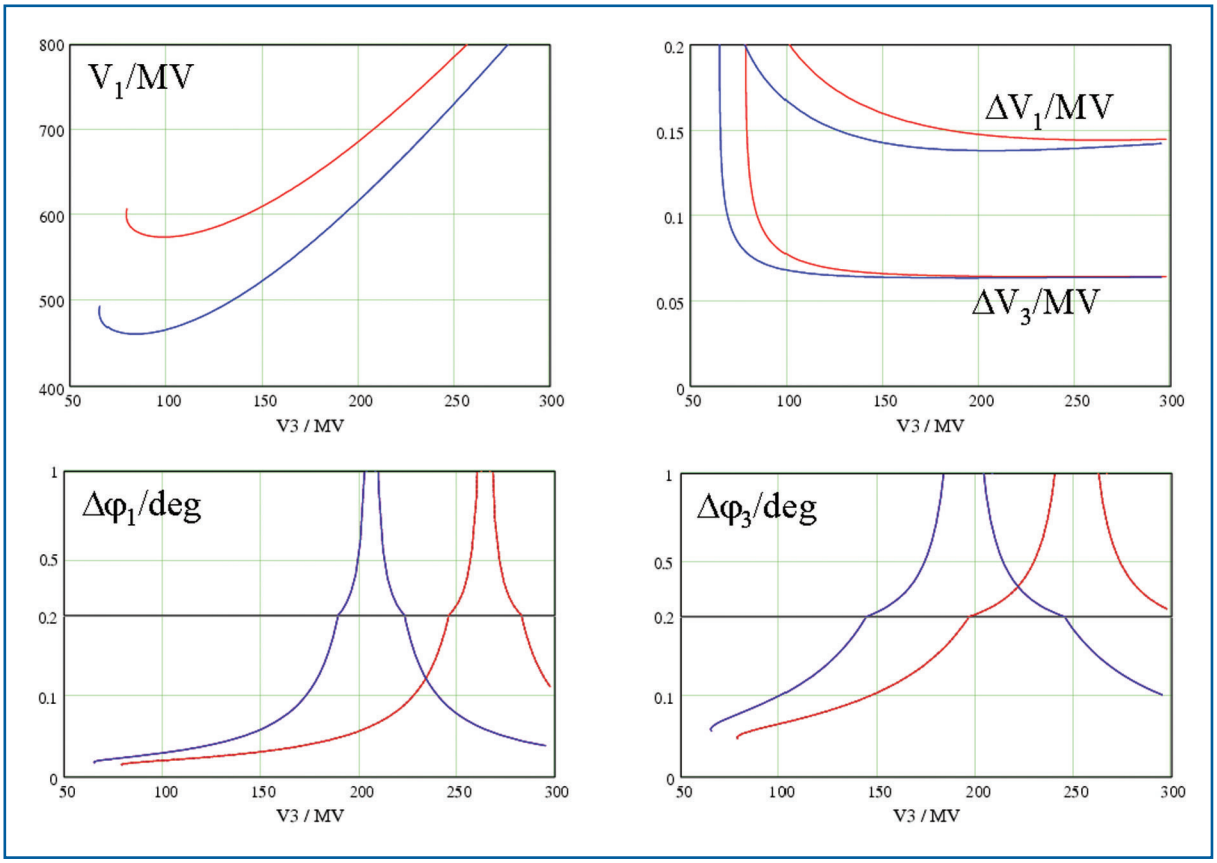

Figure 4.4.3 *RF amplitude dependence and amplitude/phase sensitivities for the fundamental mode RF and the third harmonic system. For the red lines, the beam energy at the first chicane is 500 MeV, for the blue ones 400 MeV. The upper left graph shows the amplitude of fundamental harmonic RF system against third harmonic RF amplitude. For the other three graphs, on the vertical axis the amount of phase or amplitude offset which causes a change of the final peak current by 10% is plotted, the horizontal axis shows the amplitude of the third harmonic RF system. Upper right graph: Amplitude sensitivity of both RF systems. Lower left: Phase sensitivity of the fundamental harmonic RF system. Lower right: Phase sensitivity of the third harmonic RF system.*

The phase jitter sensitivity can be reduced by more than an order of magnitude if the third harmonic system is operated with an amplitude of about 200 MV (for the 400 MeV case). At that working point, phase jitter tolerances are of the order of a degree for both RF systems, compared to a few hundredths of a degree for a working point with third harmonic amplitude of about 100 MV. The amplitude jitter tolerances are 3×10^{-4} for the third harmonic RF and 2×10^{-4} for the fundamental mode RF.

At that working point, a cancellation loosens the RF phase jitter tolerances: A change in one of the RF phases causes a change in beam energy and in the induced chirp. The phase jitter sensitivity is reduced if the effectively reduced longitudinal dispersion of the magnet chicane due to the higher beam energy is compensated for by a stronger chirp. An RF system with a single frequency cannot provide this, but for two RF systems such a working point exists.

In general, the relative priorities for peak current and timing stability together with the actual stability of RF amplitudes and phases will determine the RF parameter settings.

4.4.4 Instabilities driven by space charge and coherent synchrotron radiation

An initial bunch current ripple can be amplified by the following mechanism: a slight modulation of the initial bunch density profile produces an energy modulation due to longitudinal impedance, caused by CSR and space charge fields. In a bunch compression chicane, the energy modulation creates more density modulation. In a multi-stage bunch compression system, the gain of this amplification can be very high. A limiting factor for this mechanism is the uncorrelated energy spread.

For the calculation of gain curves, a bunch with an initial charge modulation of wavelength λ is traced from the gun to the entry of the undulator. The gain is the amplification of the relative modulation amplitude in the simulation.

The gain of the so called 'CSR Instability' was calculated with the 3-D code CSRtrack and found to be < 10 **[4-76]**.

Figure 4.4.4 shows gain curves for the space charge driven instability for different initial random energy spread. The calculated gain at the expected small values for uncorrelated energy spread from the gun (rms < 2 keV) would be sufficient to start amplification from shot noise. With a 'laser heater' **[4-85]** (a magnet chicane approximately two metres long with an undulator magnet which the electron beam traverses together with a laser beam) we can adjust the uncorrelated energy spread between its initial value and up to 40 keV. The initial uncorrelated energy spread must be above 10 keV to limit the modulation of the bunch after the last compressor chicane to less than 1%.

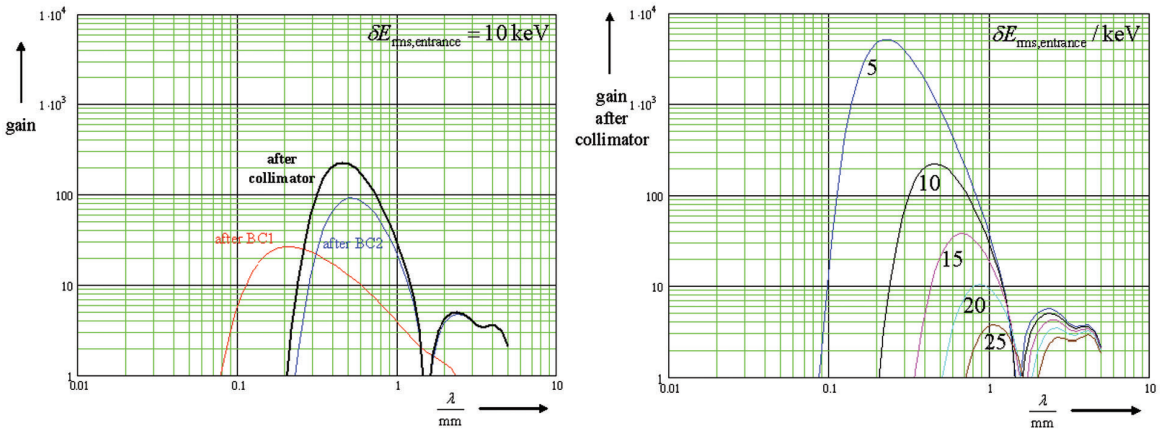

Figure 4.4.4 *Gain curves for the space charge driven instability. Left side: Contributions of the sub-sections of the linac for an uncorrelated energy spread of 10 keV. Right side: Overall gain for different uncorrelated energy spreads.*

4.4.5 Start-to-end simulation

4.4.5.1 Tracking through the accelerator

In the following we present a start-to-end simulation for the nominal operation parameters. The lattice and the optics were taken directly from the European XFEL reference list **[4-86]**. Parameters for the compression are listed in Table 4.4.2.

1.3 GHz linac phase before first chicane	1.4	degree
1.3 GHz linac amplitude before first chicane	442.85	MV
Third harmonic RF phase	143.35	degree
Third harmonic RF amplitude	90.63	MV
Linac phase first chicane to second chicane	20.0	degree
Linac amplitude first chicane to second chicane	1596	MV
Longitudinal dispersion (R56) of first chicane	-103.4	mm
R56 of second chicane	-17.6	mm

Table 4.4.2 *Compression system parameters for start-to-end calculations.*

The beam was traced from the cathode of the RF gun to the entrance of the undulator using different codes in different sections. The straight linac sections are calculated using the space charge code ASTRA if the space charge forces are strong. The impact of weaker space charge forces, for instance in the main linac, are calculated with a semi-analytical model **[4-87]**. The bending sections like chicanes or doglegs are tracked using the 1-D model in the code CSRtrack. Extensive calculations have shown that 3-D calculations yield an only slightly modified result for the nominal parameters. Shielding effects of the CSR fields have been taken into account because they disturb the compensation of projected emittance growth between the two chicanes.

Wake fields for all RF structures are included. The simulation of the SASE process in the next chapter also includes wake field effects.

The beam parameters at the entrance of the undulator are shown in Figure 4.4.5. The peak current is at 5 kA as required and the (normalised) transverse slice emittance in the region where the current is above 2 kA is less than 1 mm-mrad.

The longitudinal phase-space shows that the linear part of the correlated energy spread is approximately zero, as expected. The non-linear kink in the centre of the bunch is generated by space charge forces in the main linac.

The energy spread along the bunch distribution peaks at the centre at 1 MeV, the initial value induced by the laser heater of 10 keV multiplied by the compression factor. The projected emittance is about 1.4 mm-mrad.

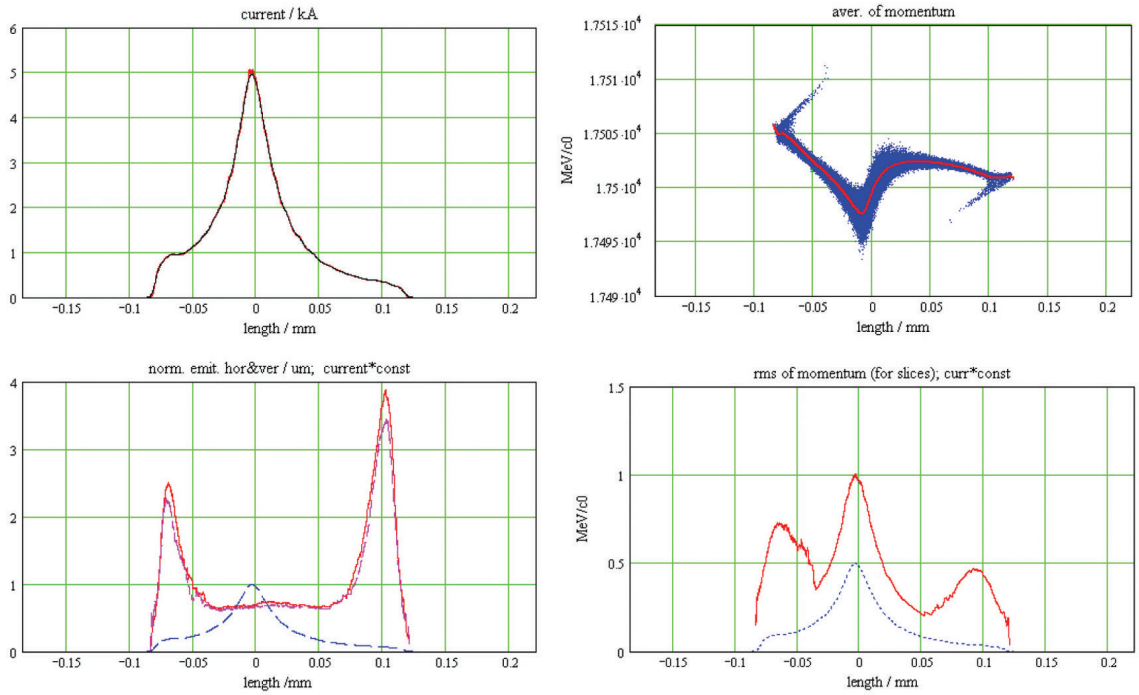

Figure 4.4.5 *Beam parameters at the entrance of the SASE undulator.*

4.4.5.2 X-Ray FEL Simulations

Wake field effects

For the long undulator, the wake fields in the undulator pipe and intersections have an important effect on the lasing process. The effect of wake fields becomes noticeable as a gain reduction when the variation in energy becomes big compared to the FEL bandwidth, i.e. $\Delta E_{wake} / E > \rho$. In the case of SASE 2, this is true if $\Delta E_{wake} > 41$ keV for a bunch of 1 nC passing through 1 m of the undulator vacuum chamber. This is usually expressed in the notation $\Delta E_{wake} > 41$ keV/(nC m).

There are three major sources of wake fields within the undulator: resistive wall, geometric and surface roughness. Geometrical wake fields arise in variation of the chamber along the undulator. These wake fields were calculated numerically **[4-88]** for the case of elliptical pipe geometry with semi-axes of 3.8 mm and 7.5 mm and for all insertions. The geometric wake for a Gaussian bunch with 25 μm length (rms) introduces an average energy loss of the electrons in the bunch of 12 kV/(nC m), and an energy spread of 4 kV/(nC m).

The resistive wall wake was estimated analytically **[4-90]** for a round pipe with a radius of 3.8 mm. Results for different materials and bunch shapes are shown in Table 4.4.3.

		Gaussian bunch Cu/Al	Rectangular bunch Cu/Al
Total energy loss	kV/nC/m	36/50	79/93
Induced energy spread	kV/nC/m	46/53	90/72
Peak energy loss	kV/nC/m	-89/-108	-256/-243

Table 4.4.3 *Energy losses due to resistive wall wake field parameters for different bunch shapes.*

Figure 4.4.6 shows the resistive wall (Cu) and geometrical wake potentials and their sum for the bunch in Figure 4.4.5. Surface roughness wake fields **[4-91]** are negligible and are not considered in the SASE FEL simulations presented here.

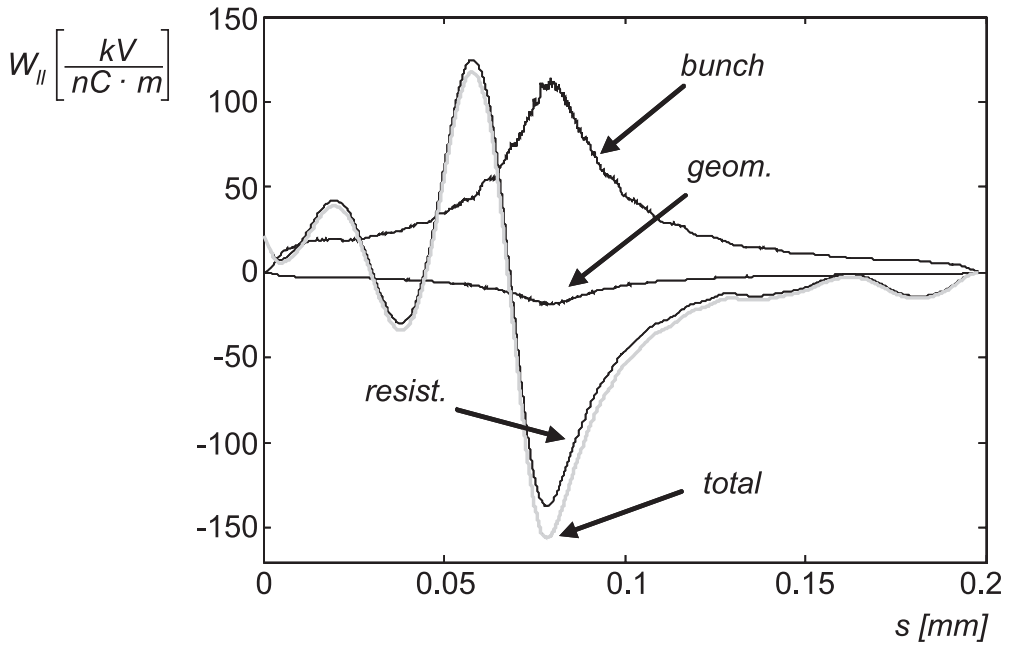

Figure 4.4.6 *Energy losses due to resistive wall wake (Cu) and geometrical wake field and their sum.*

SASE simulations

Figure 4.4.7 and Figure 4.4.8 show the radiation power for the case of the undulator SASE 2, calculated with the code Genesis **[4-92]**. When taking into account wake fields, the peak power is reduced from 80 GW to 50 GW. A linear undulator tapering of the magnet gaps ($\Delta K/K = 4\rho$) compensates the degradation and increases the radiation power up to 90 GW.

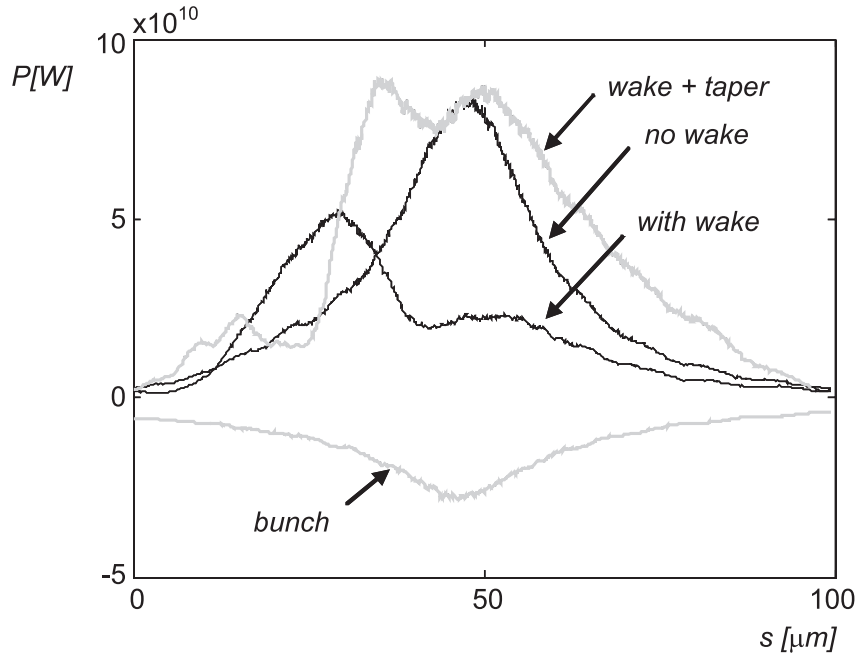

Figure 4.4.7 *Radiated power along the pulse at the end of the undulator.*

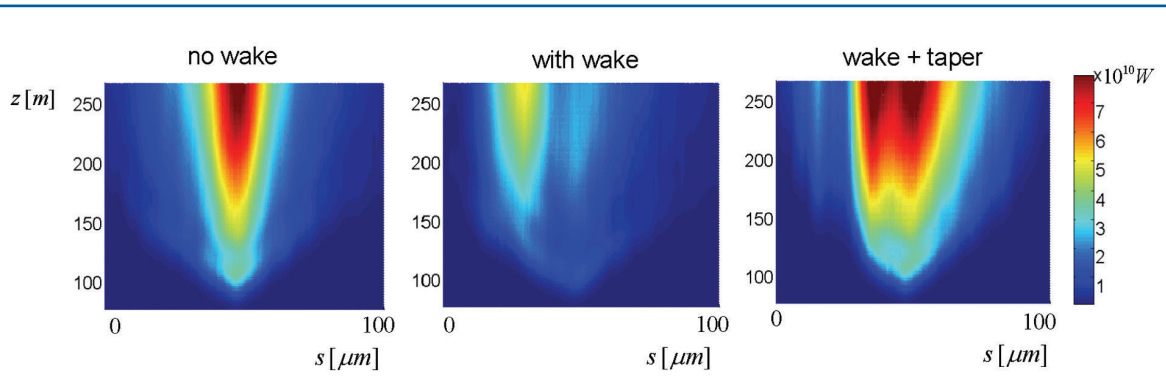

Figure 4.4.8 *Evolution of the radiated power pulse along the undulator for the three considered cases.*

The tapering requires an undulator gap variation of 32 μm over 260 m, imposing severe tolerance requirements on the undulator alignment.

4.5 Beam optics and dynamics

4.5.1 Main linac

The acceleration of the electron beam to the design energy of 20 GeV is performed in the booster linac (0.5-2 GeV) and main linac (2-20 GeV). They are separated by the bunch compression system. The main parameters of the beam at the entrance of each linac are summarised again in Table 4.5.1.

The main linac downstream from the second bunch compression consists of 100 accelerator modules with one quadrupole each forming a FODO cell with 24 m length and a phase advance of 60°. One horizontal or vertical steering magnet per module is foreseen. The booster linac contains six standard FODO cells with average gradient in cavities of about 16 MV/m.

		Booster linac	Main linac
Initial energy	GeV	0.5	2
Acceleration gradient	MV/m	16	20.8
Bunch length	μm	121	24
Initial correlated energy spread	%	1.75	0.4
Initial uncorrelated energy spread	%	0.1	0.125

Table 4.5.1 *Beam parameters at the entrance of booster and main linacs.*

4.5.1.1 Single bunch beam dynamics

The single bunch emittance dilution in linacs is determined by chromatic and transverse wake field effects. In the booster linac these effects are negligible due to the high relative energy gain of the particles compared to their initial energy. The weak wake fields in the superconducting 1.3 GHz accelerating structures and the low chromaticity of the focusing lattice leads to harmless beam dynamics in the main linac as well.

The RF accelerating field and the short range longitudinal wake field leads to an extra negative correlated energy spread (tail particles have lower energy than the head) with rms value of 5×10^{-4} at the end of the main linac. However, the electron bunch has an initial positive correlated energy spread of 0.4% (required for the bunch compression system). This initial energy spread partially cancels the induced correlated energy spread in the main linac, thus, providing an rms relative correlated energy spread at the linac exit (energy 20 GeV) of about 1.2×10^{-4} or absolute rms energy spread of 2.4 MeV (Figure 4.5.1).

The single bunch emittance dilution is mainly caused by the coherent oscillations of the beam due to transverse injection jitter, random cavity tilts and quadrupole misalignments. Cavity and module random misalignments are additional sources of correlated emittance growth due to transverse wake fields exited by off-axis beam trajectory in the accelerating sections. In Table 4.5.2 the rms tolerances to the main linac component misalignments are given.

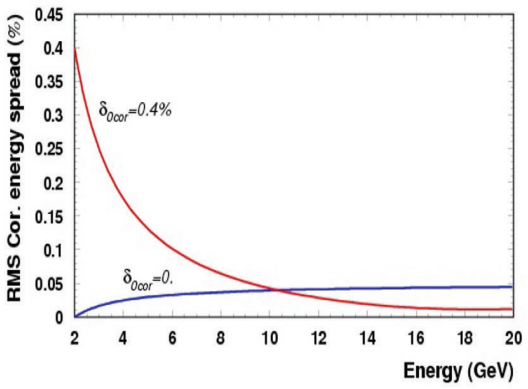

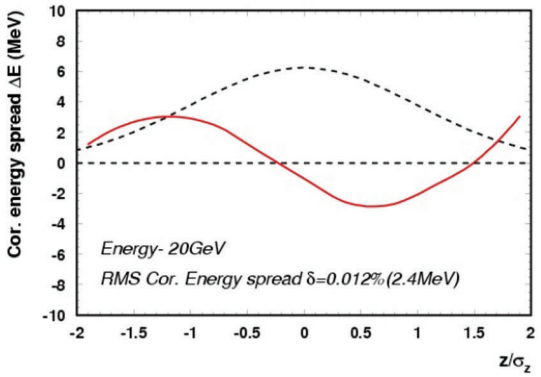

Figure 4.5.1 *The rms correlated energy spread along the main linac with (red) and without (blue) initial positive correlated energy spread (left). Absolute correlated energy deviation within the bunch at the linac exit (right).*

Injection transverse jitter	1 σ	
Cavity module misalignments	0.5	mm
Modules Misalignments	0.5	mm
Correlated 4 modules misalignment	0.5	mm
Cavity tilts	0.25	mrad
Quadrupoles module misalignments	0.5	mm
BPM module misalignments	0.2	mm

Table 4.5.2 *Assumed rms misalignment tolerances.*

The left-hand graph in Figure 4.5.2 presents the transverse-wake field caused correlated emittance dilution along the linac for cavity and module misalignments. The results are averaged over 25 random seeds of misalignments and are negligibly small due to weak transverse wake fields in the accelerating sections. In the case of cavity random tilts, the particles experience the transverse Lorenz-force of the accelerating RF field and the beam performs coherent oscillations. The right-hand graph in Figure 4.5.2 presents the correlated and uncorrelated chromatic emittance dilution along the linac caused by the initial energy spread.

The strongest impact of the chromatic effect is observed for a disturbed central trajectory caused by quadrupole misalignments. The steering of the central trajectory is supposed to use one-to-one correction algorithm: the beam trajectory is corrected in each focusing quadrupole to its geometrical axis based on the BPM reading by correction dipole coils incorporated in the previous quadrupole. Figure 4.5.3 presents the disturbed central trajectory of the beam in the main linac for one single random seed of quadrupole misalignment, the corrected trajectory and the resulting uncorrelated and correlated chromatic emittance dilution of the beam.

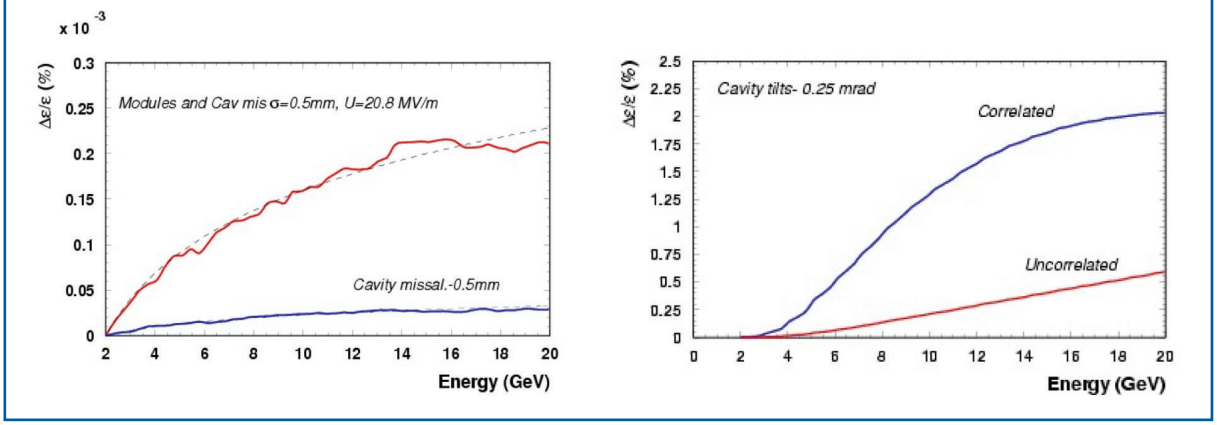

Figure 4.5.2 *Wake field caused emittance dilution along the main linac for cavity and modules random misalignments (left). The chromatic emittance dilution along the main linac for cavity random tilts (right).*

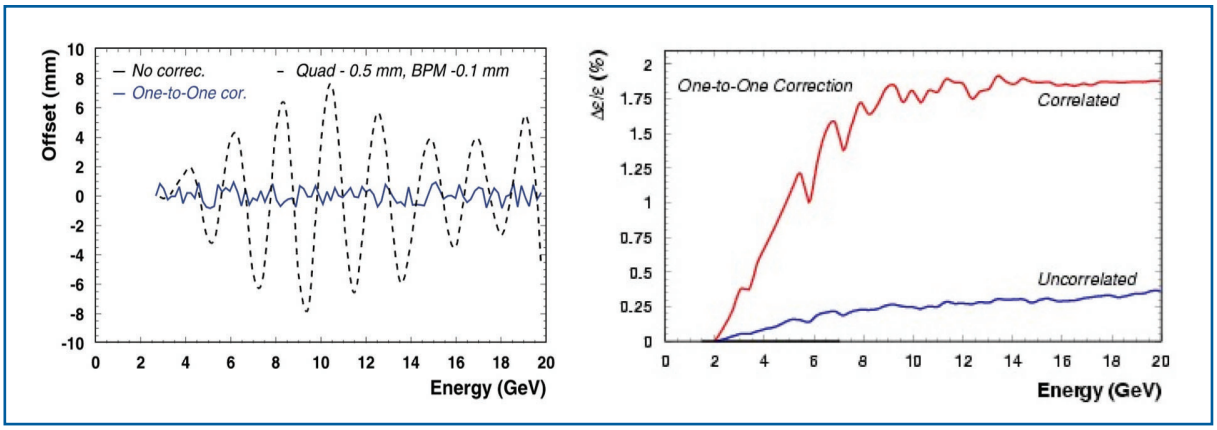

Figure 4.5.3 *Coherent betatron oscillation of the beam in the main linac with misaligned quadrupoles and steered trajectory by one-to-one correction algorithm (left). Correlated and uncorrelated emittance dilution along the linac after trajectory steering (right).*

Table 4.5.3 presents the summary of the emittance dilution in the booster and main linac.

	Booster Linac	Main Linac
Coherent oscillations		
Uncorrelated	6×10^{-6}	2×10^{-4}
Correlated	2×10^{-3}	1.2×10^{-3}
Cavity misalignments	5×10^{-6}	3×10^{-7}
Modules misalignments	4×10^{-5}	2.5×10^{-6}
Correlated misalignments (4 modules)	-	7×10^{-6}
Cavity tilt		
Uncorrelated	5.8×10^{-5}	0.6%
Correlated	0.6%	1.9%
One-to-one correction		
Uncorrelated	6.3×10^{-5}	0.4%
Correlated	1.7%	2%
Total	< 3%	< 5%

Table 4.5.3 *Summary of the emittance dilution in booster and main linacs.*

4.5.1.2 Multi-bunch beam dynamics

The effect of the long-range transverse wake field on multiple bunches has been investigated for various cases **[4-93]**. A cavity misalignment of 500 μm rms has been assumed. A typical behaviour of the bunch offset at the end of the linac is shown in Figure 4.5.4. After ≈50 μs a steady state is reached and its value is unchanged as long as the beam trajectory through the linac is unchanged. Moreover, the initial oscillation is largely repetitive and can, thus, be handled by an intra-train feed-forward system.

Figure 4.5.4 shows the average emittance growth along the linac, being only 0.02%, relative to the design slice emittance. The major contribution again comes from the first part of the bunch train. Consequently, the average emittance dilution gets larger for shorter trains, where the steady state is not reached. For high quality beam applications a bunch train of at least 200 bunches should be accelerated, with the first 100 bunches leading to a steady state wake field excitation while the remaining bunches pass the linac almost unperturbed. The unperturbed emittance can be restored by a fast intra-train feed-forward system **[4-94]**.

The longitudinal HOMs lead to an energy spread along the bunch train. As in the transverse case this is strongest for the first part of the bunch train (5.15 MeV rms for a 20 μs bunch train) while the rms energy spread over the whole train is 0.88 MeV. This variation again is repetitive and should be compensated for by the low-level RF system.

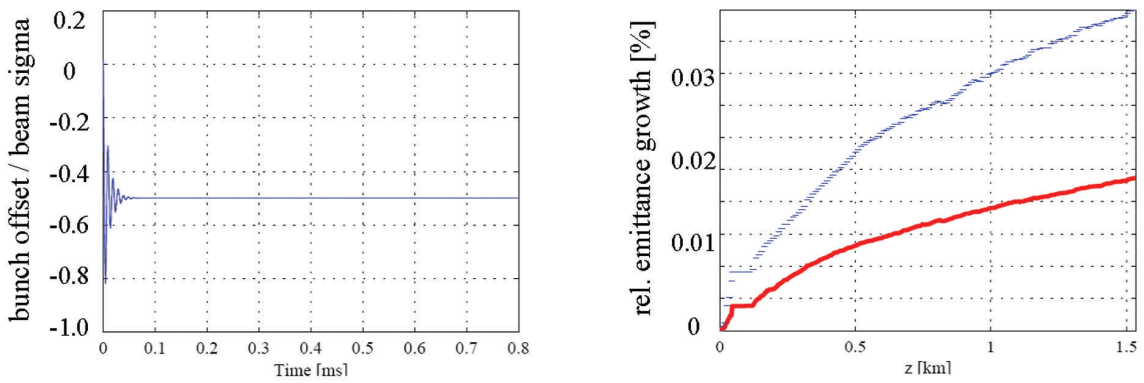

Figure 4.5.4 *Simulation results for 20 GeV final energy, 200 ns bunch spacing and 4,000 bunches/train. Left: Bunch offset along a bunch-train. Right: Emittance growth along the linac (red line: average over 100 random seeds, blue line: maximum of standard deviation).*

4.5.2 Post-linac collimation

The collimation system simultaneously fulfils several different requirements:

- during routine operation, off-momentum and large amplitude halo particles are removed with high efficiency;
- in case of machine failures, downstream equipment and undulators are protected against mis-steered and off-energy beams, without destroying the collimators in the process;
- the energy acceptance is an important requirement for the optical design of the collimation system. The collimation section is able to accept bunches with different energies (up to ±1.5% from nominal energy) and transport them without any noticeable deterioration.

Figure 4.5.5 shows the optical functions of the post-linac collimation lattice. The system consists of two arcs separated by a phase shifter. It has a dogleg shape. The arcs are identical and each one constitutes a second-order achromat. The collimation section includes matching modules to adapt the optic to the desired upstream and downstream beam behaviour.

The collimation system utilises a spoiler-absorber scheme and is designed as passive, i.e. without an integrated fast emergency extraction system, fast sweeping system or fast beam enlarging system. The spoilers must be able to withstand a direct impact of about 80-100 bunches until a failure is detected and the beam production in the RF gun is switched off. In order to find the minimum tolerable beam-spot size at which a spoiler made from Titanium alloy will survive even in the worst, but theoretically still possible, case when all these bunches will hit it exactly at the same point, the interaction of a bunch with a spoiler was investigated using the EGS4 code. The simulation results show that it is sufficient to have both beta functions above approximately 250 m at the spoiler locations, assuming a normalised emittance of 1.4 μm, beam energy of 20 GeV and bunch charge of 1 nC.

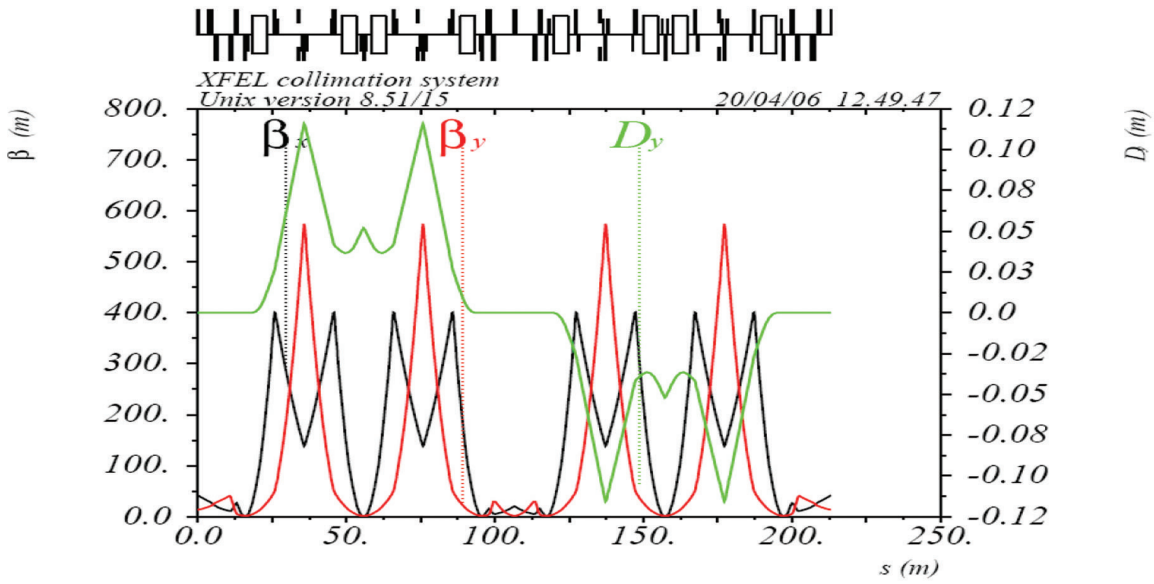

Figure 4.5.5 *Optical functions of the collimation system including upstream and downstream matching sections.*

Four spoilers will be used in total, two in each arc. The first arc collimates transverse positions of incoming particles and the second, after a shift of horizontal and vertical phases by 270°, their transverse momenta. The energy collimation and the vertical plane collimation will be done simultaneously, and therefore, the ratio of dispersion to vertical betatron function at spoiler locations is properly adjusted. Collimators are chosen to have circular inner apertures (conical tapered collimators). Analytical and numerical studies have shown that spoilers with inner radii of about 3.8 mm will be able to protect the undulator vacuum chamber (at current stage, assuming that downstream beam transport is linear) and also stop all particles with an energy offset larger than ±3.5%. An example of such investigations is shown in Figure 4.5.6. The initial distribution of the incoming particles was modelled by mono-energetic 4-D slices, with a transverse extension over the radius of the vacuum chamber at the collimator section entrance (the maximum values for transverse momenta were chosen so as to fully populate the acceptance of the transport line). The results are presented as a function of the energy deviation.

The effect of energy offsets, optics nonlinearities and incoming beam mismatches on the evolution of the beam-spot size along the collimation section can be seen in Figure 4.5.7. Simulations show that all particles with transverse offset larger than ≈80 σ (at energy 20 GeV) will be collimated by touching one of the spoilers. All particles with transverse offset smaller than ≈23 σ will pass through the collimation section freely. Some particles with offsets between 23 to 80 Ã are absorbed in the vacuum system of the collimation section.

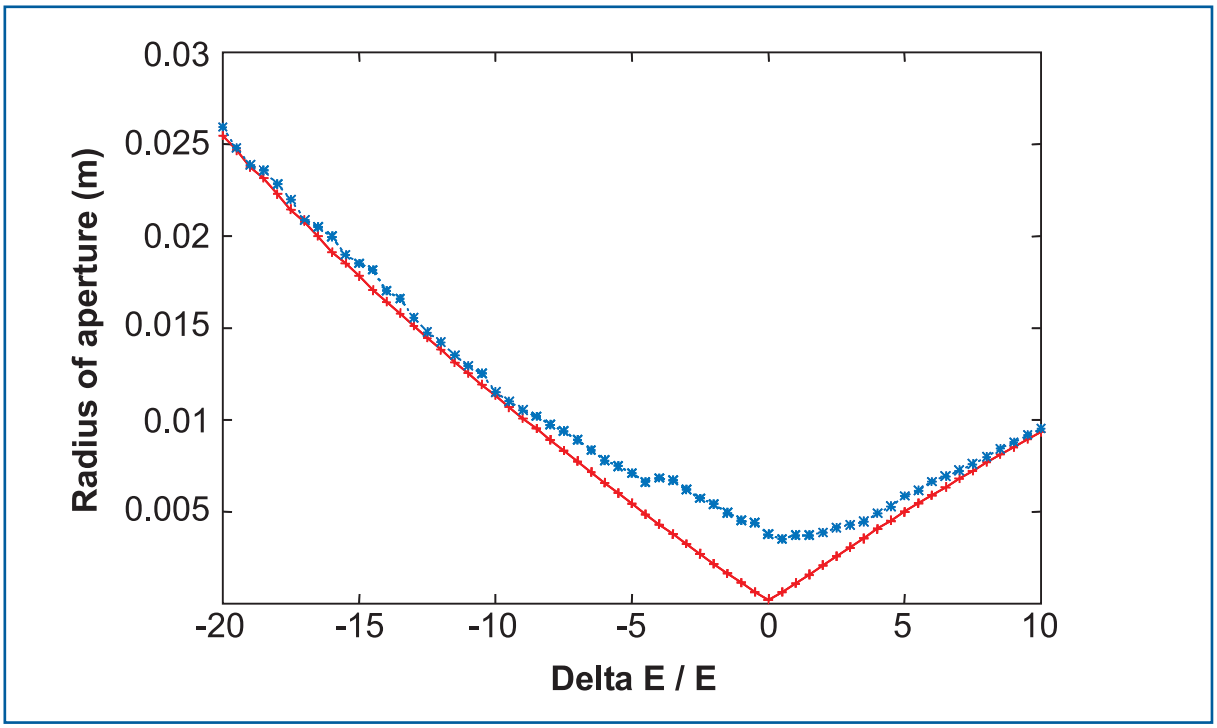

Figure 4.5.6 *Blue curve: Aperture radius required to protect the undulator vacuum chamber as a function of the energy deviation. Red curve: Aperture radius required to block the corresponding off-energy fraction of incoming particles in the collimation section.*

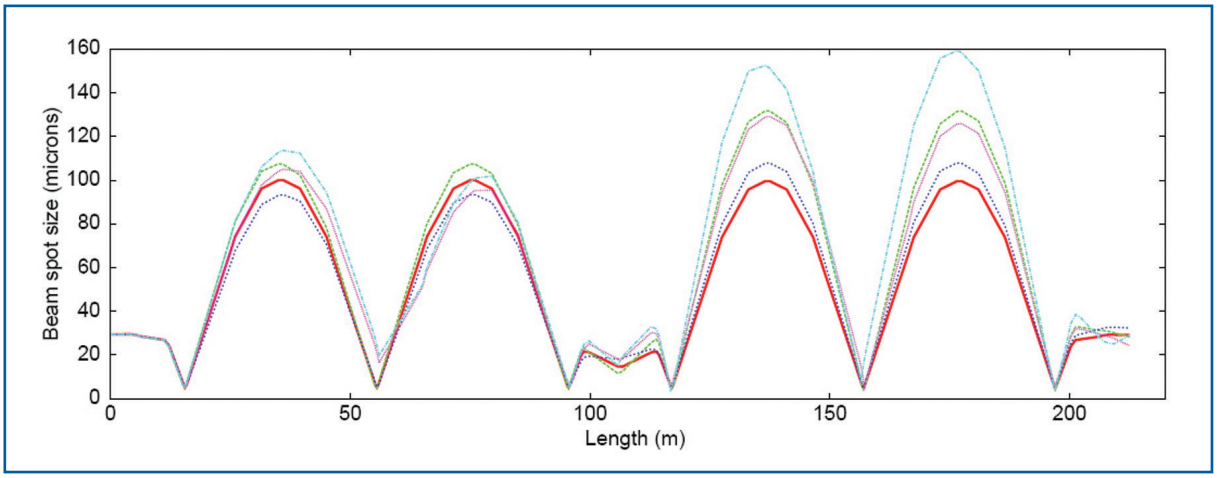

Figure 4.5.7 *Evolution of beam-spot size (rms value) along the collimation section. Red curve shows the design spot size (linear theory). All other curves are results extracted from the tracking simulations. A matched Gaussian beam at the entrance with -3% (green) and +3% (blue) energy offsets, with 40 σ y-offset (magenta), and with both -3% energy and 40 σ y-offsets (light-blue).*

4.5.3 Beam distribution and undulators

4.5.3.1 Beam distribution

Operational flexibility for each user is reached by a flexible beam distribution system. This system will allow complete and independent control over the bunch pattern for each electron beamline. The key components of this system are a very stable flat-top kicker for beam distribution into the undulator beamlines and a fast single bunch kicker to kick individual bunches into the beam dump before the beam distribution.

During one pulse, the beam is switched once between the two beamlines by means of the flat-top kicker. While the kicker field is being ramped up, the beam is aborted in the beam dump before the beam distribution with the help of the fast single bunch kicker. Individual bunch patterns are created by aborting 'unwanted' bunches in the beam dump. The beam extraction is realised with a kicker/septum layout, thus reducing the required kick strength for the kicker.

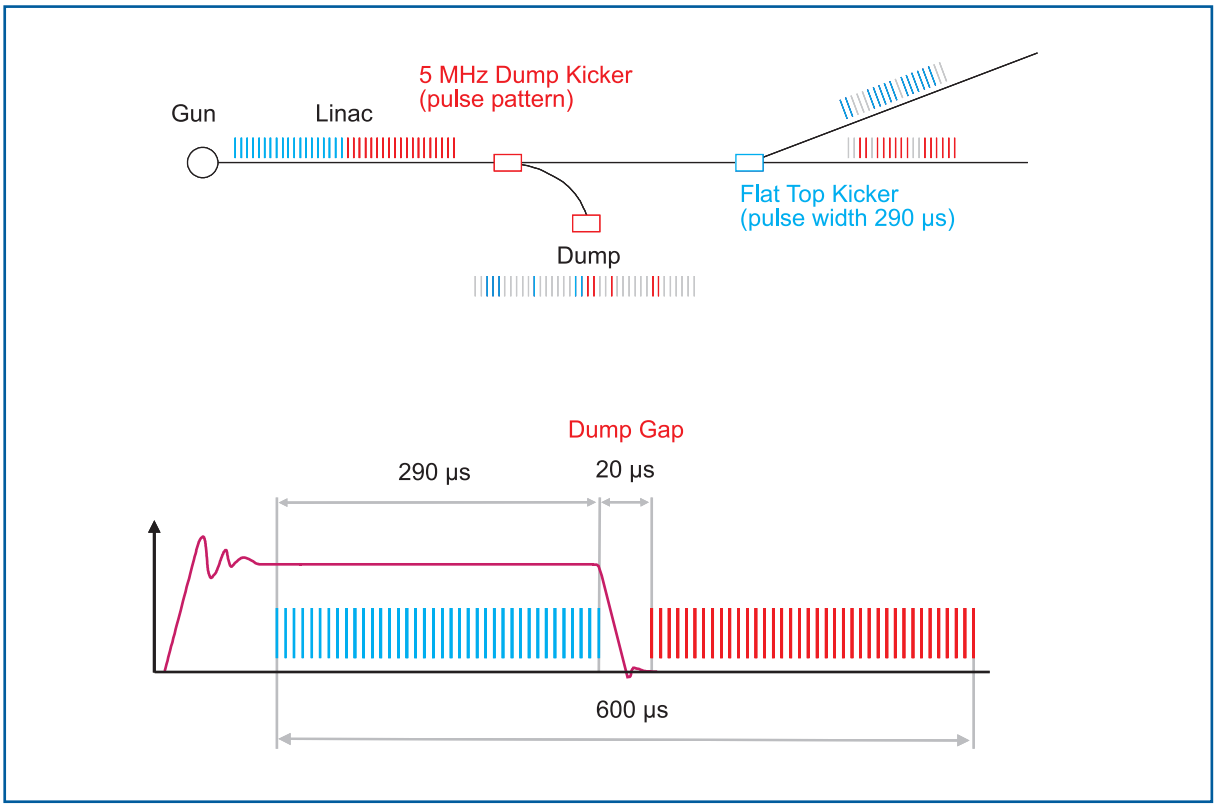

Figure 4.5.8 *Beam distribution concept: The linac is operated with a constant beam distribution. Bunches are distributed into the beamlines with a flat-top kicker once per pulse. During the ramp up of this kicker (dump gap is extended in this plot for better visibility) the bunches are aborted in the beam dump, as well as other unwanted bunches out of the train.*

The betatron function in the septum is limited by incoherent synchrotron radiation emittance growth to about 40 m (approximately the same as in the undulator). The upstream collimation protects a downstream aperture of larger than 4.5 mm at this betatron function. Thus, the kicked amplitude at a septum (with 5 mm septum width) is

15 mm, yielding a maximum kicker field of 0.375 mrad or 31 mT×m at 25 GeV. Downstream trajectory stability requirements (< 0.1 σ) lead to very tight relative amplitude and residual ripple requirements of 5×10^{-5}.

The bending sections leading to the five downstream undulators are designed as double-bend achromats with total bending angles between 1.3 and 2.5°. For phase two a deflection of ≈ 6.6° is required, which is realised with a triple-bend achromat with dipoles of twice the length. In all bending sections, sextupoles and octupoles provide higher order dispersion correction.

4.5.3.2 Undulator optics

The electron beam optics in the undulator consist of a simple FODO lattice with a cell length of 12.2 m. The average beta-function in the undulators should be variable between 15 to 45 m, yielding a phase advance between 50 and 15°. The corresponding inverse focal length ranges from 0.12 to 0.04 m^{-1}. The vertical focusing due to one 5 m long undulator segment is:

$$\frac{1}{f_y} \approx \frac{1}{2}\left(\frac{e}{p_0}\right)^2 B^2 l.$$

This amounts for B = 1 T and p_0 = 6 GeV/c to 0.006 m^{-1}. For low electron energies a retuning of the quadrupoles according to the undulator configuration is thus necessary, while for nominal energy the influence of the undulator focusing is negligible.

The beam size in the undulator is about 35 µm, the slice energy spread is 1 MeV (10 keV after the injector). A dispersion of around 25 cm would, thus, lead to a beam size growth of 10%. A much more stringent requirement comes from the ±1.5% energy bandwidth together with the 1/10 σ constraint on orbit variations, leading to a residual dispersion of 0.1 mm. This corresponds to an average kick in the quadrupoles (due to orbit errors or quadrupole misalignment) of ≈ 15 µrad. SASE operation requires trajectory angles in the order of a few tenths of a µrad, thus yielding the most stringent requirement for the orbit in the undulator. Orbit correction methods based on dispersion-free steering algorithms require a resolution of the dispersion measurement in the order of 10 µm. The collimation system has an energy bandwidth of 6%, leading to a requirement of the BPM resolution in the order of 0.5 µm (if no retuning of the upstream magnet lattice is applied during the measurement/correction).

4.5.4 Transverse beam stabilisation

4.5.4.1 Introduction

First start-to-end simulations of the European XFEL indicate that transverse beam motions in the order of a few tenths of the rms beam sizes seem to be acceptable for stable SASE operation. Moreover, the pointing stability of the photon beam leads to a stability requirement of 0.1σ for the electron beam. Such beam stabilities on a micron or even sub-micron level are regularly achieved in today's third generation synchrotron

light sources within a frequency band of 10^{-4} Hz up to several hundred Hz using global or local beam feedback systems to actively stabilise the CW-like bunch patterns of storage rings (see for example SLS, ESRF, ALS). The same micron-level beam stability needs to be achieved for a SASE-based user facility like the European XFEL for its proposed bunch structure of 600 µs long bunch trains with bunch distances of 200 ns at a 10 Hz repetition rate. The frequency range from a few Hz up to some kHz, where most of the beam position disturbances are generated by noise sources such as ground motions, cooling water and Helium flow, power supply jitter, switching magnets, RF transients and jitter, photocathode laser jitter and related beam current variations as well as long range wake fields, remains inaccessible for relatively slow closed orbit feedback systems as used in storage rings. Their range of application will be limited to the stabilisation of drifts and low frequency beam motions up to a few Hz. A fast feedback system, however, with a low latency time (preferably < 200 ns) can make use of the long macro pulses of the European XFEL with about 3,000 consecutive bunches to damp beam motions in a frequency range from a few kHz to several hundred kHz applying modern control algorithms in a feedback loop. Both, long range (from bunch train to bunch train) and fast (bunch-by-bunch) repetitive beam movements can be eliminated by adaptive feed-forwards. The basic design considerations and main characteristics of a prototype intra-bunch train feedback (IBFB) system for the European XFEL are introduced in the following section. Such a system is presently developed. It will be tested under “real” SASE conditions at FLASH (VUV-FEL) at DESY and can be considered as the central part of a general beam stabilisation strategy as required for the European XFEL, including electron and photon beam-based diagnostic devices for active stabilisation of the electron beam and critical accelerator components.

4.5.4.2 Intra-bunch train feedback system

The present layout and beam distribution concept of the European XFEL requires only one bunch-by-bunch feedback system for transverse beam stabilisation at the final beam energy of 20 GeV. This system will be located in the beam transport section behind the main linac before the beam distribution system. A schematic view of the IBFB topology is shown in Figure 4.5.9.

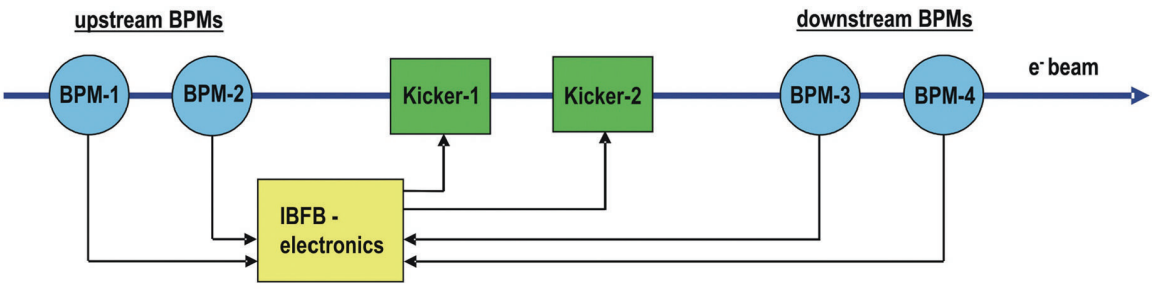

Figure 4.5.9 *Topology of IBFB for the European XFEL.*

The IBFB will make use of two upstream and two downstream BPMs for beam position measurements and two fast electromagnetic kickers in between for application of corrections. The proposed topology of using the upstream BPMs for the measurement of the uncorrected beam positions is optimised for lowest latency times through the system, since beam and feedback signals travel in the same direction. The downstream BPMs allow the verification of the feedback model by checking whether the applied kicks lead to the expected corrections. Thus, static and dynamic effects like kicker scaling errors or inaccuracy in the optics model can be detected and eliminated. In the same way, it will be possible to predict long range beam movements from bunch train to bunch train and thus, correct for repetitive disturbances through slow adaptive feed-forwards using look-up tables.

All IBFB components will be installed in the accelerator tunnel. Only short cable connections can be used to keep the system latency time below the bunch-by-bunch distance of 200 ns. The main IBFB components are:

- dedicated strip-line BPMs (at 1.625 GHz) for beam position measurement with a resolution of 1 μm;
- RF front-end for analogue signal conditioning;
- digital electronics including analogue to digital conversion, real-time data processing, calculation of corrections and back-conversion from digital to analogue;
- power electronics and fast electro-magnetic kickers for application of the correction kicks onto the electron beam.

While the strip-line BPM design will be optimised to generate well matched input signals for the RF front-end, the digital part of the system will follow a highly flexible and modular approach by using FPGA-based technology for calculating fast corrections and a set of DSPs for model-based adaptive feed-forwards. In this way, it will be possible to constantly adapt the feedback model in the data processing part of the IBFB to the actual operating conditions of the real accelerator. Interconnection with other complementary feedbacks and accelerator components will be achieved through fibre optic, multi-Gigabit links, like Rocket I/Os, providing the possibility of sharing all relevant information for beam stabilisation on a real-time basis. Beam-based information from the IBFB system could, thus, be used to improve, e.g. low level RF stability. Likewise, real-time data exchange between different electron beam and photon beam position diagnostics may allow efficient cascading of feedbacks and permit the adaptation of feedback models for stable SASE operation.

4.5.4.3 IBFB as an integral part of the XFEL beam stabilisation strategy

Cascading of beam-based feedbacks and data exchange from different beam diagnostics like electron and photon BPMs have already proven to be the most efficient ways of stabilising the radiation sources of third generation synchrotron radiation facilities. In case of a highly non-linear radiation process like SASE with its noticeable inherent (statistical) fluctuations, it will be even more important to share all relevant information about beam parameters between accelerator sub-systems on a real-time basis. In this respect, beam stability at an XFEL user facility depends not only on the optimum performance of

individual components but more importantly on an efficient matching and integration of all measurement and correction devices as well as critical accelerator sub-systems. It is, therefore, of great importance, that the fields of application and performance ranges of different diagnostics components in terms of bandwidth, resolution, dynamic range, stability and other relevant parameters are well adjusted to each other and that a time-stamped and well correlated view of the accelerator behavior is available on a real-time basis. Standardisation of interfaces including fast data links as well as clear definition of hardware and software concepts are prerequisites for realising such a general beam stabilisation concept. In this way, a vast number of components such as standard electron BPMs and photon beam diagnostics, including the online measurement of photon beam position, intensity, line-width, etc. as well as accelerator sub-systems like timing, low level RF and even gun laser control, can be treated as an integral part of a comprehensive stabilisation strategy, where the IBFB system will not only be used to stabilise the beam position at the location of the SASE radiation sources with highest bandwidth but will also provide important bunch-by-bunch information to support accelerator operation of the European XFEL as a multi-user facility.

4.6 Beam diagnostics

4.6.1 Requirements

A bunched electron beam of extremely high quality is needed in the XFEL to obtain high gain and saturation in the SASE process at sub-nanometer wavelengths. The specified parameters are given in Table 4.6.1.

Bunch length σ_z	20	µm
Peak current I	5	kA
Relative energy spread σ_E/E	$\approx 10^{-4}$	
Orbit deviation in undulator	3	µm
Directional accuracy in undulator	0.1	µrad
Arrival-time jitter (rms)[4]	60	fs

Table 4.6.1 *Electron beam parameters within a SASE undulator.*

These tight specifications put very demanding requirements on the accelerator and its instrumentation. Special diagnostic tools have to be developed to measure the relevant quantities with sufficient precision. Moreover, feedback systems are indispensable for achieving and stabilising the desired beam quality. The input signals for the feedback loops must be provided by devices that are capable of detecting the deviation of a beam parameter from its nominal value in a non-destructive manner, in order not to disturb the XFEL user operation.

[4] The arrival-time of each bunch can be determined to better than 30 fs.

The beam properties in a single pass machine vary over a wide range during the passage through the machine, thus they have to be measured at various places, resulting in a quite high density of diagnostics all over the machine.

The development of the diagnostics for XFEL will follow the general trend in accelerator instrumentation of using digital systems more intensively and it is planned to use a distributed system of electronics close to the position of the monitor in the beam pipe. These localised stations are then connected to the controls by fast digital interface systems. This should reduce the sensitivity to noise and electromagnetic interference (EMI), but might require more local radiation shielding.

In the following, the various diagnostic instruments are described that are foreseen for the XFEL. Two basic types can be distinguished: dedicated diagnostic instruments for accelerator studies; and optimisation and online diagnostics for monitoring the accelerator performance during XFEL user runs and for providing the input signals to the feedback loops. The former instruments, usually high-resolution systems, may have detrimental effects on the beam quality and may, therefore, be incompatible with user operation of the XFEL.

4.6.2 Measurement of projected bunch properties

The XFEL accelerator is a pulsed device, where the characteristics of the electron beam can vary from train to train but also within certain limits inside the train from bunch to bunch. Therefore, each measurement of a beam property has to be treated as a single data point that is connected to one bunch in a certain train. The set of all these data points allows characterisation of the bunch, and correlation of its properties with other bunches. Therefore, single bunch resolution is one main requirement for many diagnostic devices. On the other hand the tolerances, which are ruled by the SASE process, are very tight. An additional complication could be a trend towards decreasing the bunch charge in order to improve emittance, resulting, of course, in a decrease of signal amplitude for the electronics. The following bunch parameters are characterised by means of standard diagnostics.

4.6.2.1 Compression

Coherent radiation is emitted when the beam traverses a strong dipole field or passes a diffraction radiator. The emitted radiation power is proportional to the square of the bunch form-factor and increases with decreasing bunch length. Variations in the bunch peak current can, therefore, be easily monitored by far-infrared detectors.

At FLASH (VUV-FEL), monitoring the coherent diffraction radiation has become a standard tool to stabilise the RF acceleration phase of the linac.

Future designs will attempt to detect, in a single shot, the frequency spectrum emitted by the electron bunch **[4-95]**. The spectral power carries important information on the source of the longitudinal profile variation and complements the electro-optic data to control the fast longitudinal feedback loops.

4.6.2.2 Beam position

About 500 BPMs are required along the whole machine. Due to different machine environments (space and beam pipe) different types of BPMs have to be used, and:

- 117 cold BPMs are foreseen in the accelerator modules, either of pick-up type or re-entrant cavity type **[4-96]**;
- striplines and button BPMs similar to the ones used in TTF2 will be used in the warm beamlines;
- in the undulator, the resolution of these standard types is not sufficient. Therefore, cavity BPMs with a resolution about 1 μm are planned for the intersections between the undulator segments;
- special attention has to be put on the BPMs in the dispersive parts of the bunch compressors, since they have to deliver precise information about energy and energy fluctuations in the bunch compressors. The goal is to reach a few μm resolution while measuring wide distributions in a wide, but flat, vacuum chamber.

4.6.2.3 Beam size/emittance

Emittance is one of the most crucial parameters for the lasing process. Except for adiabatic damping due to the acceleration process, the phase-space volume produced at the injector can only increase during acceleration and beam transport. Therefore, emittance measurement stations have to be available at several positions in the machine, e.g. at the injector, the bunch compressors and after the main linac. All stations will consist of at least four beam size measurement devices, so that the phase ellipse of the beam can be measured without applying quadrupole scans. Usually, the stations are combinations of optical transition radiation (OTR) screens and wire scanners located next to each other. This allows coverage of a wide beam intensity range from machine start-up to long bunch train operation.

Additional tools for monitoring beam size are synchrotron radiation monitors in the bunch compressors and post-undulator beamlines to determine the energy distribution, as well as simple screens to aid machine start-up.

4.6.2.4 Beam intensity

The beam intensity is measured by current transformers, the so called toroids, which are installed at the beginning and end of each warm section. In addition to the nominal beam current *also* dark current emitted by RF resonators at high gradients is created. Especially dark current from the gun can be transported through the entire machine. Dark current will be monitored before and after dispersive sections and collimators in order to control its transport and optimise the collimation efficiency. Faraday cups for current measurements at the gun and low energy dumps complete the system.

4.6.2.5 Beam loss/radiation dose

The amount of energy transported within the long bunch trains is very high (up to 65 kJ/train). Even fractional beam loss can result in severe mechanical damage. Small fractions of the beam or dark current lost in the machine, produce radiation backgrounds and activation that will result in the strongly reduced lifetime of electronics, permanent magnet undulators or other sensitive components. Therefore, loss monitors measuring the dose and protection systems acting on different time scales are required. This ranges from fast interlock systems interrupting the bunch train on the µs level, up to systems watching the integrated dose and finding the hotspots in the machine to prevent long-term damage.

In order to provide signals for the protection systems, about 250 fast beam loss monitors will be installed at critical places along the machine. This network of fast monitors will be accompanied by fibre systems allowing the survey of bigger areas in the machine tunnel.

4.6.3 Measurement of slice properties

4.6.3.1 Transverse deflection structure

The transverse deflecting structure (TDS) is a very multipurpose instrument allowing longitudinal and transverse phase-space analysis with high resolution. The basic idea is simple: the electron bunch is deflected by a rapidly rising electromagnetic field whereby the longitudinal time coordinate inside the bunch is transformed into a spatial coordinate on an observation screen. The system functions in analogy to a conventional oscilloscope tube in which the electrons are deflected by a sawtooth voltage and the time axis of the input pulse appears as the horizontal axis on the screen. In the TDS, the deflecting field is generated by exciting the structure to an eigenmode (TM11-hybrid) exerting a strong transverse force on the electrons. The bunches cross the cavity at zero crossing of the TM wave. The length of the streaked pulse on the screen corresponds directly to the bunch length while the width of the streak is a measure of the beam size and can be used to determine the transverse emittance in the direction perpendicular to the plane of deflection. This emittance can be derived as a function of the longitudinal position in the bunch. Moreover, if the streaked bunch is sent into a spectrometer dipole, the energy of the electrons can be measured as a function of their longitudinal position. An important feature of the TDS is that the RF field is applied in pulsed mode so that an arbitrary bunch in a macro-pulse can be streaked without perturbing the straight trajectory of the other bunches in the train.

Longitudinal bunch charge distribution

The longitudinal charge distribution in the compressed electron bunches is one of the most critical quantities. The transverse streak provided by the TDS on an OTR screen is recorded with a CCD camera. At the VUV-FEL a TDS, named LOLA, has been installed in collaboration between Stanford Linear Accelerator Centre (SLAC) and DESY. The structure is 3.6 m long and operated at a frequency of 2.856 GHz with a nominal deflecting voltage of 20 MV. The OTR screen is mounted 10 m downstream from the TDS. Experimental data obtained with the LOLA system are shown in Figure 4.6.1. An excellent time resolution of 20 fs (rms) has been achieved **[4-97]**.

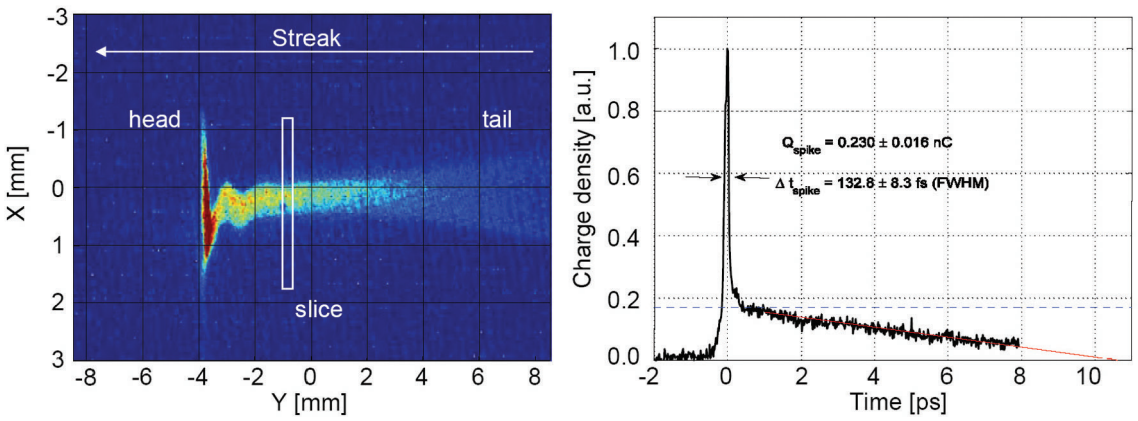

Figure 4.6.1 *Image of the beam streaked with the transverse deflecting structure. Strong distortions of the bunch due to collective effects are observed. Right: longitudinal charge profile with a peak current of 1.7 kA. By cutting the beam image into small slices, each representing a time slice of the bunch, the emittance, as a function of the longitudinal position in the bunch, can be determined.*

In the XFEL, TDSs will be in the electron-gun section and downstream of the bunch compressors. The deflecting field is chosen to provide a time resolution of better than 10% of the rms bunch duration. For dedicated studies, the resolution can be improved by increasing the betatron function at the RF structure.

Determination of slice-emittances

Ideally, the bunches in the linac should have the shape of an ellipsoid with the z-axis pointing along the flight direction. Coherent effects in the accelerator such as space-charge forces, CSR in the bunch compressor magnets or transverse wake fields in the superconducting cavities may lead to a longitudinal deformation, e.g. to a banana-like shape. In that case, conventional instruments for emittance measurement such as wire scanners or OTR screens equipped with CCD camera readout will yield larger values for the transverse emittance than for undeformed bunches. However, if one were able to subdivide the bunch longitudinally into thin slices, the emittance of any slice should be about the same as in the case of the undeformed bunch. The TDS offers a unique opportunity to determine these slice emittances.

For the emittance measurements a straight beamline comprising several FODO cells with a sufficiently large overall betatron phase advance, is installed between the TDS and the OTR imaging screen. When the quadrupole strengths are kept constant, the determination of the transverse phase-space parameters requires the imaging of the transverse particle density distribution at three (better four for redundancy) different OTR screens with a suitable betatron phase advance in between. A severe constraint is that OTR screens intercepting the electron beam are not possible, since the screen would be damaged by the long bunch train. Therefore, pulsed kicker magnets will be installed at suitable positions, which deflect the bunch to be analysed to off-axis OTR screens **[4-98]**. The slice emittance can then be measured as a function of the longitudinal position in the bunch for an arbitrary bunch in a long train. Measured results from the VUV-FEL are presented in **[4-99]**.

Energy-position correlation in the bunches

The TDS also enables the control and tuning of the bunch compression system performance. The streaked bunch is sent into a spectrometer which deflects the electrons in a direction perpendicular to the TDS deflection plane. The two-dimensional particle density distribution on an OTR screen in this dispersive section (the required dispersion is about 1 m) allows measurement of the average energy and the energy spread in each longitudinal slice.

Summarising, the TDS is a most powerful tool for determining the time profile of the bunches and the transverse emittance, the Twiss parameters and the local energy in any slice within the bunch. It must be emphasised, however, that the streaked one to ten bunches are lost for the generation of FEL radiation and must be dumped before the beam enters the main linac. Therefore, this diagnostic device does not allow monitoring of just those bunches which produce the FEL radiation, and it is also not suitable for generating the input signals for feedback systems.

4.6.3.2 Online longitudinal bunch diagnostics with electro-optic techniques

The electro-optic (EO) effect offers the possibility to resolve the time structure of the short electron bunches in a non-destructive manner. The principle is as follows: an EO crystal such as Zinc-Telluride (ZnTe) is mounted at a distance of a few millimetres from the electron beam. The large electric field co-propagating with an electron bunch induces a birefringence in the EO crystal. A linearly polarised optical laser beam acquires an elliptical polarisation when it crosses the birefringent crystal. This elliptical polarisation can be easily detected, for instance in a crossed-polariser setup.

In the electro-optic sampling (EOS) method, the time profile of the electron bunch is sampled by moving ultra-short Titanium-Sapphire laser pulses (typical duration < 20 fs FWHM) in small time steps across the bunch. The bunch shape is obtained from measurements of many bunches. Much more useful for beam diagnostics are single-shot measurements of individual bunches. This is possible in the spectral decoding scheme which is illustrated in Figure 4.6.2.

In this scheme, the Titanium-Sapphire (TiSa) laser pulse which typically contains the wavelength spectrum from 770 to 830 nm, is stretched (chirped) in a dispersive medium to a length of several picoseconds, larger than the electron bunch length. The chirp process is accompanied by a spectral ordering, the long wavelengths being at the head of the stretched pulse and the shorts ones at the tail. The chirped laser pulse overlaps the electron bunch in the ZnTe crystal and the induced birefringence at a given time slice of the bunch, is translated into an elliptical polarisation at the corresponding wavelength slice of the stretched laser pulse. Using a grating spectrometer and a suitable setup of crossed polarisers or quarter wave plates to detect the amount of ellipticity in each wavelength component, the time profile of the electron bunch can be reconstructed.

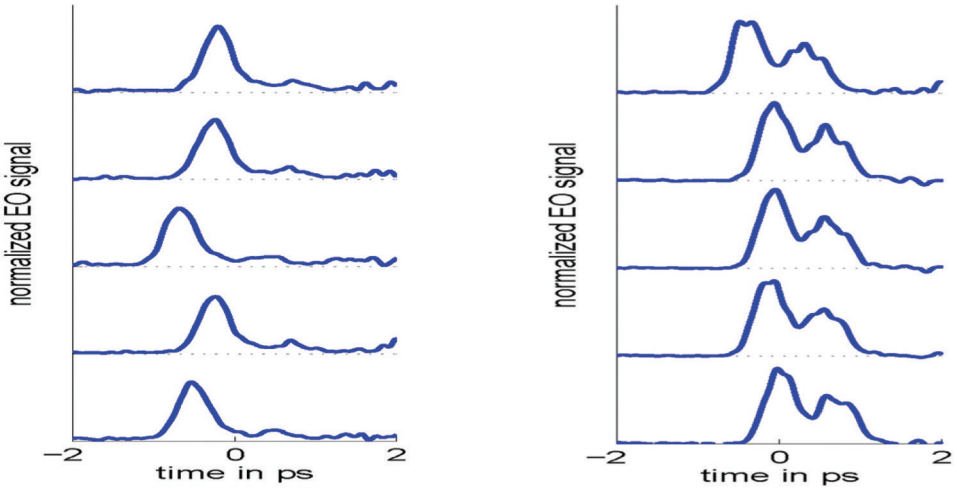

Figure 4.6.2 *Time profile of several bunches in the VUV-FEL linac, measured with the spectral decoding technique. Left: bunches with optimum longitudinal compression. Right: bunch shapes obtained with a different setting of the RF phase in the accelerating section preceding the magnetic bunch compressor.*

The measured time profiles of several bunches in the linac of the VUV-FEL are shown in Figure 4.6.3. The data from the VUV-FEL illustrate the usefulness of the spectral decoding setup. From the observed bunch shape one can easily judge whether the parameters of the bunch compression system are properly adjusted. Even in the case of optimum bunch compression, one can observe fluctuations in the bunch arrival-time at the EO crystal. The spectral-decoding EO setup is, thus, an excellent real-time monitor for the timing stability of the accelerator **[4-100]**.

Since the repetition rate of the pulsed laser can be precisely synchronised to the RF master oscillator of the machine (timing jitter of less than 20 fs is feasible), the single-shot techniques provide the possibility of determining the arrival-time of each electron bunch at the undulator with a precision of better than 30 fs. This will be of great interest for pump-and-probe experiments at the XFEL.

The intrinsic time resolution of the electro-optic method is limited by the frequency response of the EO crystals. In ZnTe the transverse optical (TO) lattice vibration frequency of 5.3 THz defines a lower limit for the resolvable bunch length of about 80 fs (rms). Of all known EO crystals, gallium phosphide GaP features the highest lattice vibration frequency (11 THz). GaP allows resolving bunch lengths down to 40 fs (rms). As shown above, the transverse deflecting cavity is superior in resolving the width of ultra-short electron bunches, however, it is not suitable for providing timing signals for all bunches in the FEL user operation **[4-101]**.

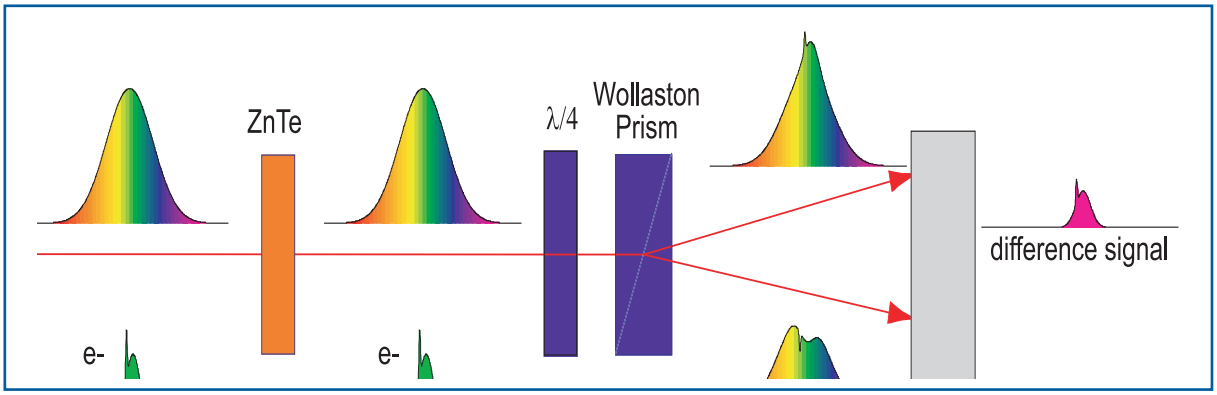

Figure 4.6.3 *The spectral decoding scheme for EO reconstruction of the longitudinal charge distribution in an electron bunch. At the top, the stretched linearly polarised TiSa laser pulse is shown. The long wavelength components are at the head of the pulse, the short wavelengths at the tail. The bottom shows the time profile of a typical electron bunch in the linac of the VUV-FEL. In the ZnTe crystal the local electric field at any slice of the bunch is imprinted as an elliptical polarisation onto the corresponding wavelength component of the laser pulse. The reconstruction of the bunch time profile is achieved by spectral analysis of the two polarisation states and subtraction of the two spectra. The spectra can be recorded with a gated intensified CCD camera (ICCD).*

To detect every bunch in a macro-pulse, a high-speed line camera with processing time of 200 ns is used. The profile information is pre-processed with a field programmable gate array (FPGA) and transferred to a longitudinal intra-pulse-train feedback. Monitoring the longitudinal bunch profile with electro-optic methods is foreseen at the injector (8.5 ps rms) and after the first bunch compressor stage (300 fs rms). After the final compression stage, with 60 fs rms bunch length, the EO technique is at the limit of its resolution.

4.6.3.3 Energy spread monitoring

Synchrotron radiation monitors, that image incoherent synchrotron radiation emitted by dipole magnets and insertion devices, are commonly used in storage rings to monitor the beam profile. In certain dispersive sections of the XFEL, like the bunch compressor or the dump-lines, the transverse beam profile is dominated by the energy spread of the beam. This makes synchrotron radiation monitors excellent candidates for non-destructive measurement of the beam energy and the energy distribution. Planned high precision synchrotron radiation monitors, equipped with fast readout system (line cameras), are listed in Table 4.6.2.

		Injector	BC1	BC2	Collimator	Dump
Energy	GeV	0.1	0.5	2.0	17.5	17.5
rms Resolution		3.0×10^{-4}	1.7×10^{-4}	1.6×10^{-4}	2.4×10^{-4}	2.4×10^{-5}
Dispersion	m	0.67	0.68	0.33	0.05	0.5
Beta-function	m	8	13	11	2	2
Betatron-component of beam size	µm	200	115	53	12	12

Table 4.6.2 *List of synchrotron radiation monitors to determine the beam energy spread with the capability to record individual bunches in long pulse trains. The rms resolution for the energy profiling is determined by the betatron component (the beam size of a beam with no energy spread) of the transverse beam size.*

To measure the residual energy spread of the beam, OTR screens and special imaging optics are foreseen for use in the commissioning dump-lines, the injector, BC1 and BC2 since these locations provide large dispersion with small beta-function.

4.7 Technical layout

4.7.1 Warm vacuum systems

The warm vacuum systems of the XFEL consist of four major parts: the injector, bunch compressors (1 and 2), the undulator sections and several beam transport lines which are part of the beam distribution system. An overview of the key aspects of these individual sections is given in Table 4.7.1.

Section	Length	Issues
Injector I	60 m	RF-guns, dust free, high complexity
Compressors, diagnostic	160 m	Flat steel chambers, Copper coating, narrow tolerances
Collimator section	209 m	Precision collimator units, material: Ti
Undulator chambers	713 m	Small aperture, low roughness, high conductivity
Beam distribution (e-)	1.737 m	Optimised for cost, low complexity, Copper pipes

Table 4.7.1 *Overview of warm vacuum sections.*

The requirements for the beam vacuum quality in the XFEL are relaxed as compared to the requirements in a storage ring. Effects which are potentially harmful for the beam include Bremsstrahlung interaction and resulting beam loss, emittance growth from elastic scattering and the fast ion instability which leads to an amplification of orbit deviations along the bunch train.

The fast ion instability is only of importance if the ions generated by one bunch stay long enough in the vicinity of the beam centre to interact with the next bunch. This leads to a threshold condition for the instability which is independent of the residual gas pressure but depends on the bunch distance and the ion mass of the gas molecules **[4-102]**. For XFEL parameters, only ions with masses beyond M≈100 can be captured by the beam.

Such heavy gas species do not occur at relevant partial pressures in accelerator vacuum systems.

The typical gas composition consists of 80% H_2 and 20% CO. Since the contribution of Hydrogen is negligible, the Bremsstrahlung scattering rate is roughly estimated using the radiation length of Carbon monoxide, which is X_0=320 m under normal conditions. Consequently, at a partial pressure of $P_{CO}=10^{-8}$ mbar, the radiation length is 3×10^{13} m and for a single passage of a 2 km drift length, the fraction of relative beam loss would be below 10^{-10}. This is less than a single electron from each bunch. Given this low interaction rate, one may already argue that the contribution of gas scattering to the emittance growth is small as well. Indeed, even in the first warm low energy section with E_{beam}=120 MeV, where the beam is most sensitive, the relative emittance growth amounts to 5×10^{-5}, or emittance doubling would occur only after 600 km drift. On the other hand the above quoted pressure can be achieved easily, at least in the radiation-free transport lines.

4.7.1.1 Injector and bunch compressor

The RF gun is made from OFHC Copper with very high surface quality requirements. Another critical aspect is the water cooling distribution to keep the spatial temperature distribution within the required tolerances. To obtain a good lifespan from the sensitive cathode, the residual gas pressure has to be kept in the range of 10^{-10} mbar. A long-term experience exists at DESY concerning the production of L-band RF guns.

The vacuum chambers in the bunch compressors should exhibit a flat aperture to allow for horizontally varying beam orbits. To obtain the necessary mechanical stability while keeping a reasonable gap height of the dipole magnets, the best choice for the chamber material is stainless steel. The inner surface of the vacuum chambers will be coated with a thin Copper layer to minimise the resistive wall wake field effect. The chambers will be produced from two milled halves which are welded together by laser beam welding, a method which has been established during the production of the bunch compressor chambers for the VUV-FEL. A significant technical challenge is presented by the need to keep sub-millimetre tolerances for the straightness of these chambers with a length of several metres during the welding process.

4.7.1.2 Collimation section

The major part of the collimation section consists of a beam transport line which will be equipped with Copper tubes and ion getter pumps similar to the beam distribution system. The section contains four collimator units with a tapered round fixed aperture and Titanium blocks as the collimator material. The collimator units will exhibit a similar design to the ones presently in operation at the FLASH (VUV-FEL) (see Figure 4.7.1). There will be a possibility of interchanging up to three different apertures using the appropriate mechanics. Technical measures which allow for precise alignment of the collimator units are of special importance.

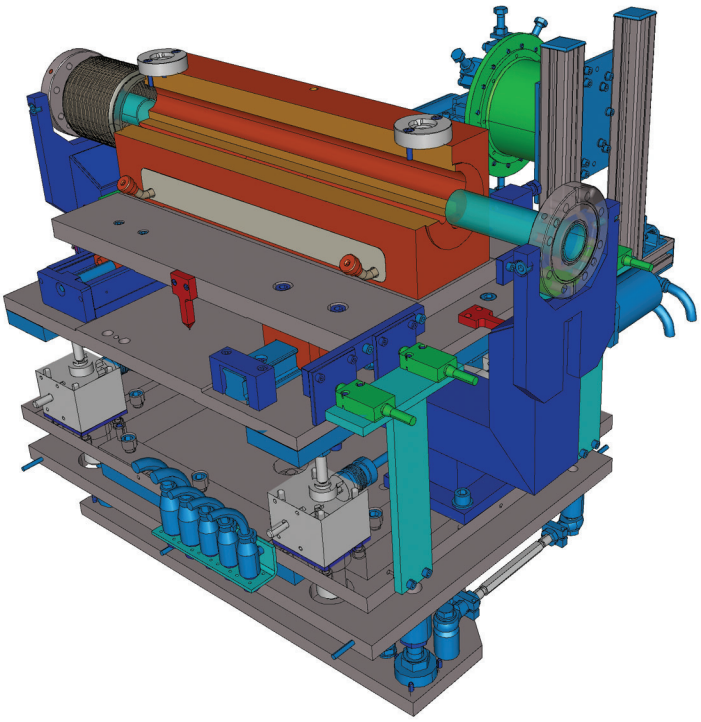

Figure 4.7.1 *Cut-away view of the collimator unit presently under operation at the VUV-FEL. The cylindrical part in the centre of the figure contains several tapered circular apertures which can be moved to the beam orbit. The collimator units for the XFEL will closely follow this design, except for different dimensions and choice of material.*

4.7.1.3 Beam distribution system

Roughly 1.7 km of cost-optimised vacuum system for beam distribution has to be built. To limit the resistive wake field effects the vacuum chambers will be produced from Copper with stainless steel flanges. Copper pipes are less expensive than Copper coated steel tubes which present an alternative. An inner diameter of 50 mm has been chosen. The system will be pumped by ion getter pumps with a pumping speed of 60 l/s in a distance of 6 m. In this configuration an average pressure of 5×10^{-9} mbar will be achieved. The power supplies for the getter pumps will be installed in the tunnel.

4.7.1.4 Undulator vacuum

Naturally, the vacuum chamber inside the undulator magnets exhibits a tight aperture. An important design criterion is a small wall thickness in the vertical direction to maximise the beam aperture while keeping an adequate magnet gap height for maximum field strength. Since there is more space available in the horizontal direction, an elliptical shape has been chosen for the chamber geometry. The wider horizontal dimension helps to reduce the amount of spontaneous radiation which is absorbed by the inner chamber walls. The baseline design assumes an elliptical steel tube for the chamber body and two Copper profiles with a water cooling channel which are brazed to both sides of the elliptical profile. The total heating power on the inner wall of the vacuum chamber is dominated by HOM losses and amounts to 2 W/m.

The typical opening angle of the spontaneous radiation is $1/\gamma$ in the vertical plane and K/γ horizontally. For example, at 20 GeV this amounts to 25 µrad and 150 µrad for the two planes[5] . It is proposed to protect the beam-pipe from radiation by absorbers which are installed in between the undulator units. With the chosen geometry, shadow angles of 70 µrad and 500 µrad can be achieved. Although the major part of the photons will hit the absorbers there is still a significant fraction in the low energy part of the spectrum with emission angles large enough to reach the beam-pipe. For example, 25% of the photons are radiated at angles beyond $3/\gamma$. Photon induced outgassing occurs for photon energies above ~10 eV which is a small fraction of the critical energy.

The baseline dimensions of the chamber are shown in Figure 4.7.2, including the cross-section of the absorber for spontaneous radiation, which is located in-between two undulators.

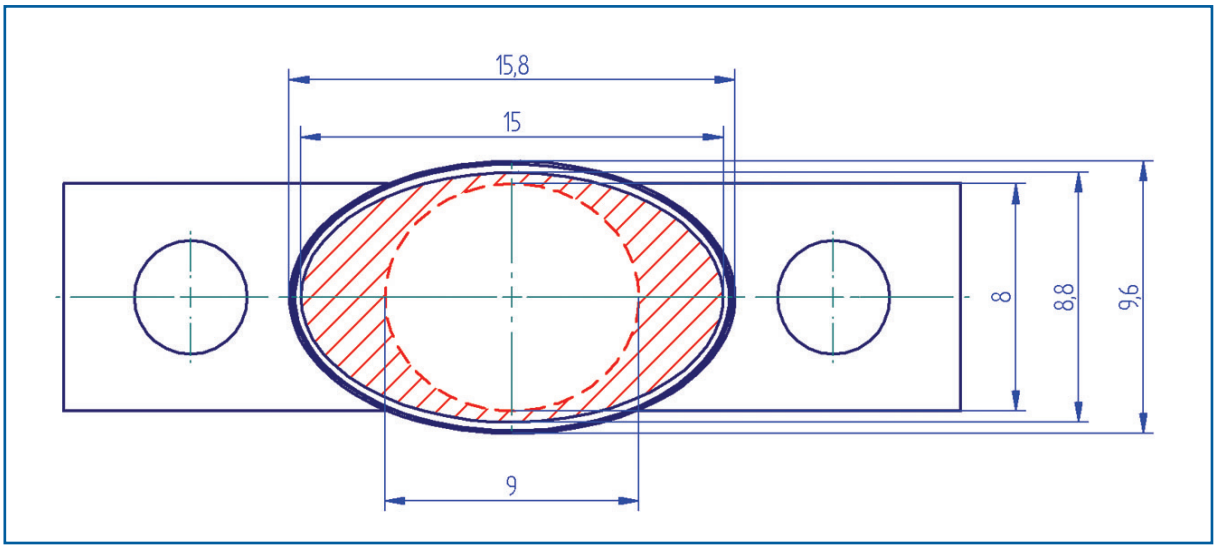

Figure 4.7.2 *Cross-section of the undulator beampipe with inner and outer dimensions. The aperture of the radiation absorber is shown as the dashed line.*

To minimise resistive wake field effects, the chamber body will be coated with a Copper or Gold layer. The roughness of the chamber surface should not exceed an rms value of ~300 nm over a wavelength of 1 mm. It has been demonstrated that such values can be achieved in electropolished steel tubes as well as in carefully extruded aluminum tubes.

At the maximum beam energy of 25 GeV, the spontaneous radiation reaches an average level of 8 W/m (beam current 12 µA). Over the length of one undulator unit this amounts to 40 W which will be absorbed by Copper absorbers. The absorbers are also required for shadowing the beam pipe; thereby reducing the photon induced outgassing. The rate of photons produced per unit length in the undulator at 300 kW beam power and a peak field of 1.3 T is 4×10^{14} $m^{-1}s^{-1}$. Assuming that 5% of these photons hit the beam pipe as residual radiation, that leads to an initial radiation-induced outgassing rate of 2×10^{-11} mbar l/s cm^2 for steel. In comparison, the thermal outgassing rate without radiation is approximately

[5] The largest K=6 of the SASE 2 undulator has been assumed.

5×10^{-12} mbar l/s cm^2. The vacuum conductance of the narrow pipe is small and amounts to c=0.17 l/s (N2) for one metre length. From this conductance and the volume of the pipe per unit length, a diffusion coefficient of 1.7 m^2/s can be computed. The typical relaxation time of pressure bursts in the chamber can be estimated as the diffusion time from the middle of the chamber to the pump. It amounts to 5 seconds. This time is much longer than the repetition time of the bunch trains. Consequently, the pulsed operation of the accelerator will result only in a moderate modulation of the pressure around the average pressure determined from the static diffusion model. The system will be pumped by ion getter pumps installed in the 1.1 m long section between the undulator units. The resulting pressure is dominated by the limited conductance. With the above outgassing rates, an average pressure of 2×10^{-7} mbar is expected for stainless steel. According to the above introductory remarks such relatively high pressures are still very acceptable.

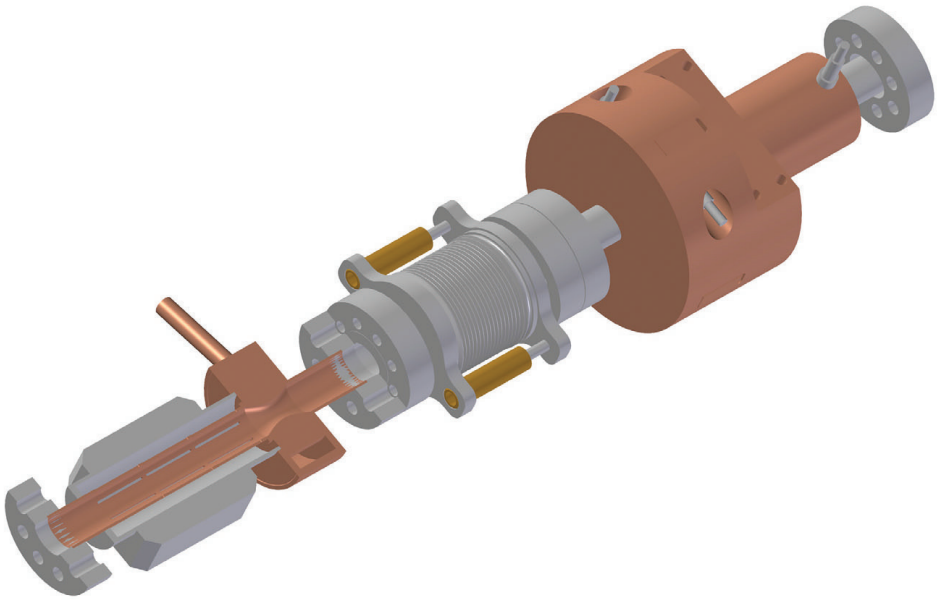

Figure 4.7.3 *Intersection beam-pipe between undulators showing RF-shield and pump connection, absorber, bellows unit and cavity BPM (from left).*

4.7.2 Magnets

The parameters of the warm dipole and quadrupole magnets are summarised in Tables 4.7.2 and Table 4.7.3 **[4-103]**. Around 60 dipole magnets are used in the bunch compressors, collimation, beam distribution and beam dumps. About 400 quadrupole magnets focus the beam. Subsequent corrector magnets will steer the beam when necessary. The dispersive sections also require about 40 sextupoles and octupoles for higher order corrections. The heavy dipole and quadrupole magnets located in the dump region fit in the maximal geometrical region of 900 mm × 600 mm horizontal and vertical to the beam axis. All other magnets have smaller geometrical size. The dipoles have gap heights of 12 mm, 40 mm, 60 mm and 100 mm respectively, and are of C-type and H-type

shape. Quadrupole and higher order multipole magnets are characterised by standard aperture (diameter) of 12 mm, 40 mm, 60 mm and 100 mm. Magnet yokes do not exceed a length of 5 m to make handling in the tunnel easier.

The magnets will be made of 1 mm laminated steel sheet metal. To minimise the tooling costs, a modular construction system will be worked out for the different types of dipole magnets and quadrupole magnets.

All dipole and quadrupole magnets will have water-cooled Copper coils whereas the correction magnets have air-cooled Copper coils.

Name	Count	Length m	Gap m	B_{max} T	Current A	Power losses kW	Total weight kg	Water flow rate l/min	Water over heating °C
BA	4	0.3	0.04	0.667	480	2.6	260	1.3	28
BI	6	0.5	0.04	0.31	670	1.9	280	2.1	<15
BF	1	1.0	0.04	0.931	440	8.8	1800	9.1	24
BG	1	2.5	0.04	1.397	660	39.9	4500	19.2	30
BB	4	0.3	0.04	1.268	900	9.2	450	3.7	36
BC	8	5.0	0.06	0.088	120	0.8	5550	0.4	31
BE	6	2.5	0.06	0.730	450	15.4	8450	6.1	37
BD	8	4.0	0.06	0.417	540	20	4100	11.4	24
BV/BW	14	2.5	0.06	1.456	890	71.4	8450	31.1	33
BX	8	0.5	0.1	0.384	690	10.8	515	7.3	21

Table 4.7.2 *Main parameters of dipoles.*

Name	Count	Length m	Bore radius m	B_{pole} T	Current A	Power losses kW	Total weight kg	Water flow rate l/min	Water over heating °C
QI	28	0.25	0.02	0.05	5	0.04	35	air cooled	
QA	135	0.2	0.006	0.15	40	0.05	25	0.8	<5
QB	53	0.5	0.02	0.40	170	1.9	150	1.32	20
QC	27	0.3	0.02	0.14	60	0.16	90	0.57	<5
QD	17	0.3	0.02	0.40	170	1.3	90	0.57	33
QE/QF	76/47	1.0/0.5	0.03	1.00	390	18/10.8	1300/600	6.3/7.8	40/20
QG	6	3.0	0.05	1.11	960	77	6500	44.5	35
SEXT	36	0.45	0.03	0.84	450	20.6	500	7.05	39
OCT	6	0.4	0.03	0.47	90	2.42	740	1.6	22

Table 4.7.3 *Main parameters of multipoles.*

4.7.3 Kickers

Table 4.7.4 gives the parameters for the kicker elements used in the beam distribution system. The kicker magnets are striplines surrounding a sputtered ceramic vacuum chamber. Magnet lengths of between 0.3 and 1 m are foreseen.

		Fast single bunch kicker (for beam dump)	Flat-top kicker (for beam distribution)
Pulse Form		Burst	Flat top
Repetition Rate	Hz	5×10^{6}	10
Max. Pulse Width	s	200×10^{-9}	300×10^{-6}
Rise/Fall Time	s	$< 100\times10^{-9}$	$\approx20\times10^{-6}$
Rel. Amplitude Stability		0.01	5×10^{-5}
Relative Residual Ripple		5×10^{-5}	5×10^{-5}
Max. int. Field Strength	mT m	31	31
Number of Kickers		30	10
Pulser Voltage	kV	8	0.3
Pulse Current	A	100	300
Max. Power	kW	40	0.27
Average Power	W	260	270

Table 4.7.4 *Parameters for the beam distribution system kicker elements.*

The fast pulser prototype is based on Behlke HTS 80-12-UF switches operated in parallel to allow for 5 MHz switching rate. The on/off time of these switches is in the order of 10 ns. Relative amplitude stability of below 0.5% has been measured at TTF for a single switch, while the first 5 MHz prototype shows an amplitude stability of about 3%. Further research and development (R&D) work is planned to improve this below 1%.

The flat-top pulser is based on a capacitor discharge pulser. The accuracy is reached by dividing it into several kicker/pulser systems (say 10), where nine kickers provide most of the amplitude and the tenth is used together with a programmable power supply to correct for the unavoidable systematic voltage drop.

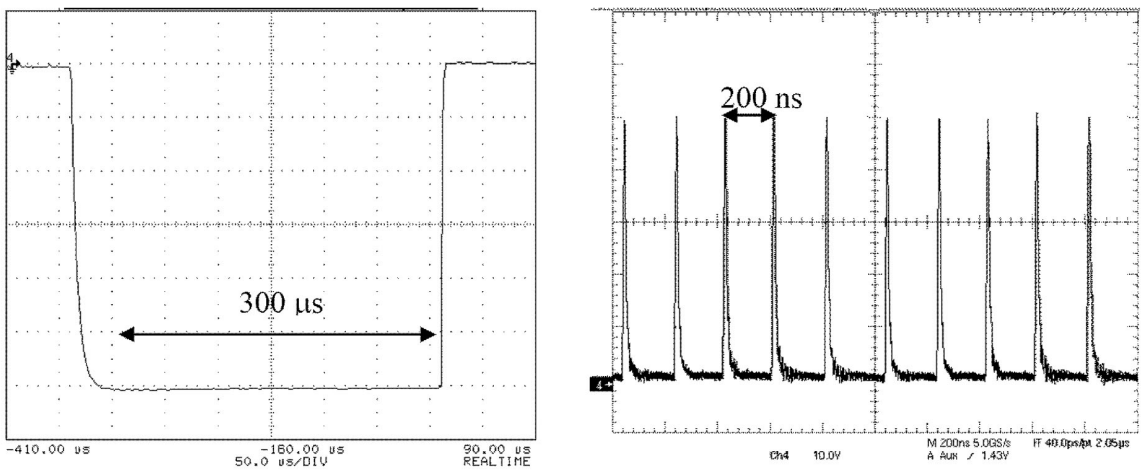

Figure 4.7.4 *Left: Pulse current of the flat-top kicker with an amplitude stability of better than 1% over a pulse length of 300 µs. The fall-time is only 5 µs. Right: Pulse form of 5 MHz single-bunch kicker.*

4.7.4 Beam dumps

4.7.4.1 Requirements and general layout

In Phase 1 of the XFEL project, the beam can be dumped at three positions downstream of the linac. These main dumps all have the same capabilities as specified by the limits given in Table 4.7.5.

The average power per dump is limited to 300 kW. This allows an operation at the nominal beam parameters (20 GeV, 1500 bunches with 1 nC per beamline, 10 Hz repetition rate). The power limit was chosen so that a solid graphite-based absorber can be used. This approach avoids the complexity and risks of using a liquid (e.g. water) dump system.

E_0, electron energy	max. 25	GeV
N_t, number of electrons per bunch train	max. $2.5 \cdot 10^{13}$ ⇔	4µC
I_{ave}, average beam current	max. 40	µA
W_t, energy carried in one bunch train	max. 100	kJ
P_{ave}, average beam power	max. 300	kW

Table 4.7.5 *Parameters of the beam hitting the dump in XSDU1, XSDU2 and XS1.*

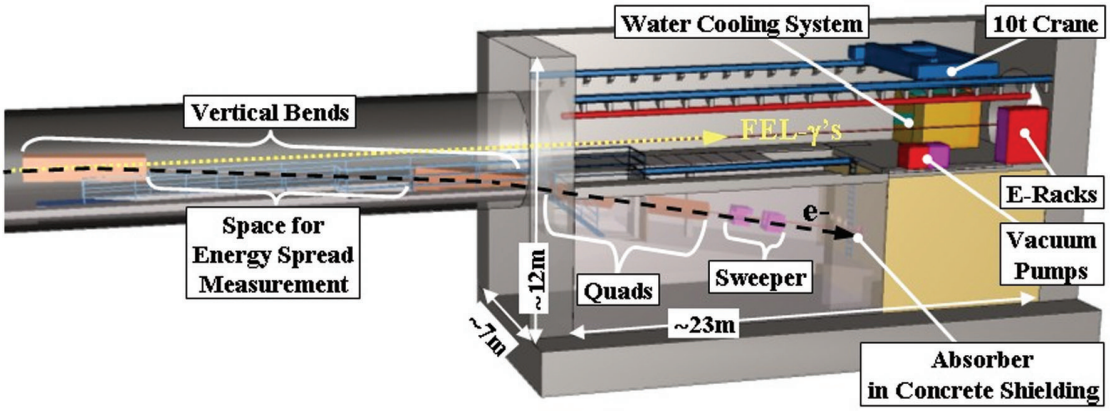

Figure 4.7.5 *The main beam dump system in the underground dump building XSDU1.*

Two of the main beam dumps are housed in dedicated buildings (XSDU1 and XSDU2) downstream of the last undulator. During regular FEL operation the electron beam is aborted here after being separated from the FEL photon beams. The third main dump system is implemented at the end of the linac tunnel in the separation building (XS1). This dump will be used during commissioning and in emergency cases. In regular FEL operation mode, this dump takes those bunches which are removed in the process of creating different bunch patterns.

As an example for the overall layout of the dump system, Figure 4.7.5 gives a 3-D sketch of the situation in one of the underground dump buildings (XSDU1). After a 10° vertical bend (15° in XS1) the electron beam is directed onto the absorber. The deflection is provided by a double-bend achromat. On its way two quadrupoles magnify the beam spot size by a factor of 100 up to $\sigma \geq 2$ mm. An issue is the alignment and orbit tolerance of about 0.5 mm in the strong quadrupoles. A slow deflection system (slow-sweeper) distributes the beam bunch train by bunch train (not bunch-by-bunch) circularly with a sweep radius of R_s=5 cm at the dump face. Both measures are required for a safe operation in terms of absorber heating, as will be explained in the next section. Before finally entering the absorber, the beam passes through a beam window which separates the beamline vacuum from the low quality vacuum in the absorber section. A second window gives redundancy and as indicated in Figure 4.7.6 offers the possibility of using the intermediate volume for beam profile monitoring by means of gas luminescence.

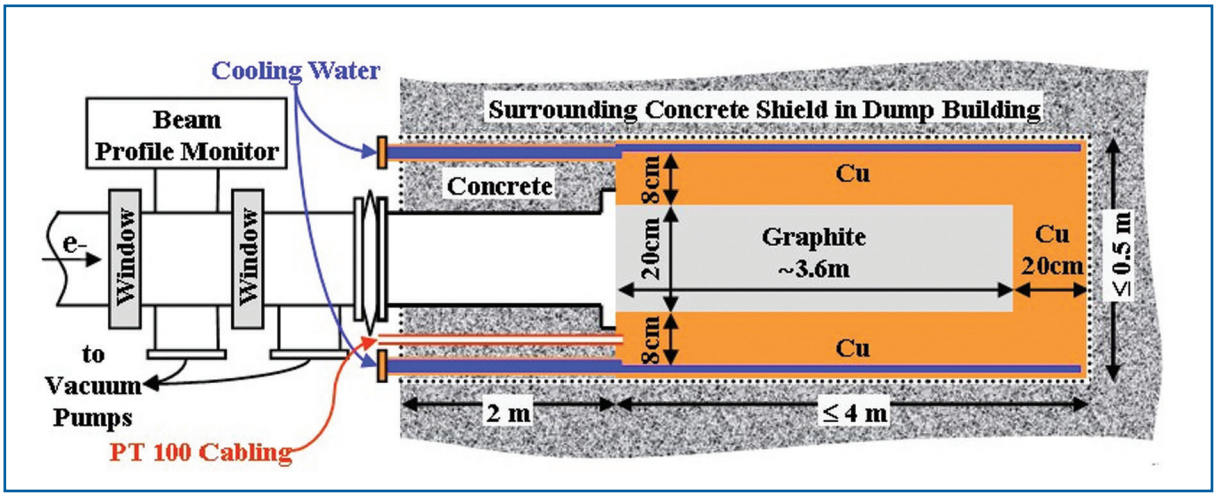

Figure 4.7.6 *Layout of the dump module (marked by dotted line) installed in a hole of the surrounding concrete shielding and connected via two windows to the beamline.*

4.7.4.2 Description of components

The cylindrical absorber has a core of 20 cm in diameter, consisting of a 3.6 m ($14.4 \times x_{0,C}$) long graphite section (density 1.7 g/cm^3), which is followed by a 20 cm ($13.8 \times x_{0,Cu}$) long Copper tail catcher. The absorption length x_0 depends on the material and is, in our case, $x_{0,C}$ = 25 cm for graphite and $x_{0,Cu}$ = 1.4 cm for Copper. Radially this core is surrounded by a layer of 8 cm (5 Molière radii) Copper, which is water-cooled at its circumference and simultaneously serves as a vacuum tight enclosure for the graphite. Less than 1% of the energy of a 25 GeV beam leaks from such an absorber and more than 90% of it is absorbed in the graphite section **[4-104]**.

The largest power dissipation occurs at the shower maximum at a depth of ~1.2 m (25 GeV) and ~0.9 m (7.5 GeV). At P_{ave}=300 kW peak power densities of about 1.6 kW/cm at 25 GeV and even 1.8 kW/cm at 7.5 GeV are expected, since the shower is shorter in the latter case. By means of slow circular beam sweeping with a radius of 5 cm, the resulting maximum equilibrium temperature in the graphite (due to heat extraction by radial thermal conduction towards the water-cooled circumference) is kept just below 500°C to 600°C, where graphite tends to oxidise at normal atmospheric conditions. For additional safety and redundancy the graphite is kept under low quality vacuum. Nevertheless, it has to be emphasised that a good ($\leq$ 0.5 W/cm^2/K) and long term reliable thermal contact at the radial graphite to Copper boundary plays a vital role for heat extraction. Therefore, brazed connections are aimed for.

Since the sweeping is slow compared to the $\leq$ 1 ms passage time of one bunch train, it does not affect the instantaneous heating produced during the absorption of one train. Thus, for safe operation the impinging beam size has to be kept at $\sigma \geq 2$ mm. In that case the maximum instantaneous temperature jump in graphite is less than 200 K and the dump can withstand the related cyclic mechanical stresses over the long-term (operation period of the XFEL).

For shielding reasons the absorber is placed 2 m deep in a dead-end hole in the surrounding concrete shield, which is part of the building. Therefore, the beam tube, water pipes and temperature sensor cabling need to be extended 2 m in the upstream direction with the intermediate space filled with concrete. With overall dimensions of 6 m in length, 50 cm in diameter and a mass of about 5 t, the front part together with the absorber form the dump module. This unit has to be handled as one part during installation and exchange.

The beam windows need a useful diameter of 200 mm. Each of them is made of a 10 to 15 mm ($<<x_0$) thick graphite (x_0=25 cm) disk, which is brazed into a water-cooled Copper frame, which again is brazed to short stainless steel tubes, to which the flange can be welded. The graphite disk has excellent thermal and mechanical properties to withstand the cyclic load induced by the beam and the static load, which is present when one of the adjacent vacuum sections is vented to 1 atm while the other is still pumped. One face of the window will be coated by a thin (~30-50 µm) layer of a suitable material (e.g. pyrolytic graphite) to make the porous graphite window leak tight and its surface suitable to be installed in a particle-free UHV system. Since tests on different window coatings are presently underway, a final choice on the most appropriate coating material has not been made yet. The power dissipation in the window is much less than that in the absorber. Therefore, it does not raise an additional limitation on the incoming beam. A full bunch train (4 µC) with a spot size of σ = 2 mm causes an instantaneous temperature rise of only 30 K in the graphite of the window. The average temperature drop, which builds up between the window centre and its cooled circumference at a radius of 10 cm, is again only 30 K when 40 µA of average beam current is homogeneously penetrating along a radius of 3 cm (size of the sweep at the window 2 m upstream of the absorber face).

The cooling water of the edge-cooled absorber takes less than 10^{-3} of the primary beam power. Therefore, radiolysis is negligible and activation is a minor problem, but demands a separate cooling circuit of conventional type. This circuit requires a space of about 8 $m^2 \times 2$ m (height) and is placed in the dump building next to the outgoing photon tunnel as shown in Figure 4.7.5. The total amount of water in the circuit is not more than 2 m^3. In case of accidental leakage, water flows passively into a container located at the deepest point of the building. After one year of operation (5,000 h) at 300 kW, the activity concentration in the cooling water stays within the legal limits to be drained, except for very short-lived nuclei and the ^{7}Be ($t_{1/2}$=53 days) content **[4-105]**. Fortunately not much of the ^{7}Be will stay dissolved in the water. Some fraction will attach to the inner surfaces of the cooling circuit and most of it will accumulate in the ion exchanger, where it, treated as a point source, creates a very moderate dose rate of ~2 µSv/h in a 1 m distance without any shielding. Thus, negligible ^{7}Be content is expected in the cooling water and the water can be exchanged without problems during regular annual maintenance as required technically, in any case, to retain its quality. Nevertheless, if activity measurements require, the water would be stored for some time to allow for decay.

The activation of soil and ground water close to the dump building will be kept below 10% (DESY planning goal) of the legal limits, if the dump module is shielded by an equivalent 4 m (including the building walls) of normal concrete **[4-105]**. An additional 5.5 m thick layer of sand, between the building wall and the surface above, results in a publicly

accessible area (≤ 0.1mSv/a) there. The dose rate in the downstream photon tunnels and the experimental hall due to escaping muons from the dump is limited by the depth of the dump position and its downward tilted axis. The activity concentration of the tunnel air is tolerable at the outlet above ground, if the air, which resides in gaps within the first 2 m of the concrete shield around the dump is trapped, i.e. cannot couple to the air flow of the vented tunnel. That is why the concrete block, which houses one hole for the dump module in operation and three holes for storing activated faulty ones, is made out of one piece. Nevertheless, where the beam pipe of 200 mm diameter (required by the slow sweep) penetrates the shield, neutrons can go out unshielded. They will activate upstream components and the ambient air as well. Hence, almost the complete ramp area in the dump building is enclosed by a wall and a demountable concrete floor to keep the highly activated air trapped. Access to this area is possible after radiation permit (decay time) and forced ventilation. Exchange of a dump module is expected to be carried out remotely without the necessity to work close to the dump module or the upstream beamline, which has to be removed before the dump module can be pulled out and put into one of the storage holes.

4.7.4.3 Remarks on the dump for the injector

The dump for the injector will be designed for $E_0 \leq 300$ MeV, $P_{ave} \leq 12$ kW, $I_{ave} \leq 40$ µA and $N_t \leq 2.5 \times 10^{13}$. A similar layout as presented for the main dump can be chosen. The length of the absorber would be adjusted to about 1.2 m to match with the lower energy. The graphite core can be reduced to a diameter of about 100 mm, since slow sweeping is not required at these power levels. The spot size limit for a full bunch train (2.5×10^{13} e^-) is about $\sigma \geq 1$ mm and fast (intra-bunch train) sweeping may be used, if the beam cannot be sufficiently defocused by optics. A tilted window, coated with an OTR reflecting material, is proposed to integrate a beam profile measurement. This approach may also be used for the main dump, but the required useful aperture of 200 mm is already quite large in that case. Due to the tilt, the actual window size will even exceed this value and the design effort is more challenging with respect to mechanical strength, dissipated power and operating temperatures. Nevertheless, the OTR option will be considered as well for the main dump systems.

4.8 Synchronisation system for the XFEL

4.8.1 Introduction

Studies of ultra-fast systems, with changes occurring on a timescale of less than 100 fs, are typically carried out with pump-probe laser experiments. Time-dependent phenomena are stimulated by a high-power pump-pulse, for example, with an ultra-fast optical laser or a laser-driven source, and then probed after a defined time delay. By repeating the experiment for different delays, the system changes can be recorded and the underlying dynamics understood. These sorts of experiments require a high level of synchronisation and information about the arrival-time of the pulses.

In the standard setup, shown in Figure 4.8.1, the pump and the probe beam have a common source, so that precise time-delays can be produced with optical path-length differences.

The time-resolution can be as short as a fraction of a femtosecond and is limited only by the overlap of the pump and the probe pulses **[4-106, 4-107]**.

The situation is different for FELs due to the fact that high-energy, high-charge electron beams serve as the driver for the FEL lasing process, and thus, the probe x-ray source is entirely distinct from the optical pump laser source located in the experimental area.

Synchronisation of the electron beam arrival to the arrival of the optical laser pulse with femtosecond precision is highly difficult. Generally, knowledge of the time-difference between the x-ray pulse and the optical laser pulse is sufficient to do pump-probe experiments.

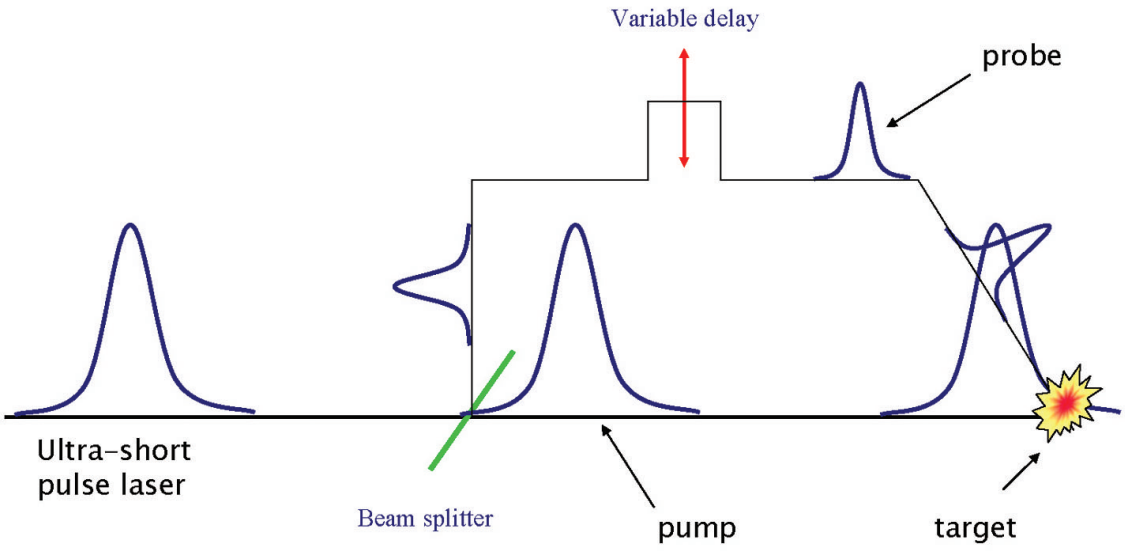

Figure 4.8.1 *Layout of a pump-probe experiment using a common source for a pump and probe beam.*

Post-sorting of experimental data according to the difference in the beam arrival-times has been demonstrated at the Sub-Picosecond Pulse Source (SPPS). The electron bunch arrival-time with respect to the optical laser was determined with an electro-optical technique that required transport of the 800 nm short-pulse optical laser over a distance of 150 m **[4-108, 4-109]**. An accuracy of 20-40 fs rms was achieved.

Because the incoherent undulator radiation produced at SPPS is a direct map of the longitudinal beam profile, the measurement of the x-ray pulse arrival-time is limited by the accuracy with which the electron bunch arrival can be determined. For FELs, this is not necessarily the case, because, often, only a small fraction of the bunch will lase. If this fraction is not always the same, then the post-sorting loses accuracy. For a 60 fs rms bunch-duration, a variation of the lasing region by as much as 25 percent, as for example,

in the case of a time-varying transverse-longitudinal tilt, the post-sorting resolution is not better than 15 fs.

Ideally, one would like to measure the arrival-time of the x-ray laser pulse and not just of the electron beam. This requires a geometrical time-sweep technique in which the pump and probe lasers are crossed on a tilted surface or within an interaction volume, so that the timing information is available in the spatial-domain **[4-110, 4-111]**. This technique is, so far, limited by the spatial resolution of the read-out system, which is on the order of 20-40 fs rms (see Section 6.2.2).

4.8.1.1 Electron beam stabilisation and arrival-time

The reliable and stable production of x-ray laser beams with pulse-durations less than 100 fs imposes completely new demands on the synchronisation system for the accelerator and its sub-systems. Phase and amplitude errors of the accelerator RF can cause undesired fluctuations of the electron beam peak-current, change the slice-emittance within the electron bunch, and introduce variation in the arrival-time of the beam at the undulator.

The demanding tolerances on the RF regulation are related to the longitudinal electron beam compression process. The compression is needed because state-of-the-art electron beam sources, RF-photoinjectors, are optimised for the tight requirements on the transverse emittance. The peak current of the RF-photoinjector is, therefore, limited to about 50 A. The beam is longitudinally compressed by introducing an energy-chirp, through off-crest acceleration, into a bunch and then passed through a magnetic chicane. The energy-dependent path-length in the chicane causes a linear shearing of the longitudinal phase-space yielding a shorter bunch at the chicane exit. To achieve 5 kA peak-current, the overall compression-factor, C, must amount to 100 for the XFEL. A deviation of 0.1% in the initial beam energy chirp, however, changes the peak-current at the exit of the last chicane by 10%.

The electron beam arrival-time at the undulator is primarily determined by the time the beam exits the first electron bunch compressor. The time can be approximated by[6]:

$$\Sigma_t^2 \approx \left(\frac{R_{56}}{c_0}\frac{\sigma_A}{A}\right)^2 + \left(\frac{C-1}{C}\right)^2 \left(\frac{\sigma_\phi}{c_0 k_{rf}}\right)^2 + \left(\frac{1}{C}\right)^2 \Sigma_{i,t}^2$$

where R56 = 0.1 m is the momentum compaction of the first chicane BC1, k_{rf} = 27.2 m^{-1} is the RF wave number, σ_A and σ_Φ are rms amplitude and phase jitter of the acceleration section prior to BC1, and c_0 is the speed of light. $\Sigma_{t,i}$ denotes the incoming beam arrival-time which is significantly compressed (C>>1).

[6] The contribution of the third harmonic cavity to linearise the longitudinal phase-space is neglected.

A small amplitude deviation of 0.01% of the acceleration field already causes a timing jitter of 33 fs at the undulator. A correlated phase variation of 0.01°, due to a phase change of the local oscillator for the RF down-converter, changes the arrival-time by 21 fs. Electron beam arrival-time stability in the order of a few femtoseconds will, therefore, be extremely difficult, if not impossible to achieve with present day technology of the low-level RF cavity regulation. Furthermore, this example shows that the major challenge of the synchronisation for the XFEL is the large distance of more than 3 km between two of the most critical timing devices: the booster acceleration-section and the pump-probe laser system.

Figure 4.8.2 shows the measured arrival-time stability of the electron beam at the VUV-FEL **[4-112]**. The observed timing-jitter of about 200 fs rms is consistent with the observed amplitude-jitter of the first RF acceleration section and a sensitivity of about 5 ps per percent amplitude variation.

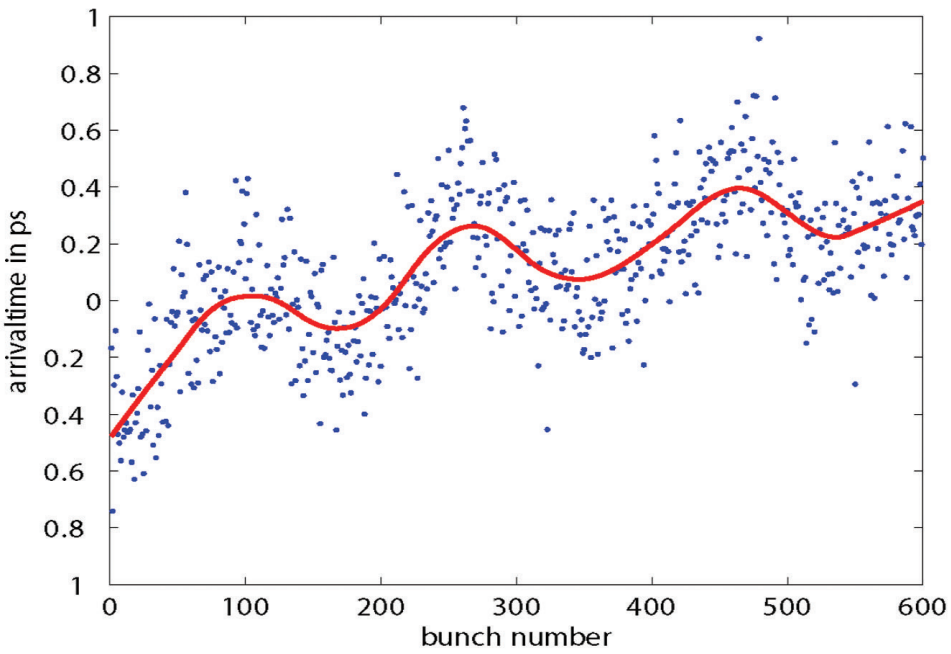

Figure 4.8.2 *Timing jitter of the electron beam at the exit of VUV-FEL acceleration linac determined by an electro-optic setup. The rms jitter over five minutes amount to 270 fs, and to 200 fs when the slow drift is removed* **[4-112]**.

4.8.1.2 Sub-femtosecond synchronisation

In the previous section, the difficulties of synchronising the electron bunch and an external reference that serves as a clock for pump-probe lasers has been discussed. To go beyond the limitations of RF system stability, the charge distribution of the electron bunch should not be the relevant carrier of the timing information. This can be achieved with electron-beam manipulation lasers acting on a longitudinally defined sub-ensemble of the electron beam. If the electron beam manipulation occurs downstream of the last bunch-compressor section, then the synchronisation problem is reduced to the locking of the manipulation and the pump laser to one another.

One possibility proposed for the XFEL, based on the use of a femtosecond laser system in conjunction with the x-ray SASE beam, accommodates a technique for the production of attosecond long x-ray pulses **[4-112]**. The basic layout of the attosecond x-ray source is sketched in Figure 4.8.3.

In this scheme, an ultra-short laser pulse is used to modulate the energy of electrons within the femtosecond slice at the manipulation-laser frequency. The manipulation laser pulse has to overlap with the central area of the electron bunch. To modulate the electron beam energy, laser pulse and electron bunch collinearly pass a few-period modulator-undulator tuned to the central wavelength of the laser. The energy-modulation depth and chirp provided by the mJ-level two-cycle laser allows for generation of a single 300 attosecond x-ray pulse. This x-ray pulse is then separated from the SASE radiation of the un-modulated beam using a monochromator. Further details are described in **[4-113]**.

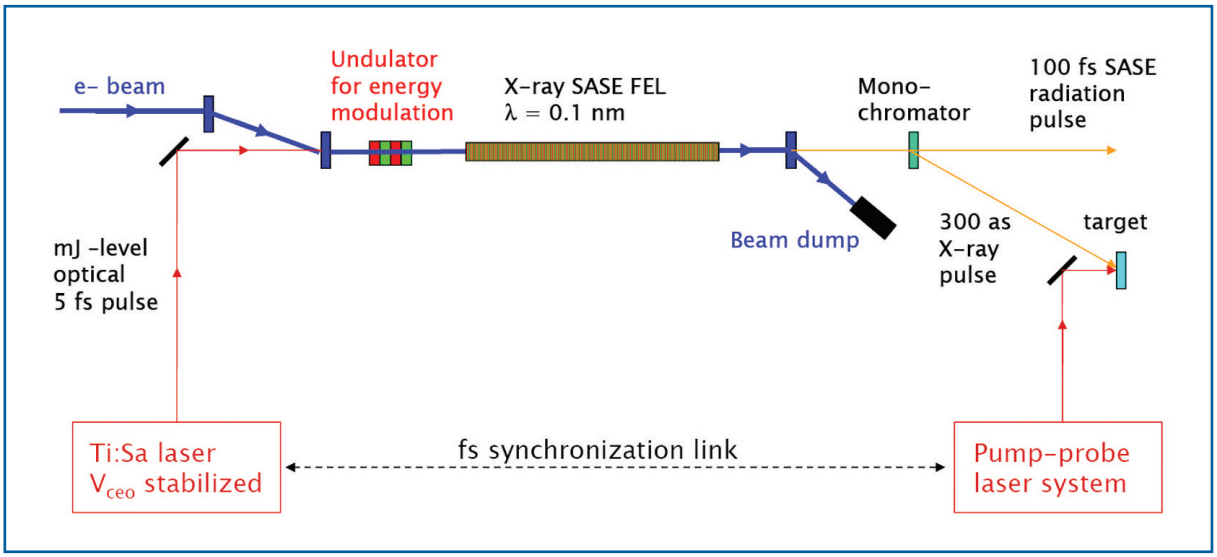

Figure 4.8.3 *Scheme of the layout for attosecond x-ray production. The synchronisation of the attosecond pulse is determined by the two-cycle laser and independent of the electron beam arrival. The manipulation and the probe laser have to be locked to one another.*

Unlike the option of post-sorting experimental data, the reliable generation of attosecond x-ray pulses requires the electron bunch to be synchronised to the manipulation laser to within a fraction of the electron bunch duration (~30 fs rms). Furthermore, investigations of physical processes in a pump-probe configuration using the 300 attosecond x-ray pulses, now mean the synchronisation between the two laser systems must be maintained with femtosecond precision. The few-cycle laser will be housed upstream of the SASE undulator at a distance of 1 km to the pump laser located in the experimental hutch.

4.8.1.3 Requirements of the XFEL synchronisation system

The synchronisation system for the XFEL has to meet the following requirements:

- it should serve as a timing reference to the XFEL, providing femtosecond stability between all significant points throughout the facility with small or negligible drifts over days and weeks. This reference system must be self-contained, without the need for recalibrations;
- it must provide RF signals or the possibility to lock ultra-low-noise RF local oscillators to the timing reference at different frequencies;
- it must provide a mechanism to lock various laser systems, as in those used for electron beam generation, beam diagnostics, pump-probe experiments, seeding, and other applications;
- the system stability, robustness, and maintenance should not limit machine availability or delay commissioning;
- the failure modes should be transparent and allow for rapid repair and start-up;
- expenditure should be moderate and cost-effective.

The synchronisation accuracy requirements are only achievable through an optical distribution of the timing signals, even though there is decades more experience with RF-based timing distribution through coaxial cables. This is because the sensitivity of optical phase-detectors far exceeds the capability of RF phase-detection. The robustness of the optical system has yet to be demonstrated, although the potential is present. The constraints and needs of a stable optical synchronisation system must be studied in an accelerator environment. This is why a prototype will be thoroughly developed and tested at FLASH at DESY. Due to the newness of the optical technology and the proven techniques of the RF technology, a hybrid system is a likely choice, in order to exploit the advantages of each.

4.8.2 Layout of the XFEL synchronisation system

This section describes the layout and main components of an optical synchronisation system as sketched in Figure 4.8.4. The system was first proposed by the Massachusetts Institute of Technology (MIT) **[4-114, 4-115]** and is currently being developed collaboratively by MIT, Sincrotrone Trieste and DESY.

To provide a stable timing-reference with a master-laser oscillator (MLO), one must lock the laser to a low-noise RF oscillator or to an atomic clock based on an optical frequency standard, as described in Section 4.8.2.1. The MLO under consideration is a mode-locked fibre laser that produces a stream of short optical pulses centred at a wavelength of 1550 nm. The pulse-stream is distributed in a dispersion-managed optical fibre to compensate for the pulse-broadening effects of non-linear dispersion. A fraction of the optical pulse-stream is sent back through the same fibre for stabilisation purposes. By correlating the arrival-time of the return pulses with pulses directly delivered from the MLO, the round-trip time is kept constant by means of a feedback loop that changes the length of the optical fibre.

The possibility of using optical cross-correlation of ultra-short pulses with about 200 fs FWHM duration to stabilise the optical-link provides:

- excellent sensitivity to detect optical path-length variations. A 1% change in the cross-correlation signal between the MLO and the return pulse corresponds to 2 fs difference in the group velocity delay;
- a detection process that is potentially drift-free. The pulse-duration sets an upper-limit on the possible drift because the two pulses must overlap. Furthermore, all critical devices used are optical elements with negligible or very small but controllable thermal dependence.

The laser pulse-stream used to stabilise the optical link also provides the timing information to the accelerator sub-systems. It is important to use a detection mechanism for the accelerator sub-systems that is equivalent to the one used for the fibre link stabilisation. While for cross-correlation, the time-slice with largest derivative of the envelope is used, a measurement of the centre-of-mass of the laser pulse envelope or any other parameter which is rigidly related to the laser-pulse envelope is also an option. To ensure the success of different detection schemes, the frequency spectrum and the output chirp of the laser pulse exiting the MLO have to be sufficiently stable. Thus, currently available commercial fibre lasers are not specified to the extent necessary for this application and one has to expect that these lasers are not optimised for low phase-noise performance.

The longest round-trip time of the laser pulses through optical links in the XFEL Facility is 30 microseconds. Corrections for faster fluctuations of the optical path-length cannot be made and it depends on the short-term stability of the link end-stations how much these uncorrectable path-length fluctuations impact on the final synchronisation precision. The limitation due to the round-trip time will be explored in the near future.

The laser pulses distributed in the facility can be used, in some cases, for a high-accuracy direct timing measurement. For example, the electron beam arrival-time can be detected from a simple pickup with broadband electro-optical modulators (EOMs) developed for the telecommunication industry (see Section 2.2.4). EOMs can also be used to precisely detect the phase of the acceleration RF in superconducting cavities, by sampling the RF with the laser pulse-stream of the timing reference system. Similar techniques allow for measurement of the arrival-time of picosecond-long laser pulses, where optical cross-correlation is difficult to apply.

The second application where optical timing pulses are of great advantage is the synchronisation of various other laser systems used throughout the facility. For example, by frequency doubling the 1550 nm to 775 nm, a regenerative Titan-Sapphire amplifier can be seeded, as proposed for the optical-replica synthesis experiment at the FLASH/VUV-FEL.

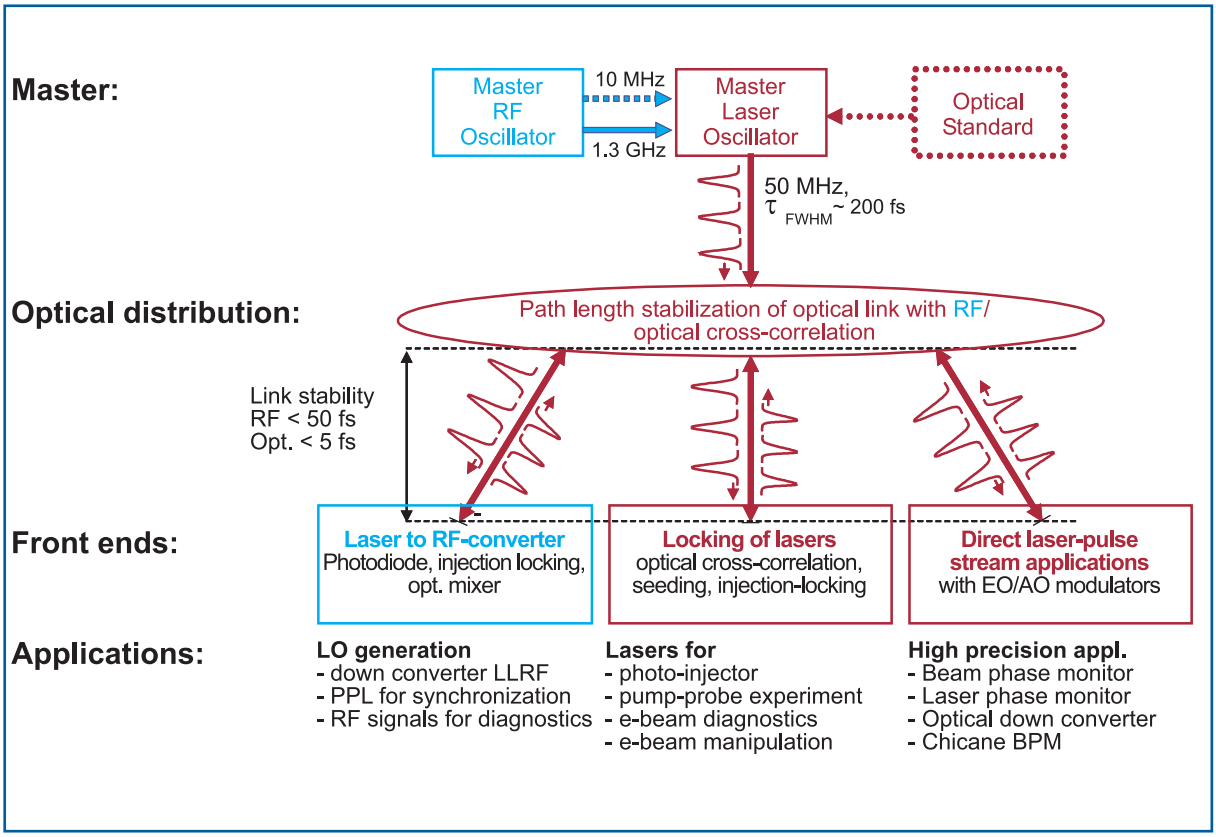

Figure 4.8.4 *Scheme of the laser-based synchronisation system for the XFEL. Three levels can be distinguished: the MLO providing a stream of identical optical pulses at a defined repetition rate.The length-stabilised fibre-link distribution to all timing critical devices in the facility and front-ends classified in three different types and their applications.*

Bunch length measurements, for instance, by EOS can be carried out by directly using the optical pulse-stream of the timing system, eliminating the need for an extra laser system. Optical cross-correlation by sum-frequency generation between the optical timing pulses and a laser system providing ultra-short laser pulses allows for precise monitoring or the operation of phase-lock-loops with femtosecond stability **[4-116, 4-117]**. Laser systems can also be synchronised directly through injection-locking, where the master-laser pulse-stream is injected into another mode-locked laser oscillator to be synchronised **[4-118]**.

For the control of the acceleration RF, the optical pulse-stream has to be converted to an RF signal without loss of timing accuracy. Several different techniques providing a clean RF reference are discussed in Section 4.8.2.3.

4.8.2.1 Frequency combs

This section will discuss the issues that go into the choice of mode-locked lasers for timing applications. The following material is a summary of reports about optical mixers and attosecond synchronisation **[4-119, 4-120]**.

Recently, new insight into the frequency and noise characteristics of mode-locked lasers has initiated intense research activities in new directions. In the frequency domain, the pulse-train from the mode-locked laser contains millions of regularly spaced frequency lines, which is often called an optical frequency “comb”. Figure 4.8.5 shows the time-frequency correspondence between the pulse train and the frequency comb.

By stabilising the spacing (repetition frequency) and the offset (carrier envelope offset frequency) of the frequency comb, one can measure an arbitrary optical frequency with unprecedented accuracy. This frequency property of mode-locked lasers has enabled precision frequency spectroscopy and provided a platform for an optical atomic clock **[4-121]**.

Another interesting and important aspect of the pulse trains from mode-locked lasers is their excellent noise performance. Mode-locked lasers can produce extremely low jitter RF-signals as a form of optical pulse trains **[4-122 – 4-124]**. Due to their excellent phase-noise performance, mode-locked lasers are expected to serve as a master clock source for systems requiring stringent synchronisation performance, such as high speed (>GHz), high-resolution optical sampling, analogue to digital converters (ADCs) and large-scale optical clock signal distribution and synchronisation systems, such as those needed for fourth generation light sources and advanced accelerator systems.

The RF-signal is encoded in an optical pulse train, as shown in Figure 4.8.5. By direct photo-detection with a fast photodiode, the optical signal is converted to an electrical signal with frequency components of the fundamental repetition frequency (f_R) and its harmonics up to the detector bandwidth. By bandpass filtering the desired frequency component (nf_R), we can extract the RF signal from an optical pulse train. Figure 4.8.6 illustrates direct photo-detection for the RF signal regeneration from optical pulse trains.

Although the RF signal encoded as an optical pulse train exhibits an extremely low timing jitter of sub-10 fs levels **[4-123, 4-124]**, the extraction of a clean RF signal from the pulse train is a non-trivial task.

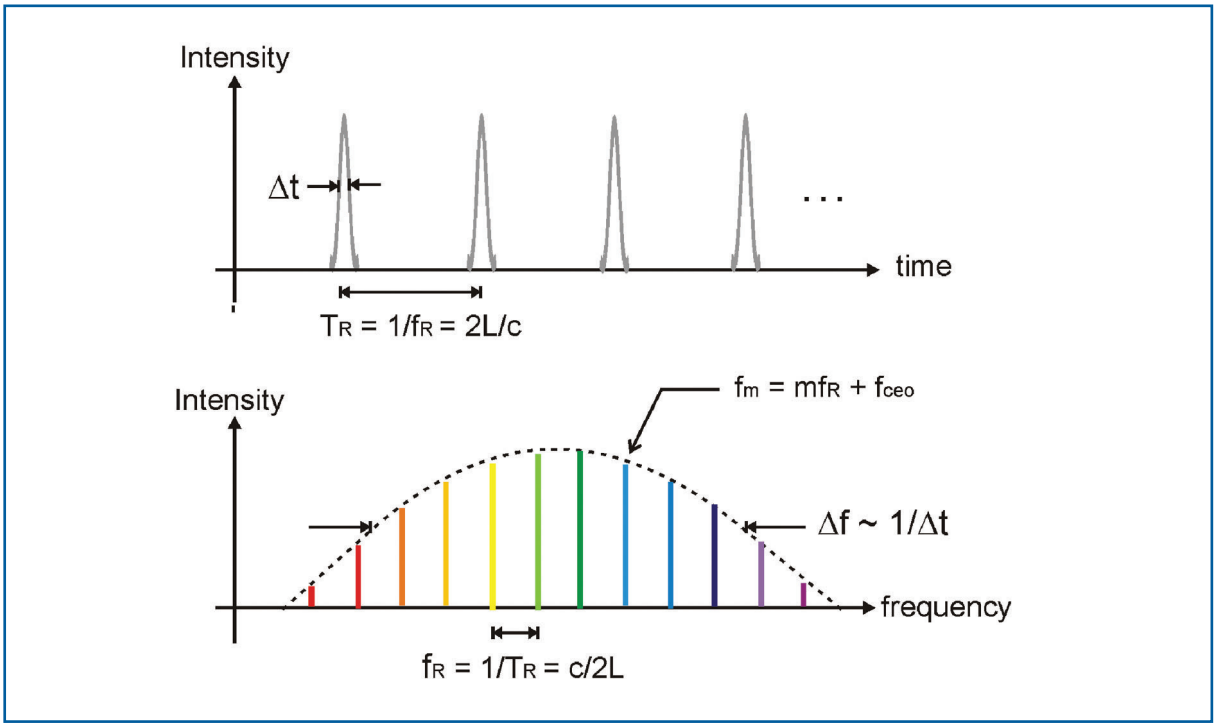

Figure 4.8.5 *Time-frequency correspondence between the optical pulse train in the time domain and the frequency comb in the frequency domain. The pulse train has a period of T_R, the same as the round-trip time (2 L/c where L is the laser cavity length and c is the velocity of light) in the laser cavity. In the frequency domain, this pulse train corresponds to regularly spaced frequency lines whose bandwidth is inversely proportional to the pulse width ($\Delta f \sim 1/\Delta t$). The spacing corresponds to the repetition frequency $f_R = 1/T_R$, and the whole comb lines are shifted by an offset frequency f_{ceo}. Each comb line can be expressed as $f_m = mf_R + f_{ceo}$ (m=integer).*

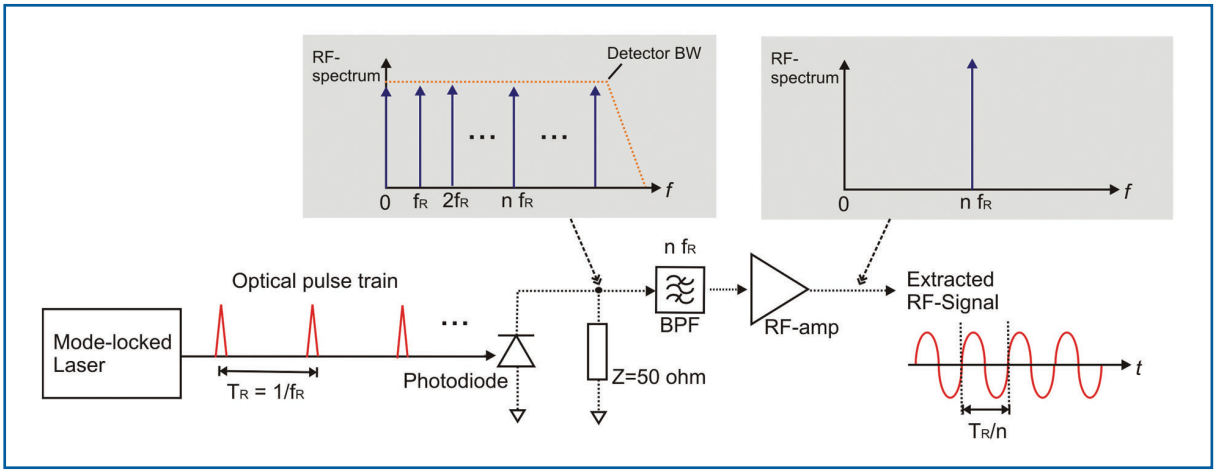

Figure 4.8.6 *Direct photo-detection for the RF signal regeneration. The optical pulse train is converted to an electrical signal by a photodiode. By proper bandpass-filtering, we can extract the desired RF signal. BPF: bandpass filter; BW: bandwidth.*

4.8.2.2 *Choice of the master-laser oscillator*

Mode-locked fibre lasers are a natural choice for an MLO, because of the ease of coupling into the fibre distribution system, their excellent long-term operating stability, and the well-developed and mature component base available at the optical communications wavelength of 1550 nm. Fibre lasers can generate pulses from picosecond down to 35 fs in duration by simultaneous phase-coherent lasing of multiple longitudinal modes spaced in frequency domain by the pulse repetition rate of the laser.

Mode-locking is initiated by a mechanism providing lower loss (hence, higher net gain) for a pulse than for CW radiation, leading to pulse formation from intra-cavity noise as soon as the laser reaches a certain intra-cavity power **[4-125]**. For passively mode-locked lasers, this is achieved by a real or artificial saturable absorber. Non-linear polarisation evolution in combination with a polariser, serves as an artificial saturable absorber. Non-linear polarisation rotation can occur in an optical fibre when the initial polarisation state is elliptical. The ellipse can be resolved into right- and left-hand circular polarisation components of different intensities. These two circular components then accumulate different non-linear phase shifts related to the intensity dependence of the refractive index (Kerr-effect $n(I) = n_0 + n_2 I$). The polarisation ellipse rotates while maintaining its ellipticity and handedness. An optical fibre is particularly well suited for non-linear polarisation rotation because the small mode diameter leads to high intensities, and thus, to a large non-linear refractive index change. Figure 4.8.7 shows how non-linear polarisation rotation can be used in conjunction with bulk polarisation optics to obtain an artificial saturable absorber.

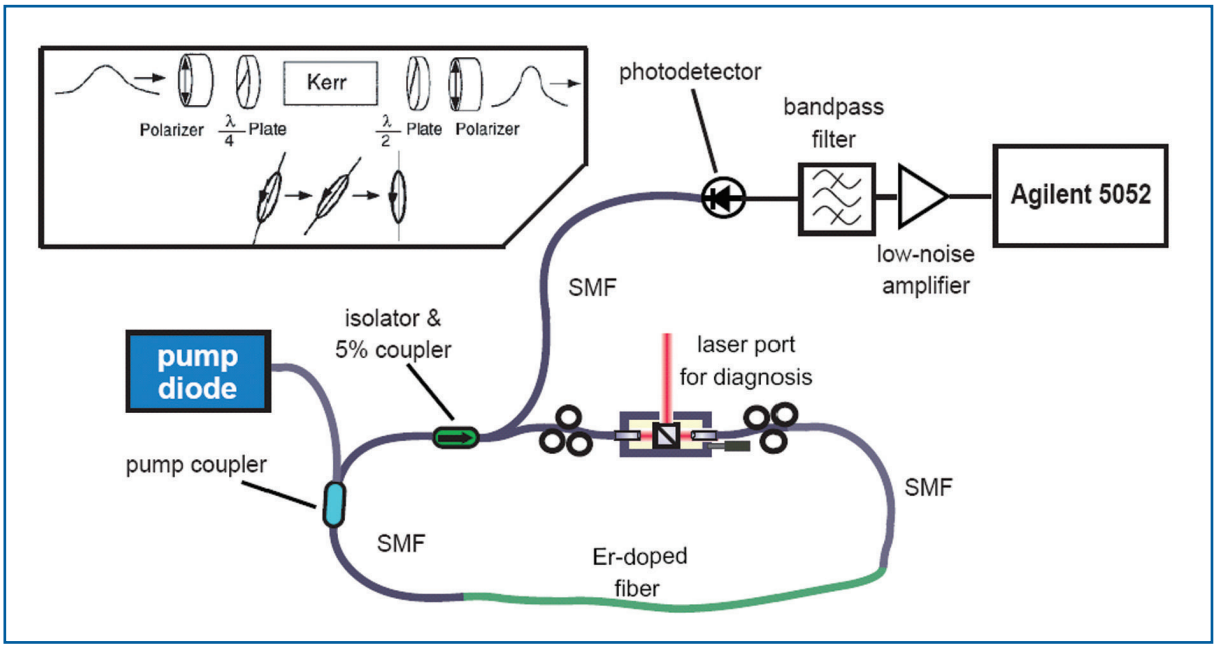

Figure 4.8.7 *Scheme of the Erbium-doped fibre laser generating the optical pulse-stream for synchronisation. The Erbium fibre is pumped by commercial diodes at 980 nm wavelength. Passive mode-locking is achieved by an artificial saturable absorber. The inset sketches the polarisation change after the polariser due to Kerr-nonlinearity. A 5% output coupler is used to determine the phase-noise spectrum of the laser-pulse-stream via photo-detection.*

While propagating through the fiber, the polarisation of the intense centre of the pulse is rotated more than that of the wings. Before going through the polariser, a polarisation controller rotates the polarisation such that, the centre of the pulse passes the polariser and the wings are absorbed. The second controller makes the polarisation elliptical before the pulse enters the fibre again.

One of the key features of the MLO is the possibility of generating multiple RF frequencies from the same source with very low phase-noise performance. For offset frequencies above 1 kHz, the intrinsic phase-noise of a free-running fibre laser is comparable to the best commercial microwave oscillators. This is due to the high equivalent microwave Q of the fibre laser, the long upper state lifetime of Erbium (~ ms) which results in the low-pass filtering of pump-power noise for frequencies above 1 kHz. Figure 4.8.8 shows the single-sideband phase-noise spectrum, L(f), of the harmonic at f_0=1.3 GHz extracted from the pulse train upon photo-detection and filtering. This phase-noise spectrum can be converted into timing jitter using:

$$\Delta t = \frac{\sqrt{2\int L(f')df'}}{2\pi f_0}$$

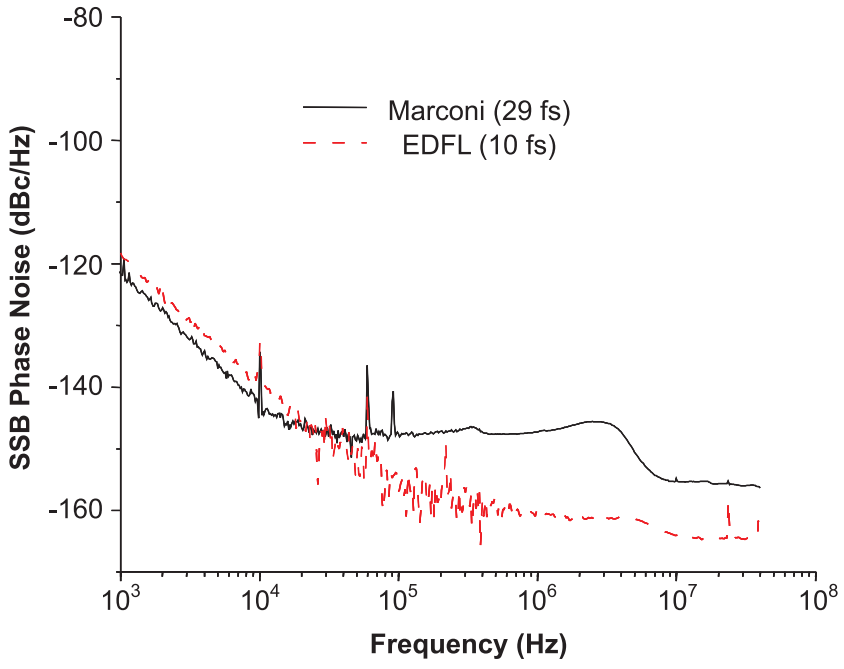

Figure 4.8.8 *Single-sideband phase-noise spectrum of the MLO, measured at a frequency of 1.3 GHz. The integrated timing jitter in a band from 1 kHz to half the repletion rate of the oscillator amounts to less than 10 fs, limited by the phase detector. For comparison, a good RF-oscillator (black curve) is also plotted.*

The integrated timing jitter from 1 kHz to the Nyquist bandwidth, i.e., half of the laser repetition rate, is measured at about 10 fs, limited only by the photo-detection process. For comparison, the phase-noise of a very low-noise frequency generator, a Marconi 2041, is also plotted.

At lower offset frequencies, the laser is susceptible to environmental perturbations (microphonics, temperature, etc.). By phase-locking the fibre laser to a low phase-noise commercial RF oscillator, these environmental perturbations can be eliminated. The phase-noise of the locked fibre laser will follow the microwave oscillator for offset frequencies up to the unity gain of the PLL and still has the excellent high-frequency properties of a free-running laser. After photo-detection, a harmonic of the laser repetition rate is picked by a suitable bandpass filter and compared to the reference oscillator in a phase detector. After amplification and filtering, this signal is fed to a piezo-based fibre stretcher incorporated into the laser cavity and it adjusts the repetition rate.

4.8.2.3 Laser to RF conversion

To convert the optical pulse-stream to a clean, high-frequency RF signal (MHz-GHz) with sufficient output power and without the loss of timing accuracy, in the following, three different schemes are discussed.

Fast photodiodes

To extract an RF signal with frequency $f = n f_R$, only a fast photodiode, a bandpass-filter tuned to the frequency f, and a low-noise amplifier, as shown in Figure 4.8.6, is required. For many applications, this scheme provides the most cost-efficient solution to deliver RF frequencies from 50 MHz up to 10 GHz. The limitations of the photo-detection process in terms of timing stability and drift performance are under investigation.

Recently, it has been shown that the extraction of an RF signal from an optical pulse train using direct photo-detection is limited in precision by excess phase-noise **[4-126]**. The major origin of this excess noise has been identified to be an amplitude-to-phase (AM-to-PM) conversion in the photo-detection process. Figure 4.8.9 shows the AM-to-PM conversion process in the photodiode. The AM-to-PM conversion factor is measured to range typically from 1 to 10 ps/mW **[4-124]**, depending on the bias-voltage and diode types. The amplitude noise of the laser can be converted into a significant amount of phase-noise by this conversion process. Here is one numerical example: if the conversion factor is 1 ps/mW and the applied optical power is 10 mW, the required amplitude regulation is within 0.1% to reach 10-fs jitter level, which is already a challenging requirement.

The sensitivity of AM-to-PM conversion can be significantly reduced by operating the photodiode close to saturation and by the use of additional laser amplitude stabilisation feedback through a fast amplitude modulator. The limitation of the output power delivered by photodiodes puts constraints on the achievable signal-to-noise ratio (SNR) of the regenerated RF signal. Since semiconductor devices typically show high temperature-sensitivity, the use of photodiodes may limit the performance for the long-term stable and drift-free operation of the RF signal regeneration. Theoretical and experimental investigations to explore the limitations on the phase-noise, drift performance and long-term stability of photo-detectors is, therefore, an important part of the near future R&D programme.

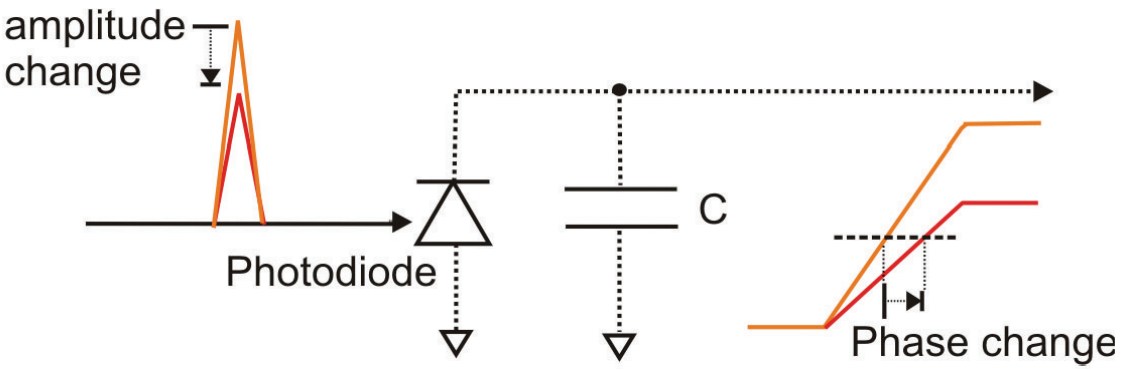

Figure 4.8.9 *Conceptual diagram of AM-to-PM conversion through direct photo-detection. Spatial charge distribution in the photodiode induces a change in the capacitance (denoted as C in the figure) of the diode. This results in a change in the phase of the converted electrical signal. By this process, amplitude noise in the optical domain is converted to phase-noise in the electronic domain.*

Injection locking to low noise oscillators

If simple photo-detection is insufficient to generate an RF signal with the desired stability, it is possible to lock an external voltage controlled oscillator (VCO) to the laser pulse-train. A dielectric resonator oscillator (DRO) optimised for low phase-noise at high offset frequencies is suitable. A very simple and effective approach to achieve the phase locking is to make use of the phase pulling capability of the oscillator and injection lock the DRO.

The dielectric resonator acts as a high-Q bandpass filter. Part of its output is amplified and fed back to the resonator. This loop has to be kept on resonance to achieve a stable output, hence the net phase shift has to be n×360 degrees of the DRO resonance frequency. If a perturbation in the phase balance is introduced by an electronic phase shifter, the DRO will compensate for this shift by changing its centre frequency. The photo-detected laser pulse-train can be directly applied to the high-bandwidth phase shifter. This enhances the quality of the phase-lock significantly compared to applying a sinusoidal wave.

The unity gain can be adjusted by varying the amplitude of the phase perturbation. So this scheme only consists of a photo-detector, a variable attenuator, and the DRO, making it very cost-effective.

The key part is, however, the DRO. It has to have at least comparable high-frequency phase-noise properties to the MLO, as the PLL can only regulate up to a certain frequency (1-10 kHz). Therefore, the RF output signal reflects the DRO phase-noise above the unity gain frequency, while following the timing reference for lower frequencies.

In cooperation with Poseidon Scientific Instruments (PSI), an ultra-low phase-noise DRO has been developed **[4-127]**. The measured timing jitter is less than 4 fs, integrated from 1 kHz to 1 MHz at a frequency of 1.3 GHz (see Figure 4.8.10). The implemented

phase shifter has a bandwidth of 10 GHz. This enables the complete bandwidth transfer of ultra-fast photodiode signal, increasing the locking accuracy. Due to the nature of the process, injection locking is insensitive to offset drifts of the photo-detectors and only weakly sensitive to gain drifts.

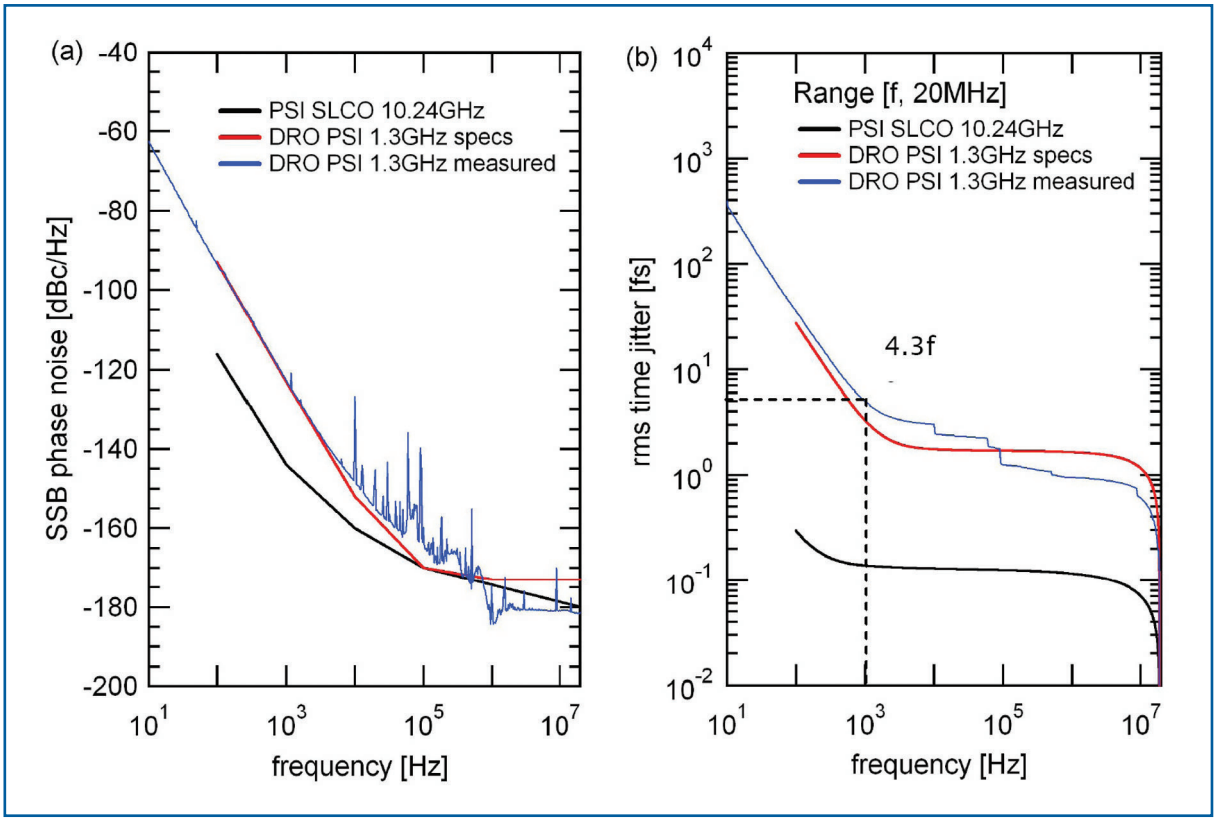

Figure 4.8.10 *(a) Single-side band phase-noise spectrum of the DRO produced by PSI. The DRO is a critical component for optical-to-RF conversion schemes. The red and blue curves shows the single-sideband (SSB) specification and measurement. For comparison, the black curve shows the best so far existing RF oscillator (10.24 GHz, Sapphire loaded SLCO from PSI) . (b) Integrated timing jitter between f and 20 MHz.*

Balanced optical to RF phase detector

An entirely different technique to regenerate an ultra-low noise RF signal from the optical pulse-stream, which does not rely on the phase-detection by photodiodes, instead it uses optical-electrical hybrid PLLs **[4-128]**. As shown in Figure 4.8.11, the continuous wave RF-signal is generated by an ultra-low-jitter VCO as, for example, the DRO described above. The RF phase of the VCO is measured by a low-jitter, and to first order, drift-compensated optical-RF phase detector and regulated with the error signal of the phase detector by a low-noise loop filter.

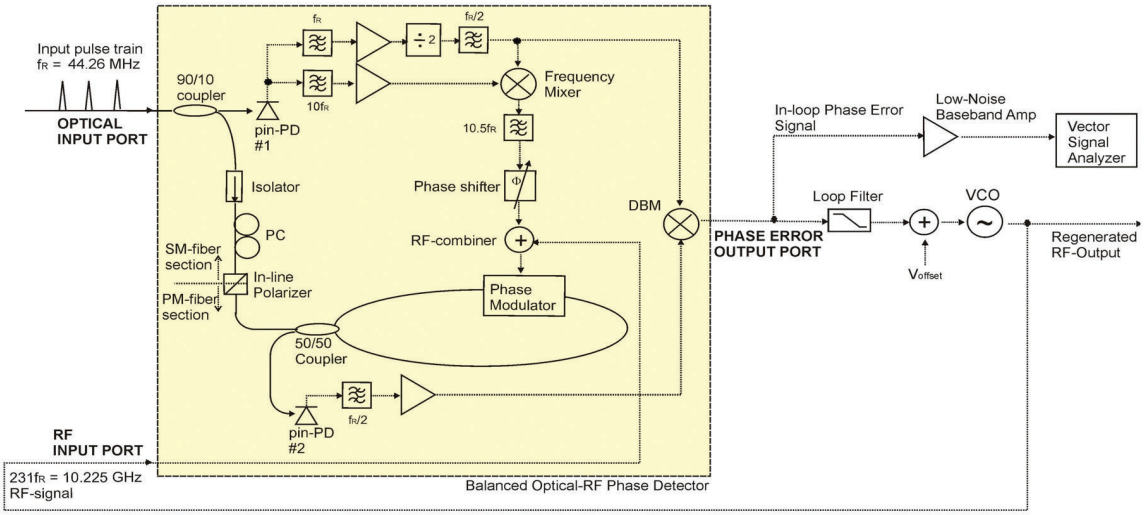

Figure 4.8.11 *Schematic setup for RF signal regeneration from an optical pulse train by use of the balanced optical-RF phase detector (yellow box) and a PLL. DBM: double-balanced mixer; PC: polarisation controller; PD: photodiode; PM: polarisation-maintaining; SM: single-mode; VCO: voltage-controlled oscillator. Solid line: optical beam path; dotted line: electric signal path.*

The optical-RF phase detector itself is marked by the yellow box. The photodiode #1 is used to generate a reference signal for a synchronous-detection scheme with half of the repetition frequency ($f_{R/2}$) of the incoming optical pulse-stream. The Sagnac-loop together with the phase-modulator, encodes the phase-error signal of the VCO in the amplitude of the $f_{R/2}$ frequency component detected by the photodiode #2. The mixer down-converts the phase-error signal at $f_{R/2}$ to the baseband through synchronous detection with the reference signal. This baseband signal is the phase error output of the balanced optical-RF phase detector.

A first measurement of the in-loop phase-noise of the balanced optical-to-RF phase detector is shown in Figure 4.8.12.

The voltage signal from the phase error output port was measured with a low-noise preamplifier and vector signal analyser (VSA) converted into SSB phase-noise at 10.225 GHz VCO operation frequency. The black line shows the in-loop phase-noise and the red line is determined by the VSA noise floor. The measurement shows an integrated in-loop timing jitter of 8.8±2.6 fs from 1Hz to 1MHz. The jitter will be significantly improved in the near future by using ultra-low-noise electronics, components with small drifts, and the PSI DROs.

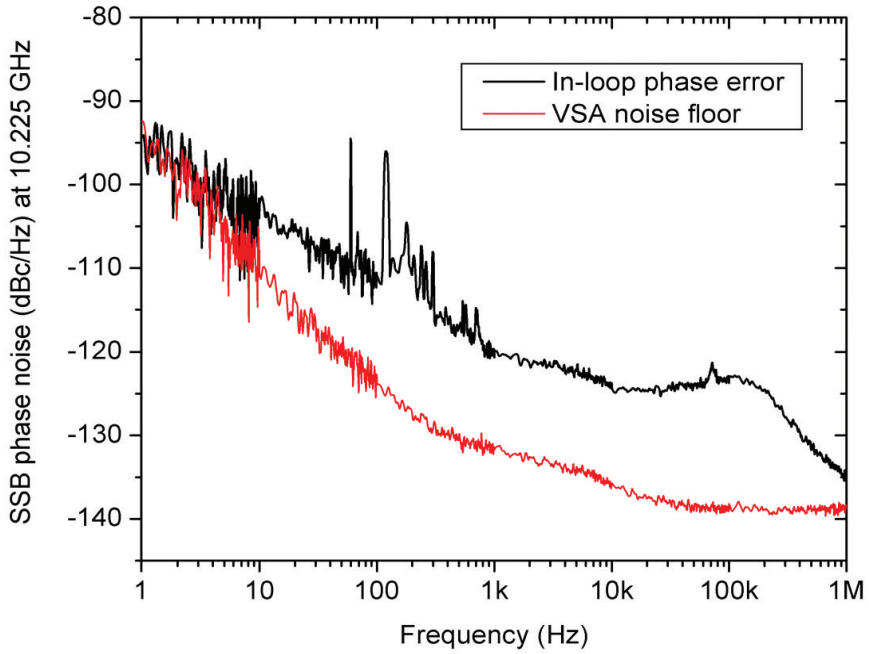

Figure 4.8.12 *The SSB in-loop phase-noise spectra at 10.225 GHz. Black line: in-loop phase-noise when it is locked. Red line: VSA noise floor. The integrated timing jitter from 1 Hz to 1 MHz corresponds to 8.8 fs ± 2.6 fs.*

4.8.2.4 Fibre length stabilisation: options and first results

The stabilisation of the fibre transmission line is a crucial part of the optical synchronisation system. The stabilisation system needs to satisfy two aspects:

- it must have enough range to cover the total optical path length change over 3 km for all temperature variations that might occur;
- the resolution of the phase-detector should allow for a stability of ~ 10 fs over long timescales of minutes to hours.

Neither an RF-based system nor optical cross-correlation fulfils both requirements at the same time. Any present day RF mixer will drift with a coefficient of ~200 fs/K (at a frequency of 1.3 GHz), so will not be suitable for long-term stability. It, however, has a dynamic range of several 100 ps, compared to the optical cross-correlation where the range is given by the optical pulse length (~200 fs). Hence, a hybrid system of two feedbacks is required. One coarse RF-based feedback ensures that there is a coarse overlap so the optical cross-correlator can operate.

One of the main features to enable optical cross-correlation, is the dispersion management of the fibre. Since the pulse needs to be short after returning through the fibre, the net dispersion of the fibre link must be zero. This can be accomplished by using matching fibre parts with opposite sign and dispersion slope. When transmitting pulses with a duration of about 200 fs over long distances, higher-order dispersion also needs to be compensated. The choice of wavelength 1550 nm, makes manufacturing optical fibres with these properties possible. These have been available for a few years, driven by the demand of the telecommunications industry.

Another important aspect is the radiation hardness of the optical fibres used in the tunnel. Standard telecommunications fibre uses compounds during manufacturing that darken upon exposure to radiation. There are, however, commercially available fibres featuring significantly lower attenuation per km and dosage. With appropriate shielding of both fibre and localised radiation hotspots (collimators, bunch compressors, etc.), there is no anticipated problem with radiation induced attenuation in the fibre.

A sketch of the fibre link is shown on the left-hand side of Figure 4.8.13. A fraction of the laser light entering the fibre link is reflected back at the end for stabilisation purposes. This, together with laser pulses directly from the MLO, is used to operate the: (a) RF-based feedback and (b) optical cross-correlator. A fibre-stretcher for correcting high frequency perturbations and a delay-line for slower corrections serve as actuators for the feedback.

Tests have been performed with a RF-based feedback at the MIT-Bates laboratory **[4-129]**. In-loop measurements, on the right-hand side of Figure 4.8.13, indicated a stability of 12 fs closed loop over a timescale of 30 seconds, compared to about 60 fs open loop for a 500 m long fibre link. This very promising result shows that an RF-feedback alone is capable of stabilising the link over shorter time-scales on the order of 10 fs. From the measurement result no significant phase-noise degradation of the optical pulse-stream within the accuracy of photo-detection after transmission through the fibre link was observed. A fibre-link stabilisation system including different versions of optical cross-correlation (either by two-photon absorption or second-harmonic generation) is presently under investigation.

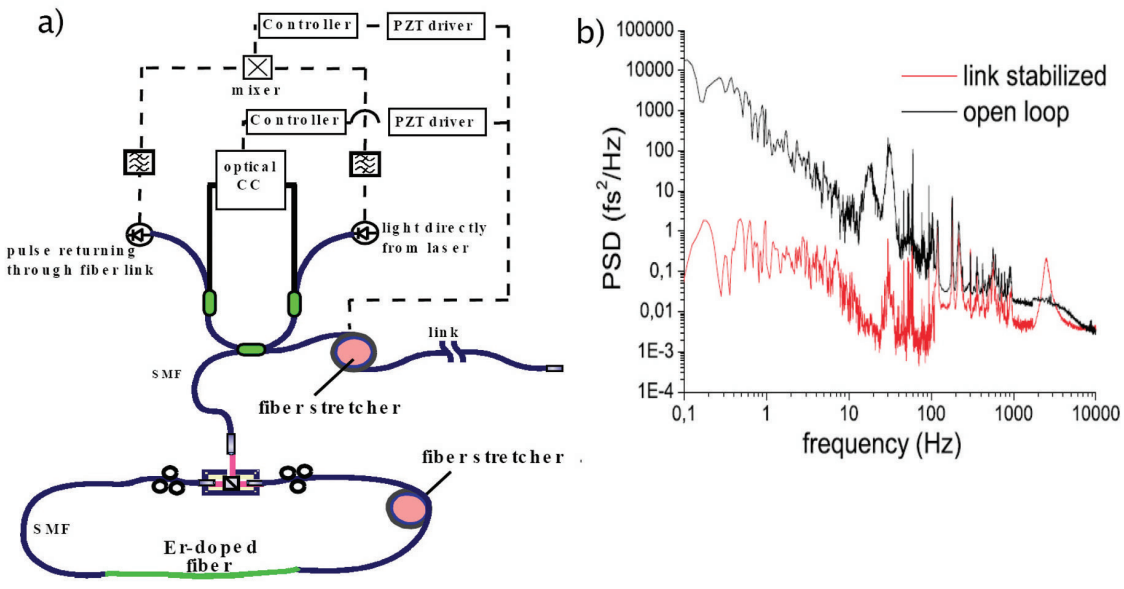

Figure 4.8.13 *(a) Scheme of the two feedback fibre link stabilisation system. The coarse fibre link feedback with a large dynamic range is realised by RF means. The high precision and long-term stability is realised by optical cross-correlation. (b) Phase-noise spectrum of open and closed feedback back loop using only RF stabilisation for a 500 m fibre link test at MIT-Bates.*

4.8.2.5 *Beam phase monitor system*

In collaboration with Sinchrotrone Trieste[7] a compact, high-precision beam arrival-time monitor is being developed (see Figure 4.8.14). The arrival-time is measured by detecting the fast transient signal of a broadband beam pick-up. The pick-up consists of a ring-electrode held by two feed-throughs mounted at opposite sides of the ring. If an electron bunch passes the pick-up, a 200 ps-wide RF pulse is generated with a peak-to-peak voltage of more than 50 V. The large transients of ~0.5 V/ps at the zero-crossing of the signal, permit precise determination of the bunch arrival-time. For that, the beam pickup signal is fed into an EOM with appropriate bandwidth (more than 10 GHz is commercially available). A laser pulse from the optical timing system injected into the EOM at the proper time is sampling the RF pulse transient close to its zero-crossing. In this way the arrival-time of the electron bunch is encoded as an amplitude change into the laser pulse. The amplitude change of the laser pulse is detected by a photodiode and sampled with a fast ADC. Since the laser pulses from the timing system are directly used, no additional devices that may add timing jitter are required.

In first measurements, a resolution of 140 fs could be achieved, limited by readout noise of the photo-diode signal (1% rms). By improving the system components, sub-20 fs resolution seems to be feasible.

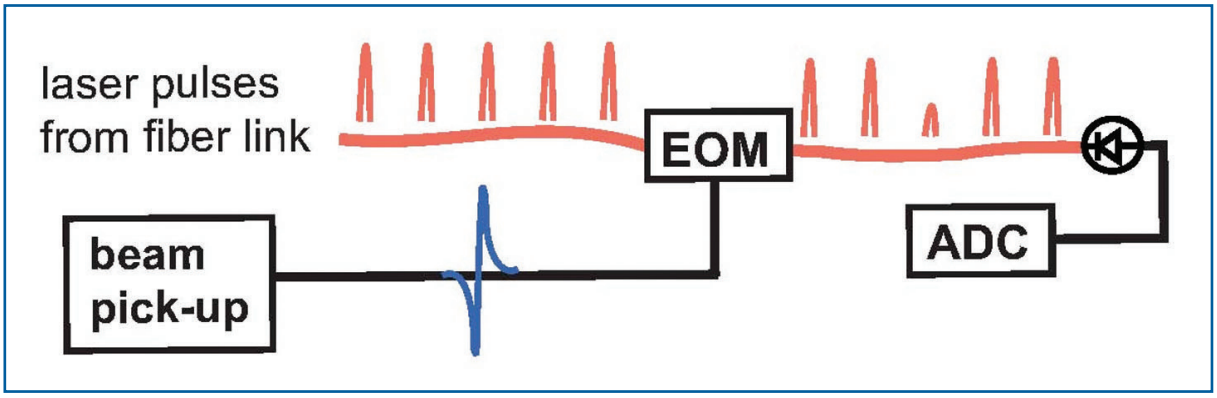

Figure 4.8.14 *Schematic setup of a beam arrival-time monitor system.*

A similar setup can be used for an ultra-precise BPM in the dispersive sections. Instead of the circular beam pick-up, used for the beam arrival-time monitor, a strip-line pick-up, mounted perpendicularly to the beam direction, is used. The pulses generated at each end of the strip-line are used as modulation signals for EOMs. The difference in the arrival-time of the pulses is proportional to the beam position along the strip-line.

4.8.3 Distribution of trigger and clock signals

The increased sampling rate of present day ADCs imposes significant stability constraints on the clock distribution system. It offers the possibility of direct In-phase/Quadrature (IQ) detection that is limited primarily by the jitter between the clocking frequency of the ADCs

[7] Work is funded in part by the EU FP6 contract 011935, EUROFEL.

and the signal to be sampled. To meet specifications this translates to an allowable timing jitter of less than 10 ps. Clock signals are normally understood as a continuous square-shaped signal used primarily to clock ADCs while a trigger signal indicates the start of an event. The timing of the trigger is much less critical than that of the clock signal, but the distribution is usually combined with the clock using pulse-width modulation.

The clock distribution for the XFEL will be based on readily available optical telecommunication technology that uses an optical fibre similar to the laser-based optical synchronisation system fibre. Clock and trigger signals are generated electronically and transferred to a CW laser by amplitude modulation. The receiver is a photodiode which converts the clock train back into the electronic domain. The demand for picosecond clock and trigger signal stability makes either a direct stabilisation of the optical path length of the fibre or a measurement and subsequent software correction mandatory. A fibre-length stabilisation at the femtosecond-level will be realised anyway to fulfill the demands of the optical synchronisation system. A combination of both systems is, therefore, desirable to reduce R&D effort.

Laser radiation of different wavelengths can propagate without mutual interference through a single optical fibre, enabling multiple channel transmission in optical telecommunication lines. A similar approach is chosen here. The clock distribution system can operate at 1,310 nm which is also a telecom wavelength, thus components are readily available. A wavelength division multiplexer (WDM) coupler is used to combine both the 1,550 nm laser radiation for the synchronisation system and the 1,310 nm radiation for the clock and trigger distribution system. Both wavelengths co-propagate until the end of the link, where a second WDM coupler separates both wavelengths to their respective receivers. These couplers offer an isolation of more than 40dB, so cross-talk between the two channels is negligible. The advantage of such an approach is that both synchronisation and the clock distribution system can operate interference free, but use a common fibre and stabilisation system. The wavelength difference between both channels will lead to a degradation of the link stability for the 1,310 nm system. However, the anticipated stability level is of better than 100 fs. This easily far surpasses the requirements of 10 ps stability for the XFEL clock system.

4.8.4 Synchronisation of the LLRF for the main linac

The phase reference system for the main linac must provide the local oscillator signal (f_lo = 1350 MHz) and the RF reference signal (f_ref = 1300 MHz) to the 25 RF stations in the main linac. Each RF station employs more than 100 downconverter channels which require a total RF power in the order of 1 W for local distribution at each RF station. To ensure high availability a redundant distribution system consisting of a coaxial and an optical line will be installed as shown in Figure 4.8.15. In both cases the distribution frequency is 50 MHz and the receiver electronics generates the required frequencies of 1,350 MHz (LO), 1,300 MHz (reference and klystron drive), 50 MHz (from which the ADC clock is derived) and 5 MHz (bunch clock signal).

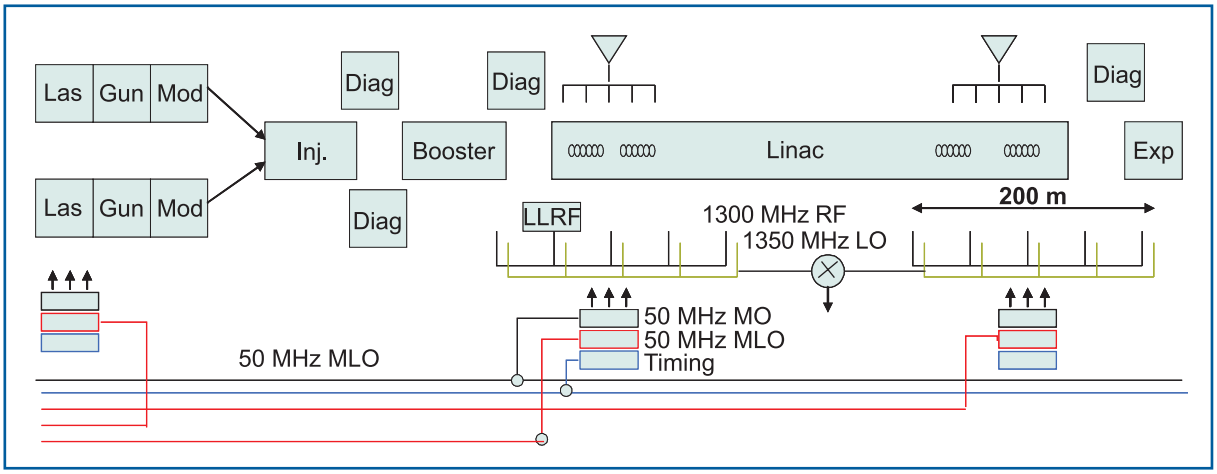

Figure 4.8.15 *The phase reference system of the main linac consists of a combination of coaxial and optical distribution systems to a few selected locations in the linac with coaxial sub-distribution for 5-7 RF stations.*

The coaxial system is extremely reliable due to the passive structure, can transport relatively high power levels to many tap points, and provide a reasonable long-term stability in the order of a few ps/km/deg C (consistent with a temperature coefficient of about 1 ppm/deg. C). For the short distances between two RF stations, the required phase stability of the order of 100 fs can be maintained. The fibre optical distribution is superior in stability (with active stabilisation) but provides only point to point connection and requires active RF components to provide the required power level.

The details of the distribution of the RF signals to one RF channel are shown in Figure 4.8.16. In the optical receiver, the 1,300 MHz and 1,350 MHz are generated by filtering of the desired harmonics of the 50 MHz while the harmonics in the coaxial receivers are generated by step recovery diodes or use of PLL loops. The clock signal is synthesised from the 50 MHz distribution signals and requires stability in the order of 5 ps rms. Trigger signals will be distributed through the timing system which will make use of the stability of the optical distribution.

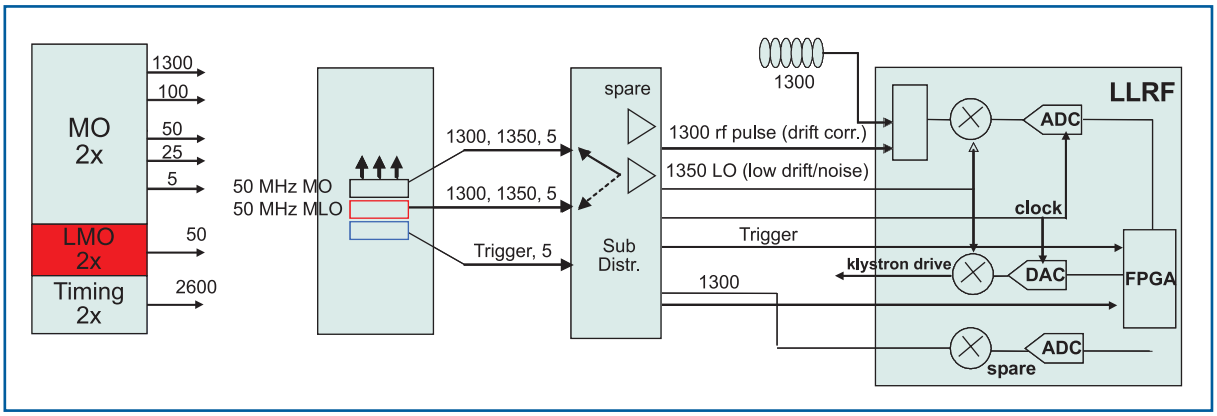

Figure 4.8.16 *The receivers for the optical and RF signal generate the required 1,350 MHz, 1,300 MHz, 5 MHz and clock signal (synthesised from the 50 MHz signal) for distribution to several RF stations.*

The sub-distribution of the 1,350 MHz and 1,300 MHz signals are achieved by phase stable 7/8" coaxial lines with a typical stability of better than 1.0 ppm/deg. C as shown in Figure 4.8.17. Redundant receivers and power amplifiers guarantee the required availability. Low cost fibre links with a stability of about 100 fs ensure good long-term stability.

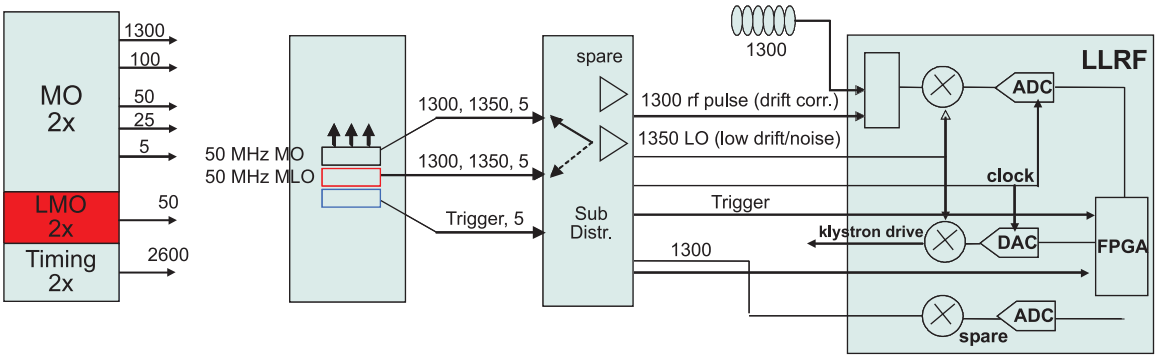

Figure 4.8.17 *Subdistribution of the 1350 MHz LO signal (same distribution for 1,300 MHz). The redundant receivers and power amplifiers ensure high availability. Low cost fibre optic references monitor the LO and RF reference stability at each RF station. The RF reference signal is distributed to each downconverter channel to provide on-line calibration.*

4.9 Summary of costs and manpower requirements

The capital investment and cost of the personnel necessary to realise the different sections of the accelerator complex as described in Sections 4.1 to 4.8 are summarised in this section. The basis for the cost estimate is the numbers and length of components specified here. For an overview about the total project cost, a description of the methodology of the performed estimate for capital investment, the determination of the costs for personnel and the expected uncertainties, see Chapter 10.

Table 4.9.1 gives a summary of the project cost in terms of capital investment and the cost of personnel for the accelerator complex. The relative distribution of the full costs for the accelerator complex is shown in Figure 4.9.1. The accelerator complex contributes about 35% to the overall capital investment and full costs of the XFEL project, in terms of cost for personnel, close to 40%. Integrated over the entire construction phase, 1,105.8 full-time equivalents (FTE) are required for the accelerator complex.

	Capital investment [M€]	Personnel cost [M€]	Full cost [M€]
Superconducting linac	199.69	48.64	248.32
Injector	9.38	5.87	15.25
Bunch compressors	13.28	10.08	23.36
Electron beamlines	38.61	20.86	59.47
Total	**260.96**	**85.45**	**346.41**

Table 4.9.1 *Project cost distribution for major items of the accelerator complex. Values are given for capital investment, personnel costs and full costs in Million-Euro.*

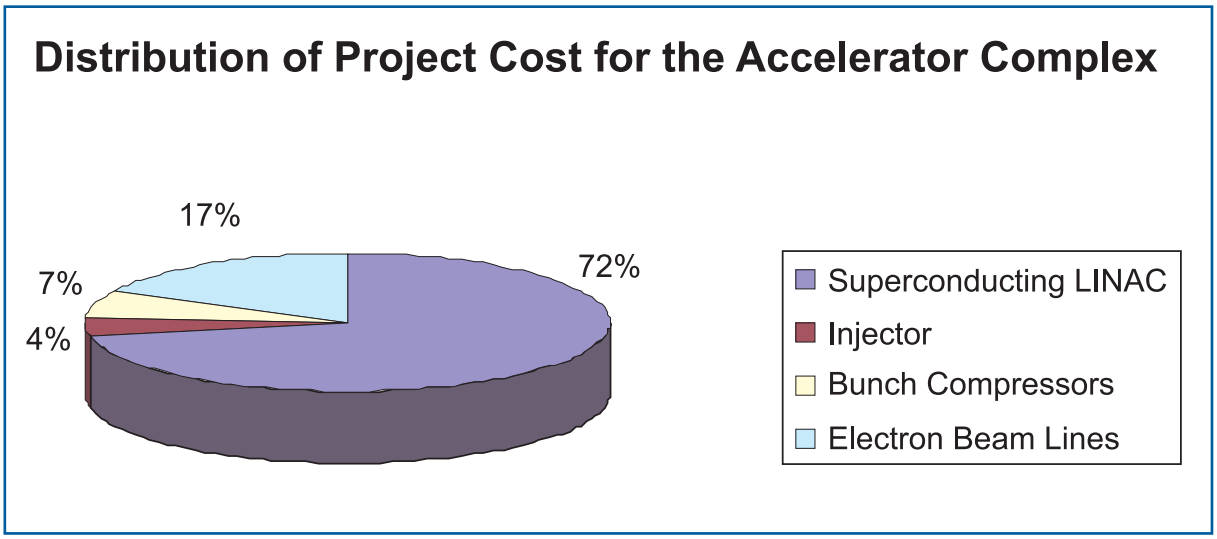

Figure 4.9.1 *Relative distribution of full project costs for the accelerator complex.*

The costs summarised in Table 4.9.1 and Figure 4.9.1 include the costs and manpower of the following components:

Injector: design and beam physics, electron RF gun and laser system, one accelerator module including the necessary high-power RF (modulator/klystron) and low level RF control components, beam diagnostic elements, beamline magnets and vacuum chambers, laser heater, installation and technical commissioning.

Bunch compressors: design and beam physics, beam diagnostic elements, all beamline components, i.e. magnets and vacuum chambers, installation and technical commissioning.

Electron beamlines: design and beam physics, collimation system, diagnostic systems, vacuum system and focusing/steering magnets from the end of the linac to the beam dumps (including undulator sections), kicker system for the beam distribution, trajectory stabilisation feedback and beam dumps.

Superconducting linac: is the largest item of the accelerator complex contributing close to 72% to its total costs; the cost structure of the superconducting linac is given in the following section.

4.9.1 Cost and manpower requirements of the superconducting linac

Table 4.9.2 and Figure 4.9.2 show the individual costs for the major components of the superconducting linac as described in Section 4.2. The individual costs are given in terms of capital investment, personnel costs and the full costs. Integrated over the entire construction phase, 636.8 FTE are required for the superconducting linac.

	Capital investment [M€]	Personnel cost [M€]	Full cost [M€]
Modules	24.31	7.11	31.42
Cavities	97.54	11.05	108.59
RF system	69.81	26.08	95.88
Vacuum system	6.44	3.91	10.36
Beam diagnostic	1.59	0.48	2.07
Total	**199.69**	**48.64**	**248.32**

Table 4.9.2 *Project cost distribution for major items of the superconducting linac. Values are given for capital investment, personnel costs and full costs in Million-Euro.*

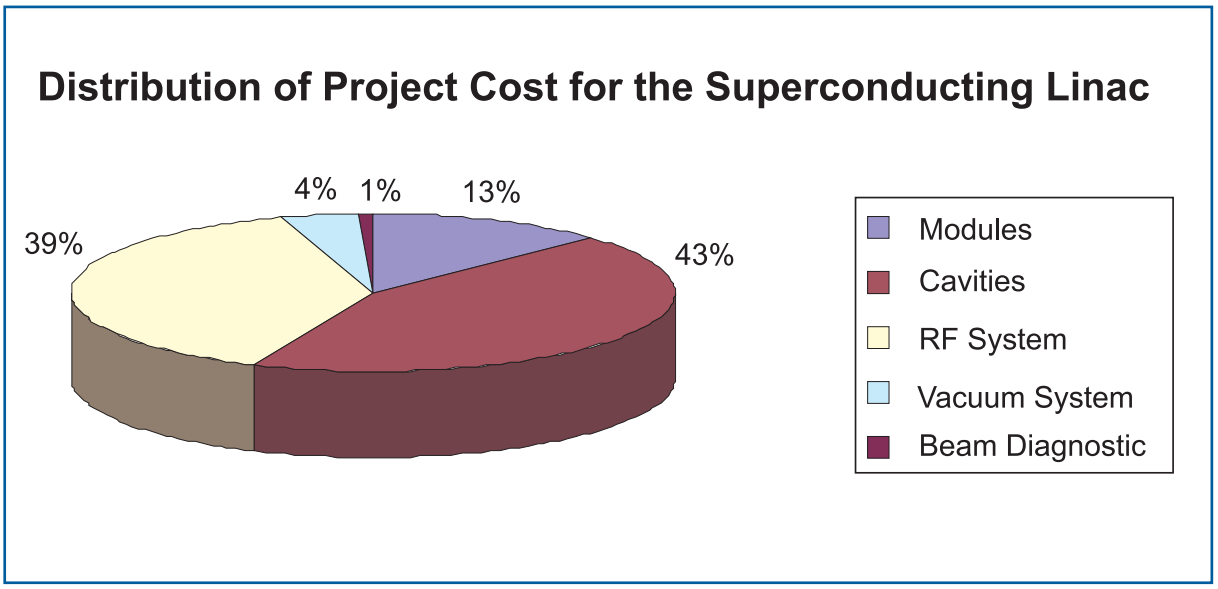

Figure 4.9.2 *Relative distribution of full project costs for the superconducting linac.*

The costs summarised in Table 4.9.2 and Figure 4.9.2 include the costs and manpower of the following components.

Modules: complete accelerator module cryostat and vacuum vessel, quadrupole magnets, assembly of the module, setup and supervision of fabrication, installation and technical commissioning.

Cavities: Niobium material, cavity fabrication and preparation, He tank welding and string assembly, input coupler, higher-order mode coupler, frequency tuner, setup and supervision of fabrication.

RF system: RF modulators, power supplies, transformers, klystrons, high voltage pulse cables, waveguide system, low level RF control, setup of fabrication and supervision, component test, installation and technical commissioning.

Vacuum system: inter-cavity connections, cold valves, flanges, insulation and RF coupler vacuum systems, vacuum pumps, installation and technical commissioning.

Beam diagnostic: beam position monitors.

References

[4-1] R. Brinkmann et al. (eds.), *TESLA Technical Design Report – Part II: The Accelerator*, DESY 2001-011, pp. II-19, March 2001; http://tesla.desy.de

[4-2] P. Kneisel, G. Ciovati, G.R. Myneni, W. Singer, X. Singer, D. Proch, T.Carneiro, *Influence of Ta content in high purity niobium on cavity performance*, Proc. Particle Accelerator Conference, USA, Mai 16-20, 2005.

[4-3] W. Singer, A. Brinkmann, D. Proch, X. Singer, *Quality requirements and control of high purity niobium for superconducting RF cavities*, Physica C 386 (2003) 379-384.

[4-4] G.R. Myneni, *Physical and mechanical properties of single and large crystal high-RRR niobium*, Proc. 12th Workshop on RF Superconductivity, SRF- 2005, 10-15 July 2005, Ithaca, USA.

[4-5] P. Kneisel, G. Ciovati, G.R. Myneni, J. Sekutowicz, T. Carneiro, *Performance of large grain and single crystal niobium cavities*, Proc. 12th Workshop on RF Superconductivity, SRF- 2005, 10-15 July 2005, Ithaca, USA.

[4-6] R. Brinkmann et al. (eds.), *TESLA Technical Design Report – Part II: The Accelerator*, DESY 2001-011, pp. II-27, March 2001.

[4-7] B. Aune et al., *Superconducting TESLA Cavities,* Phys. Rev. ST Accel. Beams 3 (2000) 092001.

[4-8] L. Lilje, E. Kako, D. Kostin, A. Matheisen, W.-D. Moeller, D. Proch, D. Reschke, K. Saito, P. Schmueser, S. Simrock, K. Suzuki, *Achievement of 35 MV/m in the Superconducting Nine-Cell Cavities for TESLA*, Nucl.Instr.Meth. A524 (2004) p.1-12.

[4-9] K. Saito et al., *High gradient performance by electropolishing with 1300 MHz single and multi-cell niobium superconducting cavities*, Proc. 9th Workshop on RF Superconductivity, SRF-1999, Santa Fe, USA, (1999) 288-291.

[4-10] J.P. Desvard et al., *Cryogenic and electrical test cryostat for instrumented superconductive RF cavitites (CHECHIA)*, Advances in cryogenic engineering, 41 (1995) 905.

[4-11] J. Graber, *High Power Processing Studies of 3 GHz Niobium Superconducting Accelerating Cavities*, Dissertation at the Cornelle University, Ithaca, May 1993.

[4-12] W.-D. Moeller for the TESLA Collaboration, *High Power Coupler For The TESLA Test Facility*, Proc. 9th Workshop on RF Superconductivity, SRF-1999, Santa Fe, Vol.2, pp.577-581.

[4-13] B. Dwersteg, D. Kostin, M. Lalayan, C. Martens, W.-D. Moeller, *Tesla RF Power Couplers Development at DESY*, Proc. 10th Workshop on RF Superconductivity, SRF-2001, September 6-11, 2001, Tsukuba, Japan, in KEK Proceedings 2003-2, pp.443-447.

[4-14] M. Ukkola and P. Yla-Oijala, *Numerical Simulation of Electron Multipacting in TTF III Cold Window with a DC Bias*, Helsinki Institute of Physics, Finland, Technical Report, 2000.

[4-15] J. Lorkiewicz, B. Dwersteg, A. Brinkmann, W.-D. Moeller, D. Kostin, M. Lalayan, *Surface TiN Coating of TESLA Couplers at DESY as an Antimultipactor Remedy*, Proc. 10th Workshop on RF Superconductivity , SRF-2001, September 6-11, 2001, Tsukuba, Japan, in KEK Proceedings 2003-2, pp.448-452.

[4-16] S. Michizono, A. Kinbara et al., *TiN Film Coatings on Alumina Radio Frequency Windows*, J. Vac. Sci. Technol. A 10 (4) 1992.

[4-17] M. Dohlus, *3D CSR calculations for XFEL Bunch Compression*, TESLA Collaboration Meeting, DESY-Zeuthen, January 2004; http://www-zeuthen.desy.de/tesla2004/

[4-18] J. Sekutowicz, *Higher Order Mode Coupler for TESLA*, Proc. 6th Workshop on RF Superconductivity, October 4-8, SRF-1993, Newport News, Virginia, USA.

[4-19] J. Sekutowicz et al., *Proposed Continuous Wave Energy Recovery Operation of an X-Ray Free Electron Laser*, Phys. Rev. ST-AB, vol. 8, January 2005.

[4-20] P. Bosland, et al., *Third Harmonic Superconducting Passive Cavities In ELETTRA and SLS,* Proc.11th Workshop on RF Superconductivity , SRF-2003, Lübeck, Germany.

[4-21] P. Bosland, Bo Wu, *Mechanical study of the «Saclay piezo tuner» PTS (Piezo Tuning System)*, DAPNIA - CEA Saclay, CARE-Note-2005-004-SRF.

[4-22] M. Liepe, W.D. Moeller, S.N. Simrock, *Dynamic Lorentz Force Compensation with a Fast Piezoelectric Tuner*, DESY TESLA-01-03, 2001.

[4-23] P. Sekalski, private communication.

[4-24] CIEMAT, Research Center for Energy, Environment and Technology, Madrid, Spain.

[4-25] M. Juillard, C. Magne, A. Mosnier, B. Phung, *High Resolution BPM for the Next Linear Collider,* Beam Instr.Workshop 2000, Camebridge, Massachusetts, U.S., (2000), p. 259.

[4-26] A. Ballerino, *Conduction-cooled 60 a resistive current leads for the LHC dipole correctors*, LHC Project Report 691, March 2001.

[4-27] K. Zapfe, *Running experience with the vacuum system of the superconducting linac of the TESLA Test Facility*, Vacuum 73 (2004) 213.

[4-28] K. Zapfe, *The vacuum system for the superconducting linac of the TESLA Test Facility*, Vacuum 60 (2001) 51.

[4-29] K. Zapfe, F. Herrmann, D. Hubert, P. Schmüser, *A New Flange Design for the Superconducting Cavities for TESLA*, Proc. of the 8th Workshop on RF Superconductivity, Abano Terme, 1997, eds. V. Palmieri and A. Lombardi (INFN, LNL-INFN (Rep) 133/98) 457.

[4-30] D. Trines et. al., *The Insulating Vacuum System of the HERA Proton Ring;* Proc. of the XVth Int. Conference on High Energy Accelerators, Hamburg, 1992, ed. J. Roßbach, Int. J. Mod. Phys. A (Proc. Suppl.) 2B (1993) 347.

[4-31] C. Bearzatto, M. Bres, G. Faillon, *Advantages of Multiple Beam Klystrons*, ITG Garmisch-Partenkirchen, May 4 to 5, 1992.

[4-32] R. Palmer, *Introduction to Cluster Klystrons*, Proc. International Workshop on Pulsed RF Power Sources For Linear Colliders, RF93, Dubna, Protvino, Russia, July 5-9,1993, p. 28.

[4-33] A. Beunas, G. Faillon, *10 MW/1.5 ms, L-band multi-beam klystron*, Proc.Conf. Displays and Vacuum Electronics, Garmisch-Partenkirchen, Germany, April 29-30 1998.

[4-34] A. Beunas, G. Faillon, S. Choroba, A. Gamp, *A High Efficiency Long Pulse Multi Beam Klystron for the TESLA Linear Collider*, TESLA Report 2001-01.

[4-35] H. Bohlen, A. Balkcum, M. Cattelino, L. Cox, M. Cusick, S. Forrest, F. Friedlander, A. Staprans, E. Wright, L. Zitelli, K. Eppley, *Operation of a 1.3GHz, 10MW Multiple Beam Klystron*, Proc. XXII International Linear Accelerator Conference. Linac 2004, Lübeck, Germany, August 16-20, (2004) 693.

[4-36] A. Balkcum, E. Wright, H. Bohlen, M. Cattelino, L. Cox, M. Cusick, S. Forrest, F. Friedlander, A. Staprans, L. Zitelli, *Continued Operation of a 1.3GHz Multiple Beam Klystron for TESLA*, Proc. Sixth International Vacuum Electronis Conference, IVEC 2005, Noordwijk, The Netherlands, April 20-22, 2005, p. 505.

[4-37] A. Yano, S. Miyake, S. Kazakov, A. Larionov, V. Teriaev, Y.H. Chin, *The Toshiba E3736 Multi-Beam Klystron*, Proccedings of the XXII International Linear Accelerator Conference. Linac 2004, Lübeck, Germany, August 16-20, 2004, p. 706.

[4-38] Y.H. Chin, A. Yano, S. Miyake, S. Choroba, *Development of Toshiba L-Band Multi-Beam Klystron for European XFEL Project*, Proceedings of the 2005 Particle Accelerator Conference, PAC05, Knoxville, USA, May 16-20, 2005, p. 3153.

[4-39] W. Bothe, Pulse *Generation for TESLA, a Comparison of Various Methods,* TESLA Report 94-21, July 1994.

[4-40] H. Pfeffer, C.Jensen, S. Hays, L. Bartelson, *The TESLA Modulator*, TESLA Report 93-30.

[4-41] Ed. D.A. Edwards, *The TESLA TEST FACILITY LINAC-Design Report*, Tesla Report 95-01.

[4-42] H. Pfeffer, L. Bartelson, K. Bourkland, C. Jensen, Q. Kerns, P. Prieto, G. Saewert. D. Wolff, *A Long Pulse Modulator for Reduced Size and Cost*, Fourth Europ. Particle Accelerator Conf., London 1994.

[4-43] H. Pfeffer, L. Bartelson, K. Bourkland, C. Jensen, P. Prieto, G. Saewert, D. Wolff, *A Second Long Pulse Modulator For TESLA Using IGBTs*, Proc. Fifth European Particle Accelerator Conference, EPAC96, Sitges (Barcelona), 10-14 June 1996, p. 2585.

[4-44] W. Kaesler, *A Long-Pulse Modulator for the TESLA Test Facility (TTF)*, Proc. XXII International Linear Accelerator Conf., Linac 2004, Lübeck, Germany, August 16-20, (2004) 459.

[4-45] H.-J. Eckoldt, N. Heidbrook, *Constant Power TESLA Supplies for the Modulator*, TESLA Report 2000-36.

[4-46] H.-J. Eckoldt, *Pulse Cables for TESLA*, TESLA Report 2000-35.

[4-47] T. Grevsmühl, S. Choroba, P. Duval, O. Hensler, J. Kahl, F.-R. Kaiser, A. Kretzschmann, H. Leich, K. Rehlich, U. Schwendicke, S. Simrock, S. Weisse, R. Wenndorff, *The RF-Station Interlock for the European X-Ray Laser*, Proc. XXII International Linear Accelerator Conference, Linac 2004, Lübeck, Germany, August 16-20, (2004) 718.

[4-48] H. Leich, S. Choroba, P. Duval, T. Grevsmühl, V. Petrosyan, S. Weisse, R. Wenndorff, *An Advanced Interlock Solution for TTF2/XFEL RF Stations*, Proc. 14th IEEE_NPSS Real Time Conference, Stockholm, Sweden, June 4-10, (2005) 36.

[4-49] H. Leich, S. Choroba, P. Duval, T. Grevsmühl, A. Kretzschmann, U. Schwendicke, R. Wenndorff, *The Design of a Technical Interlock for TTF2/XFEL RF Stations*, NEC 2005, XX International Symposium on Nuclear Electronics & Computing (to be published).

[4-50] V. Katalev, S. Choroba, *RF Power Distributing Waveguide System for TESLA*, Proceedings of the Russian Particle Accelerator Conference, Rupac 2002, Obninsk, Russia, October 1-4, (2002,) 79.

[4-51] V. Katalev, S. Choroba, *Tuning of External Q and Phase for the Cavities of a Superconducting Linear Accelerator*, Proc. XXII International Linear Accelerator Conf., Linac 2004, Lübeck, Germany, August 16-20, (2004) 724.

[4-52] P. Sekalski, M. Grecki, C. Albrecht, *Performance of Magnetostrictive Elements at LHe Environment*, MIXDES 2005.

[4-53] K.T. Pozniak, R.S. Romaniuk, T. Czarski, W. Giergusiewicz, W. Jalmuzna, K. Olowski, K. Perkuszewski, S. Simrock, *FPGA and optical network based LLRF distributed control system for TESLA-XFEL Linear Accelerator,* Proceedings of SPIE - The International Society for Optical Engineering 5775, pp. 69-77.

[4-54] M. Grecki, T. Jezynski, A. Brandt, *Estimation of IQ Vector Components of RF Field - Theory and Implementation*, MIXDES 2005.

[4-55] T.A. Filipek, *Frequency Conversion in Field Stabilization System for Application in SC Cavity of Linear Accelerator*, SPIE - COO Warsaw, Poland 2005.

[4-56] W. Giergusiewicz, W. JaBmulna, K. Pozniak, N. Ignashin, M. Grecki, D. Makowski, T. JelyDki, K. Perkuszewski, K. Czuba, S. Simrock, and R. Romaniuk, *Low latency control board for LLR system – Simcon 3.1*, Photonics Applications in Industry and Research IV, August 2005.

[4-57] T. Czarski, K.T. Pozniak, R.S. Romaniuk, S. Simrock, *Cavity parameters identification for TESLA control system development , N*ucl. Instr. and Methods in Physics Research, Section A: Accelerators, Spectrometers, Detectors and Associated Equipment 548 (2003) 283-297.

[4-58] T. Jezynski, M. Grecki, *A Performance Diagnostic Tool for the Low Level RF Control System for VUV-FEL*, MIXDES 2005.

[4-59] P. Pucyk, T. JezyDski, W. Koprek, T. Czarski, K.T. Pozniak, R.S. Romaniuk, *DOOCS server and client application for FPGA based TESLA cavity controller and simulator,* Proceedings of SPIE - The International Society for Optical Engineering 5775 pp. 52-60.

[4-60] D. Makowski, M. Grecki, A. Napieralski, S. Simrock, and B. Mukherjee, *A distributed system for radiation monitoring at linear accelerators*, IEEE Transactions on Nuclear Science (TNS), p. in print, January 2006.

[4-61] B. Mukherjee, D. Makowski, and S. Simrock, *Dosimetry of high energy electron linac* produced photoneutrons and the bremsstrahlung gamma rays using TLD-500 and TLD-*700 dosimeter pairs*, Nucl.Instr. and Meth. A 545 (2005) 830-841.

[4-62] P. Pawlik, M. Grecki, S. Simrock, *System for High Resolution Detection of Beam Induced Transients in RF Signals*, MIXDES 2005.

[4-63] P. Pawlik, M. Grecki, S. Simrock, *Single Bunch Transient Detection for the Beam Phase Measurement in Superconducting Accelerators*, DIPAC 2005, Lyon, France, 6th-8th June 2005.5.Undulators SASE and for Spontaneous Emission.

[4-64] S. Schreiber et al., *The Injector of the VUV-FEL at DESY*, Proceedings of FEL 2005, to be published.

[4-65] P. Piot et al., C*onceptual design for the XFEL Photoinjector*, DESY TESLA-FEL 01-03, 2001.

[4-66] TESLA - Technical Design Report, Part II, TESLA-FEL 01-05, 2001.

[4-67] V. Miltchev et al., *Measurements of thermal emittance for cesium telluride photocathodes at PITZ*, Proceedings of FEL 2005, to be published.

[4-68] H.-J. Han et al., *Emission Mechanisms in a Photocathode RF Gun*, Proceedings of PAC 2005.

[4-69] K. Honkavaara et al., *Electron Beam Characterization at PITZ and the VUV-FEL at DESY*, Proceedings of FEL 2005, to be published.

[4-70] K. Honkavaara et al., *Transverse Electron Beam Diagnostics at the VUV-FEL at DESY*, Proceedings of FEL 2005, to be published.

[4-71] V. Miltchev, Modelling the Transverse Phase-space and Core Emittance Studies at PITZ, Proceedings of FEL 2005, to be published.

[4-72] Will, P. Nickles, W. Sandner, *A Laser System for the TESLA Photo-Injector*, internal design study, Max-Born-Institut, Berlin 1994.

[4-73] I. Will, G. Koss, I. Templin, *The upgraded photoinjector laser of the TESLA Test Facility*, Nucl. Instr. and Meth. A 541 (2005) 467-477.

[4-74] K. Abrahamyan et al., *Experimental characterization and numerical simulations of the electron source at PITZ,* Nucl. Instr. and Meth. A, in press.

[4-75] B. Steffen et al., *Spectral Decoding Electro-Optic Measurements for Longitudinal Bunch Diagnostics at the DESY VUV-FEL*, Proceedings of FEL 2005, to be published.

[4-76] V. Balandin et al., *Optimized Bunch Compression System for the European XFEL*. PAC 2005.

[4-77] M. Dohlus, T. Limberg, *Impact of Optics on CSR-related Emittance Growth in Bunch Compressor Chicanes*. PAC 2005.

[4-78] M. Dohlus, K. Floettmann, Y. Kim, T. Limberg, *Injector and Bunch Compressor for the European XFEL*, EPAC 2004, P. 342-344.

[4-79] M. Dohlus, T. Limberg, *XFEL Bunch Compression System Set Up*. Commissioning Workshop, Zeuthen 2005. http://commissioning2005.desy.de/

[4-80] P. Piot et al., *Conceptual Design for the XFEL Photoinjector*, DESY TESLA-FEL 01-03, 2001.

[4-81] M. Dohlus and T. Limberg, *Bunch Compression Stability Dependence on RF Parameters*, FEL'05, Stanford, CA, 2005.

[4-82] V. Balandin and N. Golubeva, *The TrackFMN Program. User's Reference Manual*, unpublished.

[4-83] ASTRA; http://www.DESY.de/~mpyflo/Astra_dokumentation/

[4-84] M. Dohlus, T. Limberg, *CSRtrack: Faster Calculation of 3D CSR effects*, FEL 2004, 2004.

[4-85] E. Saldin, E. Schneidmiller and M. Yurkov, *Nucl. Instrum. Meth*. A 528 (2004) 355.

[4-86] http://www.desy.de/xfel-beam/data/component_list.xls

[4-87] M. Dohlus, private communication.

[4-88] M. Martin and I. Zagorodnov, *Impact of Undulator Wake Fields and Tapering on the European X-Ray FEL Performance*, DESY TESLA-FEL 2005-10.

[4-89] K.L.F. Bane and G.V. Stupakov, SLAC-PUB-10707, (2004).

[4-90] I.A. Zagorodnov, T. Weiland, *TE/TM field solven for particle beam simulations without numerial Cherenkov radiation,* Physical Review – STAB 8, (2005) 042001.

[4-91] M. Dohlus, TESLA 2001-26, (2001).

[4-92] S. Reiche, *Genesis 1.3; a fully 3D time-dependent FEL simulation code*, Nucl. Instrum. Methods Phys. Res., Sect. A 429, (1999) 243.

[4-93] N. Baboi, *Multi-Bunch Beam Dynamics Studies for the European XFEL*, Proceedings of LINAC 2004, Lübeck.

[4-94] N. Baboi, R. Brinkmann, *Higher order mode effects and multi-bunch orbit stability in the TESLA main linac*, DESY-TESLA-2000-28, 2000, Hamburg.

[4-95] H. Delsim-Hashemi, *Broadband single shot spectrometer*, Proceedings of the 2005 FEL conference, San Francisco, California.

[4-96] M. Juillard, C. Magne, A. Mosnier, B. Phung, high *resolution BPM for the next linear colliders*, 9th Beam Instrumentation Workshop (BIW 2000), Cambridge, Massachusetts, 2000.

[4-97] M. Hüning et al., *Observation of femtosecond bunch length using a transverse deflecting structure*, Proceedings of the 2005 FEL conference, San Francisco, California.

[4-98] Ch. Gerth, M.Röhrs, H. Schlarb, *Layout of the diagnostic section for the European XFEL*, Proceedings of PAC 2005, Knoxville, Tennessee.

[4-99] M. Röhrs et al., *Measurement of Slice-Emittance using a transverse deflecting structure*, Proceedings of the 2005 FEL conference, San Francisco, California.

[4-100] B. Steffen et al., *Spectral decoding electro-optic measurements for longitudinal bunch diagnostics at the DESY VEV-FEL,* Proceeding of the 2005 FEL conference, San Francisco, California; A.Cavalieri et al., Phys. Ref. Lett. 94, 114801.

[4-101] S. Casalbouni et al., *Numerical Studies on the Electro-Optic Sampling of Revalistic Electron Bunches*, TESLA Report 2005-01.

[4-102] T. Raubenheimer, F. Zimmermann, *Fast beam-ion instability I. linear theory and simulation*, Phys.Rev.E 52 (1995) 5487-5497.

[4-103] E. Bondarchuk et al., *Technical proposal for a batch of electromagnets for the X-FEL Project*, St. Petersburg, September 2005.

[4-104] M. Maslov, V. Sytchev, M. Schmitz, *Layout Considerations on the 25GeV/300kW Beam Dump of the XFEL Project, DESY*, (2006) TESLA-FEL Report 2006-05.

[4-105] N. Tesch, A. Leuschner, *Sicherheitsbericht zum Strahlenschutz für das Planfest-stellungsverfahren des europäischen Röntgenlasers XFEL*, DESY, 13.4.2005.

[4-106] M. Hentschel et al., *Attosecond metrology*, Nature 414, 509-513 (2001).

[4-107] E. Goulielmakis et al., *Direct Measurement of Light Waves*, Science, Vol. 305, 1267-1269 (2004).

[4-108] A. Cavalieri et al., *Clocking Femtosecond X-ray*, Phys. Ref. Lett. 94, 114801.

[4-109] A. Cavalieri, *Electro-optic characterization of femtosecond electron bunches*, PhD-thesis, published by the University of Michigan.

[4-110] A. M. Lindberg et al., *Atomic-scale visualization of inertial dynamics*, Science, Vol. 308, 392-395 (2005).

[4-111] M. Drescher, DESY Proposal II-02-042 FEL.

[4-112] B. Steffen et al., *Spectral decoding electro-optic measurements for longitudinal bunch diagnostics at the DESY VUV-FEL*, Proceedings of the 27th International Free Electron Laser Conference, San Francisco, 2005.

[4-113] E.L. Saldin et al., *Terewatt-Scale Sub-10-fs Laser Technology – Key to Generation of GW-Level Attosecond Pulses in X-Ray Free Electron Laser*, DESY Report 04-13, January 2004.

[4-114] T. Zwart et al., *The MIT Bates X-ray laser project*, Proceedings of the 2003 Particle Accelerator Conference, Portland (2003).

[4-115] J. Kim et al., *Large-scale timing distribution and RF-synchronization for FEL facilities*, Proceedings of the 26th International Free Electron Laser Conference, Trieste, 2004.

[4-116] Jun Ye et al., *Sub-10-femtosecond synchronization of two passively mode-locked Ti:sapphire oscillators*, Phy. Rev. A, Vol. 64, 021802(R).

[4-117] T.R. Schibli et al., *Attosecond active synchronization of passsive mode-locked lasers by balanced cross correlation*, Optics Letters, Vol. 28, No. 11 (2003) 947-949.

[4-118] M. Margalit, et al., *Noise in pulsed injection locking of a passively modelocked laser*, IEEE Journal of Quantum Electronics, Vol. 32, No. 5 (1996) 796-801.

[4-119] J. Kim et al., *A Balanced Optical-to-RF Phase Detector for Synchronization and Timing Distribution in XFELs*, Midterm Report for DESY-MIT Synchronisation Project, 40003350-1.

[4-120] F.X. Kärtner, *Few-Cycle Laser Source for the Electron Beam Modulation in XFELs on an Attosecond Timing scale and High Harmonic Seed Generation*, internal DESY report, 500040-1.

[4-121] S.A. Diddams et al., *An Optical Clock Based on a Single Trapped 199Hg+ Ion*, Science 293 (2001) 825.

[4-122] S. Namiki and H.A. Haus, *Noise of the stretched pulse fiber ring laser: Part I-Theory*, IEEE. J. Quantum Electron. 33 (1997) 649.

[4-123] J.B. Schlager et al., *Passively mode-locked glass waveguide laser with 14-fs timing jitter*, Opt. Lett. 28 (2003) 2411.

[4-124] J. Kim, F.O. Ilday, A. Winter and F.X. Kärtner, *Timing Distribution and RF-Synchronization of Mode-Locked Lasers*, in 2005 Digest of the LEOS Summer Topical Meetings, IEEE, New York, (2005), 149-150.

[4-125] L.E. Nelson et al., *Ultrashort-pulse fiber ring laser*, Applied Physics. B 65, (1997) 277-294.

[4-126] E.N. Ivanov, S.A. Diddams and L. Hollberg, *Analysis of Noise Mechanisms Limiting the Frequency Stability of Microwave Signals Generated With a Femtosecond Laser*, IEEE J. Sel. Top. Quant. Elec. 9 (2003) 1059-1065.

[4-127] Posseidon Scientific Instrument, Report on the 1.3 GHz DRO for DESY.

[4-128] J. Kim, F. Ludwig, D. Sheevers, F.Ö. Ilday, J. Burnham, F.X. Kärtner, *A balanced optical-RF phase detector*, Proceedings of the Conference on Lasers and Electro-Optics, Long Beach, 2006.

[4-129] A. Winter et al., *High-precision Optical Synchronization System for X-ray Free Electron Lasers*, Proceedings of the 27th International Free Electron Laser Conference, San Francisco, 2005.